1971

A photomechanics study of wave propagation

John Barclay Ligon
Iowa State University

A photomechanics study of wave propagation

by

John Barclay Ligon

A Dissertation Submitted to the
Graduate Faculty in Partial Fulfillment of
The Requirements for the Degree of
DOCTOR OF PHILOSOPHY

Major Subject: Engineering Mechanics

Approved:

Signature was redacted for privacy.

In Charge of Major Work

Signature was redacted for privacy.

For the Major Department

Signature was redacted for privacy.

For the Graduate College

Iowa State University
Ames, Iowa

1971

TABLE OF CONTENTS

INTRODUCTION

In recent years, interest in wave propagation has grown considerably with increasing emphasis on earthquake phenomena, petroleum exploration and nuclear detection. The electronic computer has also aided this growth since in the past even the simplest problems in wave mechanics required a lengthy, and usually impractical, pursuit in order to extract numerical results. At the present, straight forward theoretical problems in wave mechanics can be handled with modest effort when mathematically convenient approximations to the loading functions are assumed. However, when analyzing stress waves propagating in complex regions, theoretical solutions become extremely complicated and experimental information is often used to provide insight into the problem.

In order to compare a theoretical solution with experimental results, complete knowledge of the manner in which a transient stress wave forms and attenuates in a medium is a necessity. With the characteristic of the pulse known, the effects of dispersion, dissipation, and geometric attenuation can be examined and compared to that predicted by theory.

In the current study, dynamic photoelasticity was chosen as the experimental technique used to investigate the formation of a stress pulse that is transmitted from an explosive charge ignited in a circular cavity in an infinite plate. In order to accomplish this task, an ultra high speed photographic

system was constructed by the author to record the dynamic photoelastic event.

Motivation for studying the formation of the stress pulse resulting from detonation of an explosive charge in a circular cavity arose from apparent inconsistencies in the method frequently used for determining the pulse shape. The method relies on extrapolated data from far field studies to approximate the shape and magnitude of the loading function. This data indicates that the stress pulse that is formed in the far field of the medium is simply the geometrically attenuated wave originally applied to the boundary. Far field studies indicate that the radial component of the compressional stress wave exhibits a tensile tail as it propagates through the medium. The inconsistencies arise when the magnitude of the radial tensile tail established by the far field trend are extrapolated to the loading boundary where the stress would be expected to be a maximum. However, when the explosive has ceased to burn, the compressive stress acting on the hole boundary diminishes to zero and the cavity boundary remains free of stress in the radial direction. Therefore, the hole boundary cannot support a tensile radial stress. This indicated that the stress wave must not be formed completely until it has traveled a short distance into the medium. This was indeed the case as will be shown in subsequent chapters.

INTRODUCTORY PHOTOMECHANICS

Photomechanic methods of experimental stress analysis are based on the property of temporary double refraction exhibited by certain transparent materials when they are stressed or strained.

Historical Background

The photoelastic phenomenon was first presented in 1816 to the Royal Society of London by Sir David Brewster (1). Brewster reported that glass, which otherwise, had no influence on a beam of polarized light, when subjected to tension or compression, exhibited properties of double refraction similar to natural crystals such as quartz. He later suggested that the stresses in structures could be analyzed by use of these stressed transparent models. In 1823, Brewster described the apparatus that he used to load his models. This apparatus consisted of a source of polarized light, a frame for placing a measurable load on the specimen, a lens, and a screen thus establishing the forerunner of the present day polariscope.

Although significant contributions were made through the years by physicists such as Nicol, inventor of the polarizing prism, and Neumann (2), James Clerk Maxwell (1831-1879) (3) probably did more in the period to put the science on a firm basis as well as to develop equipment

which gave satisfactory results. However, it was not until 1931 when Coker, an engineer, and Filon, a mathematician, collaborated on their historic Treatise on Photoelasticity (4) that interest was revived in photomechanics and the move towards engineering applications was initiated.

In 1941, Max M. Frocht greatly extended the work of Coker and Filon in his book Photoelasticity, Volume I (5) and later in 1948 with Photoelasticity, Volume II (6). Since that time, photoelasticity has become a useful experimental tool, applicable to numerous engineering problems. The introduction of texts by Dally and Riley (7), Durelli and Riley (8), Jessop and Harris (9) and Heywood (10), indicate the extent of interest in the method.

Basic Theory

As stated earlier, the basic concept upon which photomechanics methods in general and photoelasticity in particular is based is the optical property of double refraction. Certain materials such as quartz are permanently double refracting. To distinguish these from the materials that are used in photoelasticity, which exhibit the phenomenon only when subjected to stress or strain, the term temporary double refraction or birefringence was adopted.

When observed in a field of polarized monochromatic light, the photomechanics effect of temporary double refraction manifests itself in the form of alternate dark

and light bands which are referred to as interference or isochromatic fringes. At a given point in a material, the fringes will be ordered according to the number of dark and light cycles that appear as the load is increased from zero to its final value.

This isochromatic information is expressed in terms of the stress-optic law for photomechanical analysis. This law states that the fringe order at a given point in a transparent material subjected to stress is proportional to the thickness of the material in the direction of light propagation and to the difference between the principal stresses acting on the plane perpendicular to the direction of light propagation. If one of the principal directions in the model is not parallel to the light propagation axis, the isochromatic information that is obtained is in terms of secondary principal stresses. These are the maximum and minimum of those normal stresses in the plane of the model which is perpendicular to the axis of light propagation. When stresses vary across the thickness of the model, the optical effect is related to their average values. The stress-optic law in its simplest form is expressed by the relation:

$$N = \frac{h}{f_\sigma} (\sigma_1 - \sigma_2) \qquad (1)$$

where:

N = fringe order

h = thickness of model

σ_1, σ_2 = in-plane principal or secondary stresses

f_σ = material stress fringe coefficient

The material fringe coefficient is also given by:

$$f_\sigma = \frac{\lambda}{C}$$

where:

λ = wave length of light source

C = stress optic coefficient (a property of the material)

The optical effect of birefringent materials may be dependent on stress or strain, or both. When the material is linearly elastic, the stress and strain are linearly related and the coefficient, C, may refer to either stress or strain. Since C is constant for a particular material, f_σ is directly related to the monochromatic light source used for analysis. Therefore, a specimen may be calibrated under a light source of one wave length and used to analyze stress under a different source provided a correction is made for the wave length. This type of procedure was used in the current study. The materials were calibrated in a sodium diffused light polariscope and later used for analysis in a dynamic polariscope with a spark light source.

Dynamic Photoelasticity

In order to interpret the information that is available from dynamic photoelasticity, the well established validity of Equation 1 for static analysis had to be extended for use at high loading rates. Frocht (11) was the first to verify the stress optic law for uniaxial dynamic stress fields. Later, Thau and Dally (12) extended the validity of the law to encompass a biaxial state of dynamic stress. These investigators established that the dynamic stress-optic law was the same as that used for static analysis provided the material fringe coefficient was calibrated at the loading rates associated with the dynamic isochromatics, i.e.

$$\frac{N_d (f_\sigma)_d}{h} = (\sigma_1 - \sigma_2)_d \qquad (2)$$

where:

$(f_\sigma)_d$ = dynamic stress optic coefficient

Photomechanical Analysis

A two-dimensional analysis is justified when the state of stress in a structure can be approximated by a generalized plane stress condition. Once a model is machined to the given geometry, it is placed in a circular polarized mono-

chromatic light field and subjected to the desired state of loading ($\bar{P}_1$, $\bar{P}_2$,..., $\bar{P}_n$) (Figure 1). The fringe patterns that are viewed can be permanently recorded on photographic film for analysis at the convenience of the investigator. Since the fringes can be thought of as representing the loci of points of constant maximum in-plane shear, the maximum shear distribution throughout the model can be obtained by the process of counting the fringes and multiplying their order by the appropriate calibration constant.

The major difficulty in photoelastic analysis is encountered in separating the principal stresses. On free boundaries and at any other points where the stress field is uniaxial, the nonzero principal stress is directly determined from the stress optic equation. When evaluating stresses at interior points of the model, additional information is usually required for determining the principal stresses. Various methods such as Moire and electrical analogy techniques have been developed to provide this added information. However, in certain select cases, symmetry of loading will allow for the separation of the principal stresses without introducing additional experimental data. Such a technique was utilized in the current study.

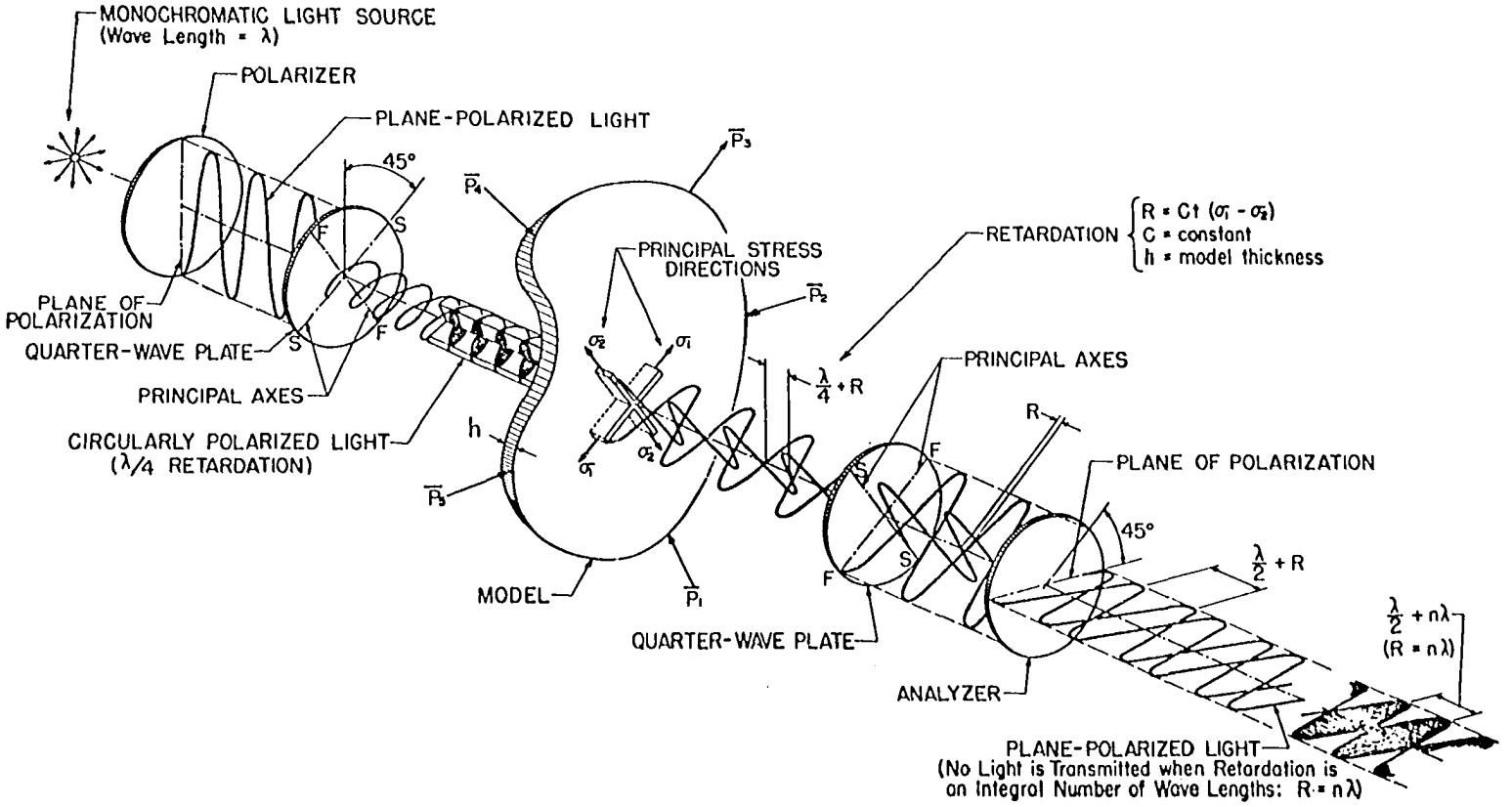

Figure 1. Schematic diagram of optical transformations in a circular polariscope, reference 8, page 37

LITERATURE SURVEY

In order to investigate the propagation of stress waves in solids by photomechanic technology, three disciplines of theoretical and experimental mechanics are of interest. These are: (a) dynamic photoelasticity, since the stress wave patterns that are exhibited in the birefringent materials are transient (b) high speed photography, since the stress patterns that must be photographically frozen during a sequence are sometimes moving in excess of 100,000 in./sec. (c) theoretical and experimental wave mechanics, since the primary objective of this and future work is the study of stress waves propagating in various materials.

Dynamic Photoelasticity

In 1901, Konig (13), who is regarded as the first experimentalist to develop techniques in dynamic photoelasticity, used a simple streak camera and the photoelastic technique to study shear stresses in vibrating glass beams. Twenty-seven years later, Tuzi (14) in Japan recorded the loading and unloading of several specimens by kinematography at the rate of 32 frames per second. Frocht (15) recorded similar patterns in this country, in 1932, with a camera operating at a speed twice that of Dr. Tuzi.

In 1936, Tuzi and Nisida (16) introduced streak photography into dynamic photoelasticity by recording disks and

beams subjected to impacts with a carbon arc lamp and a rotating drum camera.

In 1946, by utilizing an arditron discharge tube, Senior and Wells (17) were able to achieve single light flashes of microsecond duration which permitted study of several problems of impact on rods and plates made of zylonite. Three years later, Foeppl (18) used framing rate of 3000 frames per second to study uniaxial bending stresses in beams subjected to transverse impact.

In 1955, Christie (19-20) modified the spark camera, originally designed by Cranz and Schardin (21) in 1929, to study the stress field surrounding a propagating crack and the reflection of elastic waves from free boundaries. A year later, Schardin (22) applied the spark camera to the study of failure processes. Realizing the advantages of using low modulus birefringent rubber for a dynamic photoelastic model material, Perkins (23) was able to successfully record fringe photographs of stress waves with the Fastax camera. The application of the image dissection camera to stress wave propagation was introduced by its designer, Courtney-Pratt, in 1953 (24) on tests using glass molds. Schwieger (25) was one of the first investigators to utilize the photoelectric cell and oscillograph recorder for point intensity measurement in dynamic photoelastic studies when he published his work in 1956.

In the late 1950's, Frocht, Betser, and Flynn (26-28)

incorporated streak photography in their analysis of a compressed strut, a simply supported beam, and a diametrically compressed disk. In 1961, Flynn and Frocht (29) investigated Saint Venent's Principle under dynamic loading where they found that in regions of uniform stress distribution, the maximum stresses were essentially the same whether a central circular cavity was present or not.

In 1957, Wells and Post (30) examined the velocity and stress field associated with a running crack as initiated previously by Christie (31) and Schardin (22). They used thin models (1/8 inch thick) coupled with fringe multiplication where the event was recorded with a 2 by 2 array multiple spark camera. Their results indicated that the dynamic stress distributions in the vicinity of the crack approximated that of static distributions in models extended at their ends by a fixed displacement. They also found that measurements of the terminal crack velocity compared well with calculated values, but observed that rates of acceleration were smaller than calculated.

From 1957 until 1964, Durelli, Riley, Dally, and Daniel (32-39) utilized a low modulus material, urethane rubber (Hysol 8705), and a Fastax camera operating at 14,000 frames per second to obtain dynamic fringes moving with a wave velocity of approximately 200 ft./sec. Dally, Riley, and Durelli found that the stress-optic coefficient, strain-optic coefficient, and elastic modulus were all rate dependent

while Poisson's ratio was relatively insensitive to loading rate (35). In 1959, these three investigators supplemented the photoelastic method with an embedded grid (34) technique. Three years later, Riley and Durelli employed Moire techniques to aid in photoelastic data reduction (38). Using these auxiliary techniques with photoelasticity, stress concentration, stress distribution on the boundary of holes in plates, and the mechanical-optical response of materials under dynamic conditions were obtained.

Throughout the 1960's Flynn and his associates at the Frankford Arsenal conducted numerous studies in photoelastic wave propagation (40-50). Although Flynn conducted his Ph. D. research in 1954 on dynamic photoelasticity (51), the activity at Frankford did not start until 1956 when Feder, Gibbons, Gilbert, and Offenbacker applied a commercial ultra high-speed framing camera (Beckman and Whitley 189) to dynamic photoelastic problems (52). Flynn has since incorporated a dual-beam polariscope for simultaneously recording normal and oblique incidence rays which provide sufficient data to separate principal stresses on axes of symmetry. When recording photoelastic wave motion in the low modulus materials (Hysol 8705, urethane rubber), Flynn utilized the Fastax in conjunction with the dual-beam polariscope. However, with the high modulus materials (Homolite 100) he incorporated the Beckman-Whitley camera in the dual-beam polariscope in order to

photographically "freeze" the rapid moving stress waves.

In the early 1960's, Dally and Riley developed a modified version of the multiple spark system used by Christie for their work in dynamic photoelasticity (53). Their system utilized cascading electrical sparks to allow the dynamic fringe patterns to be photographed with an exposure time of 0.4 microseconds at rates up to 700,000 frames per second for sixteen consecutive frames. With this system, Dally, Riley, and their associates conducted numerous studies in half-planes subjected to transient internal and boundary concentrated loads in both uniform and layered models (54-61). Daniels (62) has recently prepared an extensive report on the study of wave propagation in layered media. He utilized various loading, experimental, and photographic recording techniques to obtain: a) the propagation and attenuation characteristics of incident, reflected, and refracted waves; b) stress determinations using photoelastic and Moire data; c) and effects of impedance mismatch between layers.

Since most birefringent polymers are viscoelastic to some degree, an increasing interest in photoviscoelastic wave propagation has become evident in recent years (63-70).

The use of a single Q-switched ruby laser as a source of light for dynamic photoelasticity (71-74) produced a degree of photographic fringe resolution never before achieved.

In 1967, Rowlands and his associates (74-76) coupled a sequentially modulated ruby laser, whose pulse duration is less than 65 nanoseconds, with a Bechman-Whitley model 189 high speed camera and thus added a new dimension to transmitted and scattered light dynamic photoelasticity.

Since the isochromatics that are recorded in photographs of stress waves propagating in birefringent material yield only information about points of principal stress difference, fundamental problems of separating the principal stresses have been considered by various investigators. Some of the techniques that have been investigated for principal stress separation under dynamic conditions are embedded grids (34), absolute retardation (30), Moire (38, 62), oblique incidence (46), and analytical procedures (77-78).

Although the literature review above provided a host of information that was utilized in the current study, published literature on dynamic photoelastic analysis of the specific problem of interest, the formation and description of an explosive pulse in the vicinity of loading, was not available. Dally and Riley published some work in this area (77, 53, 54) in the mid 1960's; however, they were unable to obtain information any closer than two inches from the loading boundary because of inherent synchronization delays, inadequate smoke shielding, and high fringe densities.

Additional information on previous work in dynamic

photoelasticity can be obtained from an excellent comprehensive review article on dynamic photoelasticity by W. Goldsmith (79).

High Speed Photography

The fundamental requirement for analysis in dynamic photoelasticity is the ability to record photographically the event since the eye is limited by time, distance, and storage ability. Since the correct interpretation of the fringe magnitudes is the basic concern of photoelasticians, a photograph of a fringe pattern must have sufficient sharpness that the isochromatics can be readily resolved. In dynamic photoelasticity, the isochromatics in the high modulus, birefringent materials are propagating at speeds up to 100,000 in./sec. Therefore, the exposure duration of the photographic system must be sufficiently short to stop the motion. Since the mechanical shutters approach their practical limits at exposures around 100 microseconds, other means of shuttering have to be employed. When a photographic sequence of an event is desired, the system must also be capable of placing successive images on different portions of a film. Cameras that record photographs in this manner fall into three classifications: a) multiple-framing b) streak and c) image-dissection.

The characteristics and suitability of several specific high speed systems which fall within the three classifications,

are discussed in some detail by Rowlands (75), namely:

1. Streak Photography (80-81)
2. Rotary Prism Cameras (33), (44)
3. Cranz-Schardin System (19-21), (30), (53-60), (62), (77), (82-83)
4. Kerr Cell Camera (84-87)
5. Ellis "Smear" Camera (88-90)
6. Rotating Mirror Framing Camera with Image Compensation (91)
7. Image Dissection Camera (92-95)
8. Converter Camera (96)
9. Electro-Optic Light Beam Deflectors (97-98)

Dally, Henzi, and Lewis (82) have recently published a general theory on the fidelity of the high speed framing camera, the spark-gap camera, and the Q spoiled laser system used for dynamic photoelasticity.

For additional informations, there are numerous texts and articles on the subject of ultra high-speed photography available, references 99 through 111, to mention a few.

Wave Propagation

Because of the rapid growth of interest in wave mechanics in the past decade, a large amount of theoretical and experimental work has been published in the field in recent times. Although a complete review of these works would be superfluous to the present study, a few texts and articles of a classical nature will be mentioned in addition

to the literature directly related to the current problem.

General wave mechanics

Several excellent reviews of significant contributions in elastic wave propagation have been published in recent years. Among these is an extensive survey by Miklowitz (112), published in 1960, in which he reviews and lists some 135 books and papers on published works on the subject to that date. In 1966, Miklowtiz (113) updated his review with a total of 221 references. While at Brown University, Kolsky (114) published a review of experimental investigations of stress wave propagation up to 1960 in which he listed 121 references.

Of all of Kolsky's work on wave propagation in general, the most well known is his excellent text Stress Waves in Solids (115).

Another text which can be considered as classic on elastic waves in layered media was written by Ewing and Jardetzky (116) in 1959. Three years later Cagniard, Flinn, and Dix published a text on the reflection and refraction of progressive seismic waves (117).

Davies (118-119) has written several good papers for general information on stress waves in solids in which he has a sum total of 135 books and papers referenced.

In 1965, Dally, Riley, and Brillhart published a report in which they tabulated current analytical solutions

pertaining to stress wave propagation in solids subjected to dynamic point source loadings (120). From 73 references, they tabulated several relatively simple analytical solutions which would serve as guides for calibration models in the development of an experimental approach to more complex wave propagation problems.

Cylindrical waves generated from a cylindrical cavity in an infinite medium

Although extensive experimental and theoretical work has been done in the area of a cylindrical wave propagating from a point or line load in an infinite medium, very little literature is available on an experimental approach to the transient response from a uniform radial pressure suddenly applied to the boundary of a finite cylindrical hole in an infinite elastic medium. As early as 1927, Sezawa (121) published a paper that was concerned with the problem of a circular cavity subject to uniform blast loading. Kromm (122), Goodier and Jahsman (123) and Miklowitz (124) have considered the plane stress solution for the transient response of an infinite elastic plate with a radial pressure loading in a circular hole. Miklowitz pointed out that his solutions have application in calculating the tensile circumferential stresses generated by the unloading mechanism of a stretched elastic plate in which a circular hole is suddenly punched. Forrestal (125) later developed a

simplified approximate formula for the circumferential tensile stresses at the boundary of the hole which were in close agreement with Miklowitz's exact solutions. Finally, Miklowitz and Scott treated the problem of an infinite free plate with a circular cylindrical cavity subjected to a step normal displacement.

In a study by Eringen (126) a formal solution was written for a general transient excitation of the cavity wall using a Laplace transform and classical separation on the circumferential coordinates. Of particular interest to the current study was his consideration of blast loading on the circular cavity.

Selberg (127) gave a solution using Laplace transforms with some numerical results involving a uniform step input pressure in a cylindrical cavity for the dynamic plane strain problem which is equivalent to the dynamic plane stress problem (128) with the appropriate adjustment to the elastic constants. It was an approach similar to the one utilized by Selberg that was eventually adapted to use in conjunction with the results of the current investigation for future studies.

Although numerous publications, which were not closely related to the current study, were omitted from this review, the reference sections of the papers and texts discussed in this chapter contain most of the significant literature that has been published on wave propagation, dynamic

photoelasticity, and high speed photoelastic photography with few, if any, exceptions.

PHOTOGRAPHIC SYSTEM

Before investigating any dynamic photoelastic wave phenomenon, a suitable photographic recording system must be selected. In order to utilize the high modulus materials for models where wave velocities of 100,000 in./sec. are possible, a high speed camera capable of 50,000 to 1,000,000 frames per second with a shutter speed of less than 1/1,000,000 second is a necessity. In addition to the capabilities of high framing rates and fast shutter speeds, several other parameters had to be considered in selecting a high speed photographic system for the current study, namely:

1. Number of frames
2. Light intensity requirements
3. Synchronization
4. Size of field
5. Size of model image
6. Resolution
7. Flexibility
8. Cost

After reviewing several types of high speed recording systems, summarized in Table 1, the multiple spark camera was selected as the most suitable system for accomplishing the primary objectives of the current study and future work at a reasonable cost.

Table 1. The characteristics of several high speed photographic systems utilized in dynamic photoelasticity

Photographic System	Speed frames/sec.	Light Source	Field Size	Film Size	Sychronization	Relative Cost*
Single spark		spark	full	limited by cost only	electronic	1
Electronic sensor or photocell	limited by cost only	continuous	point		mechanical switch	2
Rotary prism camera (Fastax, Magnifax)	14,000-8mm 7,000-16mm 5,000-35mm	flash bulb	full	8, 16 or 35 mm	mechanical switch	3
Streak	1.5×10^6 equivalent exposures	flash bulb	line	35 mm	mechanical switch	4
Multiple spark	700,000 exposure time 0.4 μsec.	spark	limited by field lens size	limited by cost only	electronic	5
Electronic (image conversion)	200×10^6	extremely high intensity	full	$3\frac{1}{2} \times 3\frac{1}{2}$ inches	electronic	6
Beckman-Whitley or Ellis	4.3×10^6	extremely high intensity (Zenon flashtube or ruby laser)	full	35 mm	built in or electronic	7

* Rated in increasing cost, i.e. 1 is the lowest and 7 is the highest.

The reasons for rejecting the other systems varied. In referring to the systems in Table 1 in the order of increasing estimated cost, the single spark would have met all of the desired requirements except that only one frame would have been available for each experiment. Therefore, to obtain a photographic sequence, it would have been necessary to repeat the experiment several times with different delay intervals. While such an approach has been found to be adequate for many applica' >ns (129), (130), (74), it is not applicable to cases where the model material is destroyed or altered during the loading. The electronic photocell does not meet the field requirements since it is limited to point to point analysis which is similar to information gained from a resistance strain gage. The rotary prism camera, although a long proven moderate speed camera for photoelastic use, is limited to investigating low modulus materials because of its relatively slow framing rate. The streak camera was eliminated because of its limited field. Electronic image conversions do not yield a sufficient number of frames per cost to adequately record the dynamic event. The Beckman-Whitley and Ellis cameras, at the initiation of this research were limited by their need for an extremely high intensity light source which could not be easily achieved in the laboratory. When a modulated ruby laser was incorporated with the Beckman-Whitley (75), its light limitations were eliminated.

Although the sequential modulated ruby system was not fully developed at the beginning of the current study, its exorbitant cost of over $50,000 would have excluded its adoption since the multiple spark camera (with sixteen frames) could be built for less than one-third of that cost.

The multiple spark systems, as proven by earlier investigators (20), (53), provides adequate illumination with a short exposure time for a respectable number of frames. High framing rates, excellent resolution and a large image size are easily obtained with the system. Furthermore, the diameter of the field of view is limited only by the size of the field lens. At the initiation of the current research program, commercially available units did not have, at a reasonable cost, the flexibility in operation and synchronization desired for the present, as well as, future work at this laboratory. Therefore, a multiple spark camera was constructed by the author with several modifications different from those previously built. Since detailed design information is not available on past systems, the camera, along with numerous modifications made by the author, are outlined extensively throughout the subsequent sections with detailed numerical data available in Appendices A through E.

The multiple spark camera (Figure 2) is composed of three distinct systems. These are designated as the spark gap system, the optical system, and the synchronization and

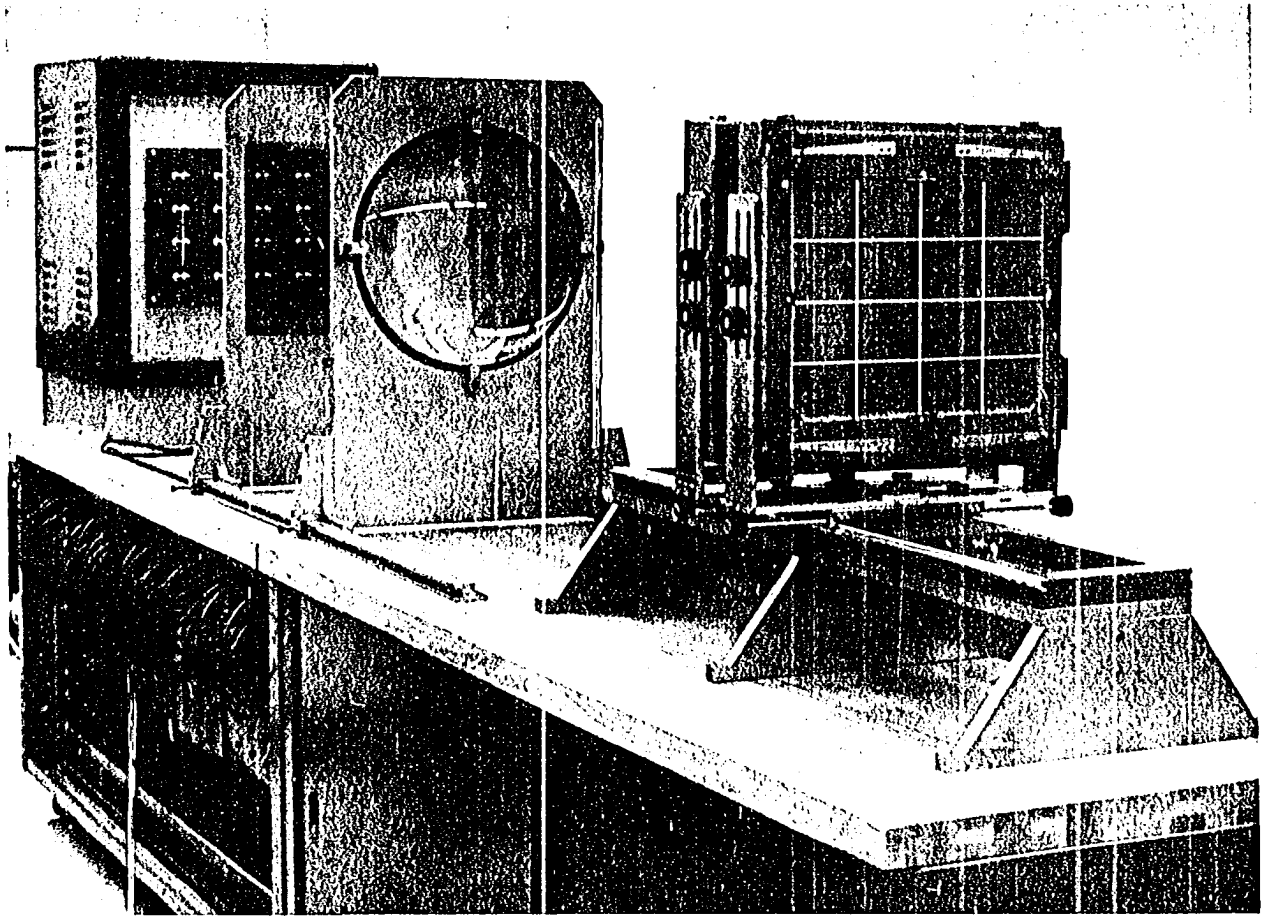

Figure 2. The multiple spark camera

calibration system. Each of these systems is expounded upon in detail in the following sections.

Spark Gap System

The spark gap system is comprised of all of the high voltage circuitry and hardware used to illuminate the model and to shutter the camera. The basic assembly of the system is a four by four rectangular array of spark gaps which are shown in Figure 3. The accompanying circuitry for the spark gap array (Figure 4) provides the means of energizing and discharging the system to accomplish the controlled cascading sequence of short-duration, high-intensity point flashes used to capture the dynamic photoelastic event. The sixteen pairs of electrodes in the spark gap array were constructed of 0.50 inch diameter solid brass spheres mounted on a high voltage insulation board by means of brass studs through ceramic insulators. The 0.25 inch spark gaps (G_1, G_2, G_3,..., G_{16}) were formed by aligning each electrode of a particular gap on 2.75 inch by 3.50 inch centers in agreement with the design conditions (Appendix A).

The electrical components that are used to produce the spark illumination are confined in a metal cabinet that is the established base ground. The energy necessary to accomplish the high voltage discharge across the gaps is accumulated in 0.05 MFD (15 KV-DC) capacitors, one of

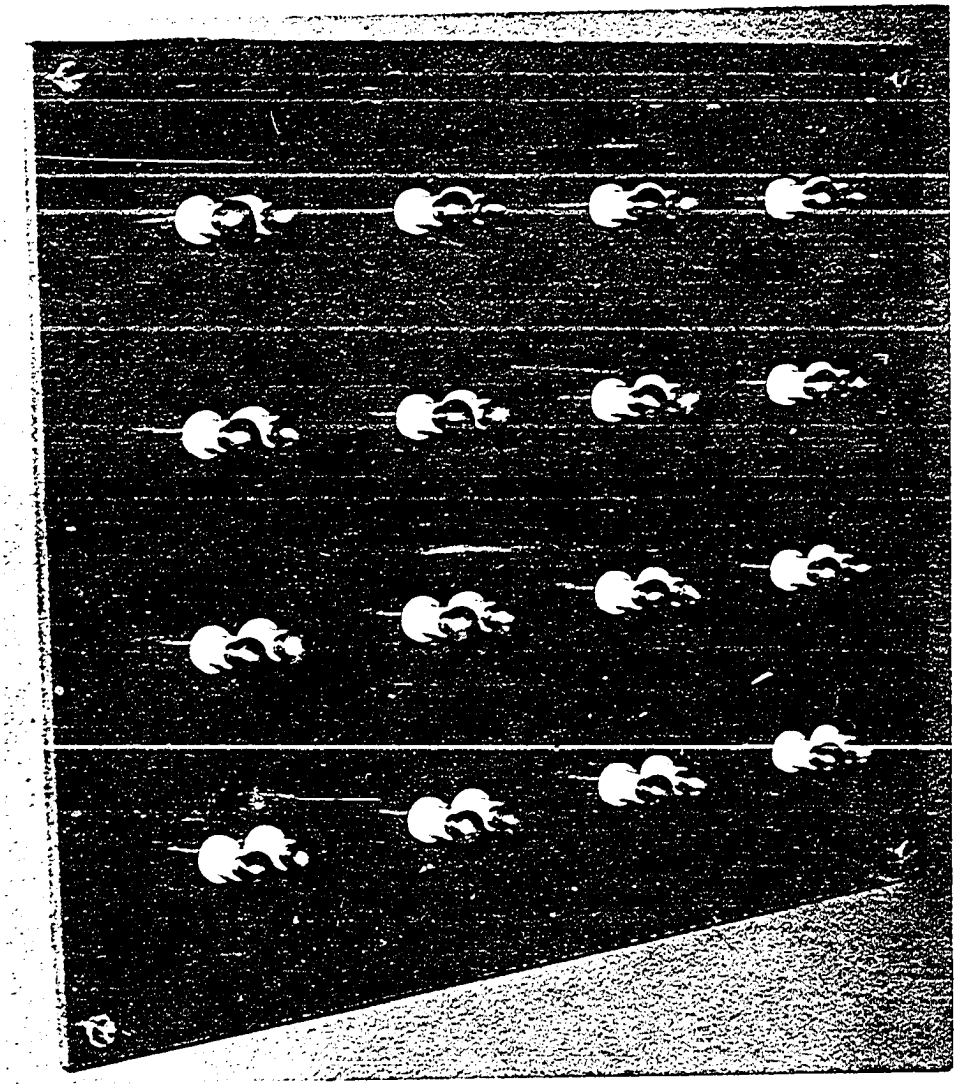

Figure 3. The spark gap array

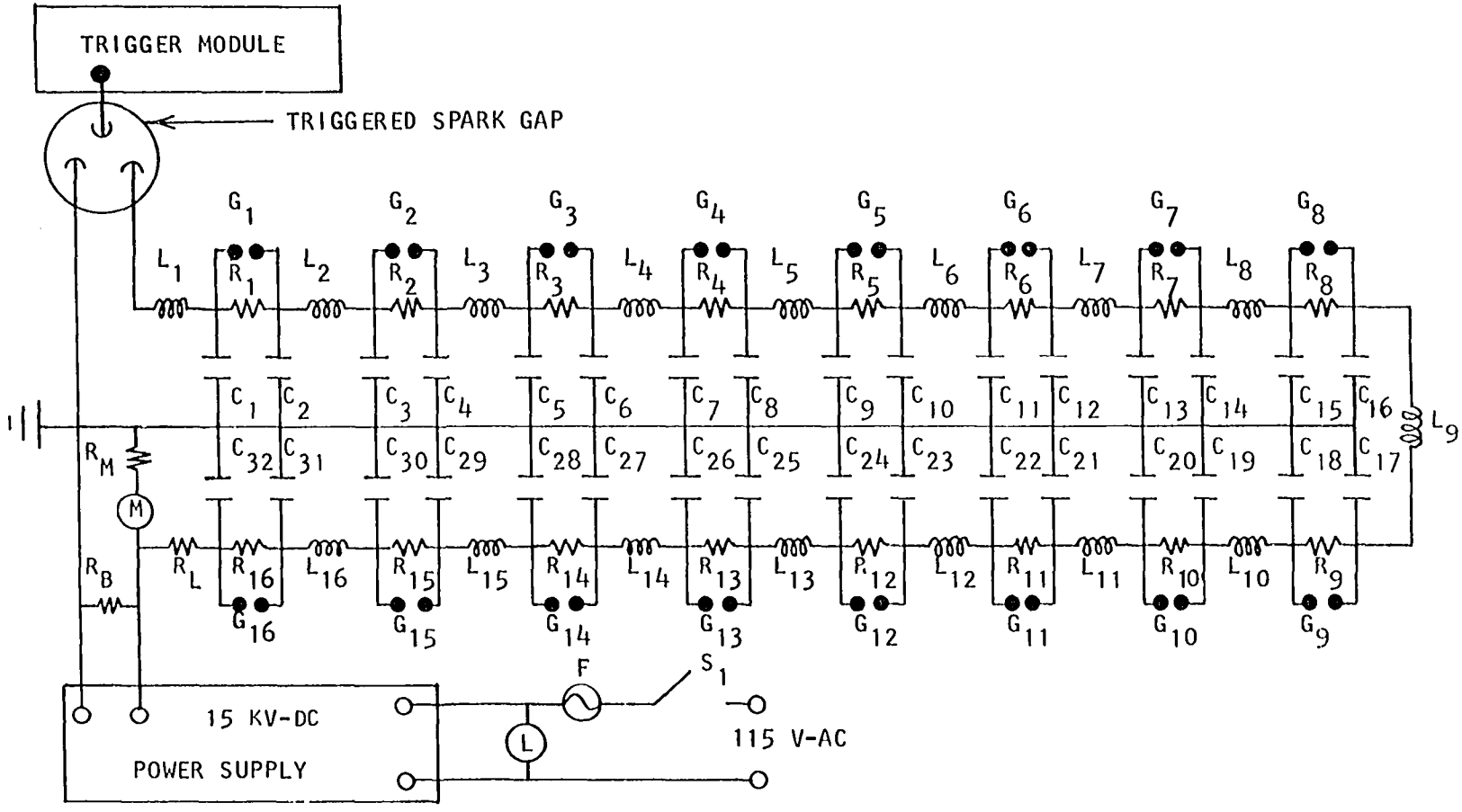

Figure 4. The spark gap system circuit

which is connected to each of the electrodes in the spark gap array. These capacitors (C_1, C_2, C_3,..., C_{32}) are energized by a 15 KV-DC (5 MA) power supply (Figure 5) to a positive 14 KV-DC. Since all of the electrodes are charged to the same potential, the spark gap array is considered stable as long as it remains an isolated system.

The span of time between the discharging of two gap locations, say G_1 and G_2, is a function of the values of the electrical components in the $C_2L_2C_3$ loop (Figure 4). When G_1 is discharged, the positive 14 KV-DC potential in C_3 decays in a sinusoidal manner until it reaches a negative value of approximately 14 KV-DC. This causes a 28 KV-DC potential difference in the two electrodes of G_2. The air in the gap is ionized and an arc of very intense light output (10 joules) of short duration (0.4μsecond) is struck across the two electrodes. The voltage in loop $C_4L_3C_5$ is set in oscillation and the sequence is repeated in a cascading manner throughout the spark gap array.

Since the capacitor bank is fixed at the above mentioned values, the series of sixteen inductors (L_1, L_2, L_3,..., L_{15}) are used to control the cascading sequence of discharging spark gaps. The framing rate is related to the inductance through Equation 73 (Appendix A). The inductor bank is housed in a metal cabinet under the optical bench. The cabinet is connected to the base ground in order to confine, as much as possible, the enormous electrical field

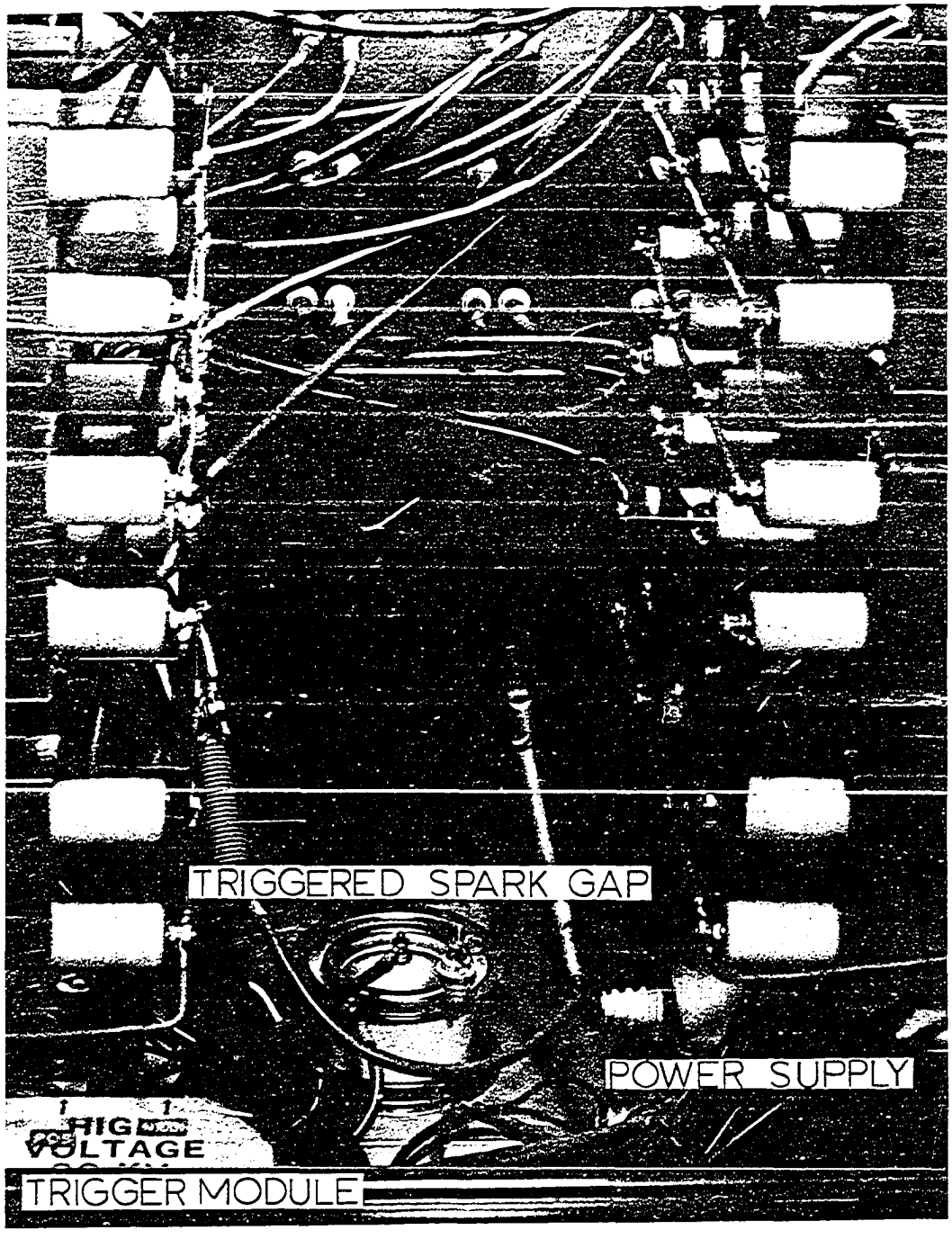

Figure 5. The high voltage assembly of the multiple spark camera

produced in charging the camera. Each inductor consisted of a continuous single layer of #20 plastic coated wire wound on two different diametered insulated fiber tubes (Figure 6) in accordance with the design conditions calculated in Appendix A. A series of eight electrical taps were installed on the windings of the two tubes of each inductor at predetermined locations. The taps were permanently connected by high voltage lead wires to an insulated patch board (Figure 7). Jumper wires, which are used to introduce the desired inductance into the high voltage circuit, allow the framing rate of the camera to be varied in discrete steps from 61,000 frames per second to 820,000 frames per second. Although there are only seven distinct inductance values commonly used (Table 3, Appendix A), 28 different framing rates are obtainable from different combinations of the eight tap locations.

Once the circuit is charged to 14 KV-DC, a 15 KV-DC pulse from a variable 1-20 KV-DC trigger module is applied to the third electrode of the triggered spark gap (Figure 5). This closes the L_1C_1 loop and initiates the firing sequence. The amount of charge on the camera at any given time is measured on a microampmeter that was installed in the high voltage circuit. The ampmeter scale was converted to indicate voltage directly by placing the meter in series with a 1000 meg-ohm resistor. The ampmeter, along with the trigger module and the power supply controls, are easily

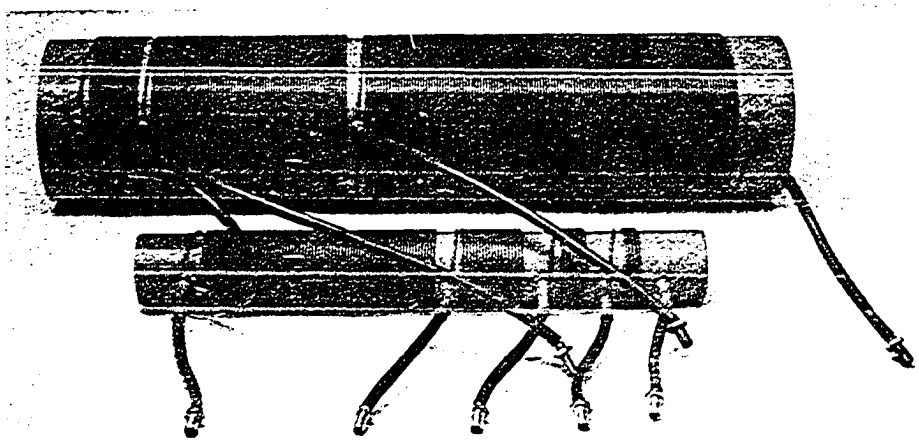

Figure 6. A single inductor configuration

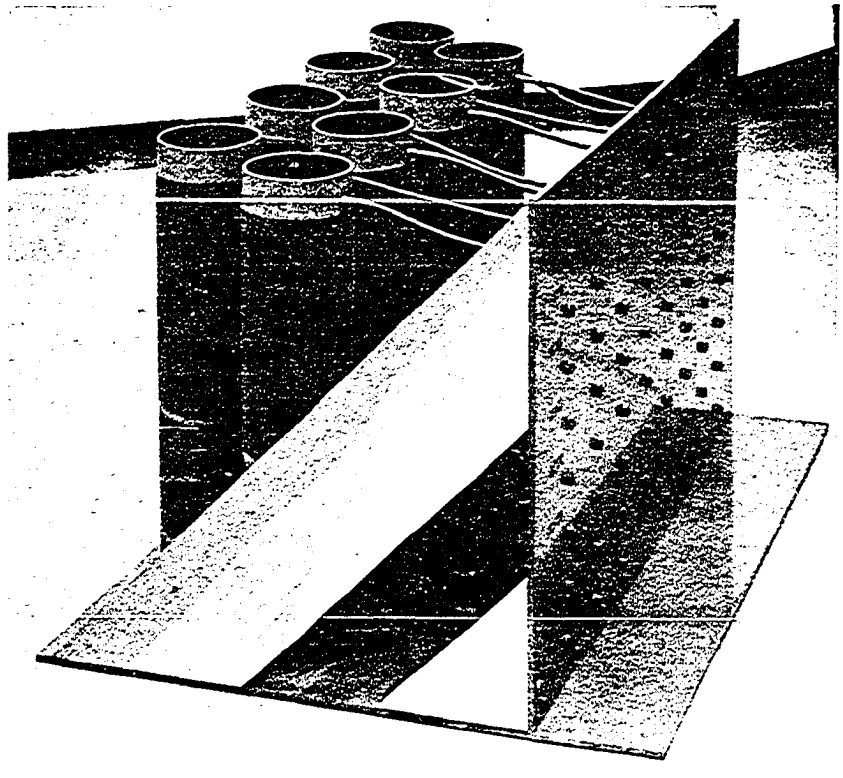

Figure 7. The patch board assembly for inductors L_1 through L_8

accessible from the back of the capacitor bank cabinet (Figure 8).

A 22.5 meg-ohm bleed down resistor was installed in the circuit such that the entire system would be completely discharged automatically regardless of the residual voltage left in the circuit after the camera has been in operation. A series of 1 meg-ohm resistors, one of which spands the electrodes of each gap, (Figure 4) were needed to allow the system to be initially charged.

Optical System

The optical system performs two distinct functions which include the polarized illumination of the model (Figure 10) and the recording on film of a sequence of separated focused model images of sufficient magnification for analysis (Figure 11). The optical elements of the system consist of a 16 inch diameter field lens (Figure 9), two circular polaroids (HNCP-38), and an array of 16 camera lenses mounted on an 11 inch by 14 inch view camera (Figure 12).

The illumination is accomplished by arranging the optical elements such that the high intensity flash from an individual spark gap is optically projected by the field lens and entirely collected by a single lens in the lens array. In this manner, the sixteen spark gaps will produce sixteen separate illuminations of the photoelastic field which are projected by the lenses of the lens array onto

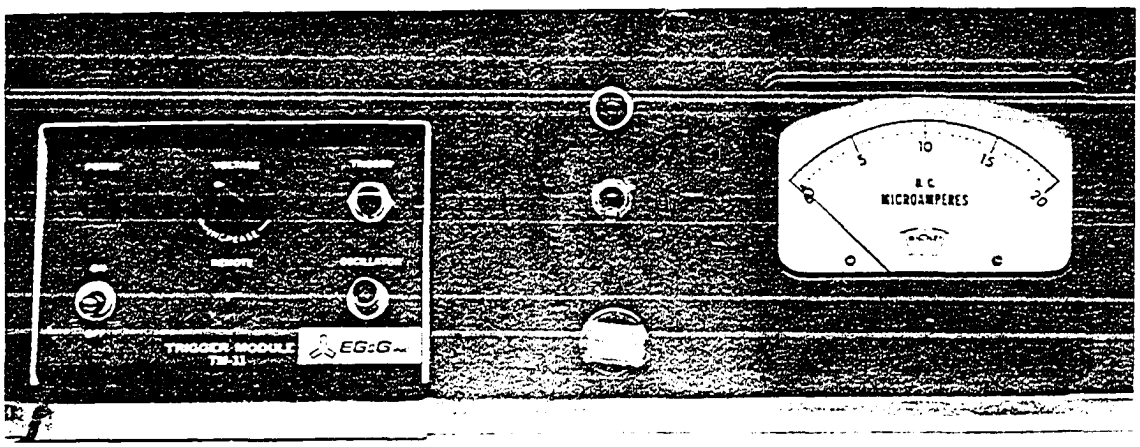

Figure 8. The high voltage assembly cabinet

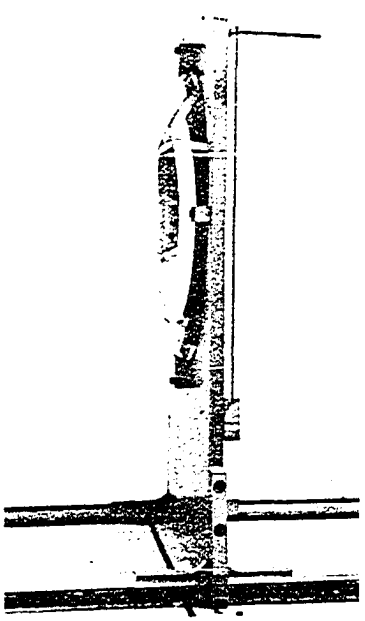

Figure 9. The field lens system

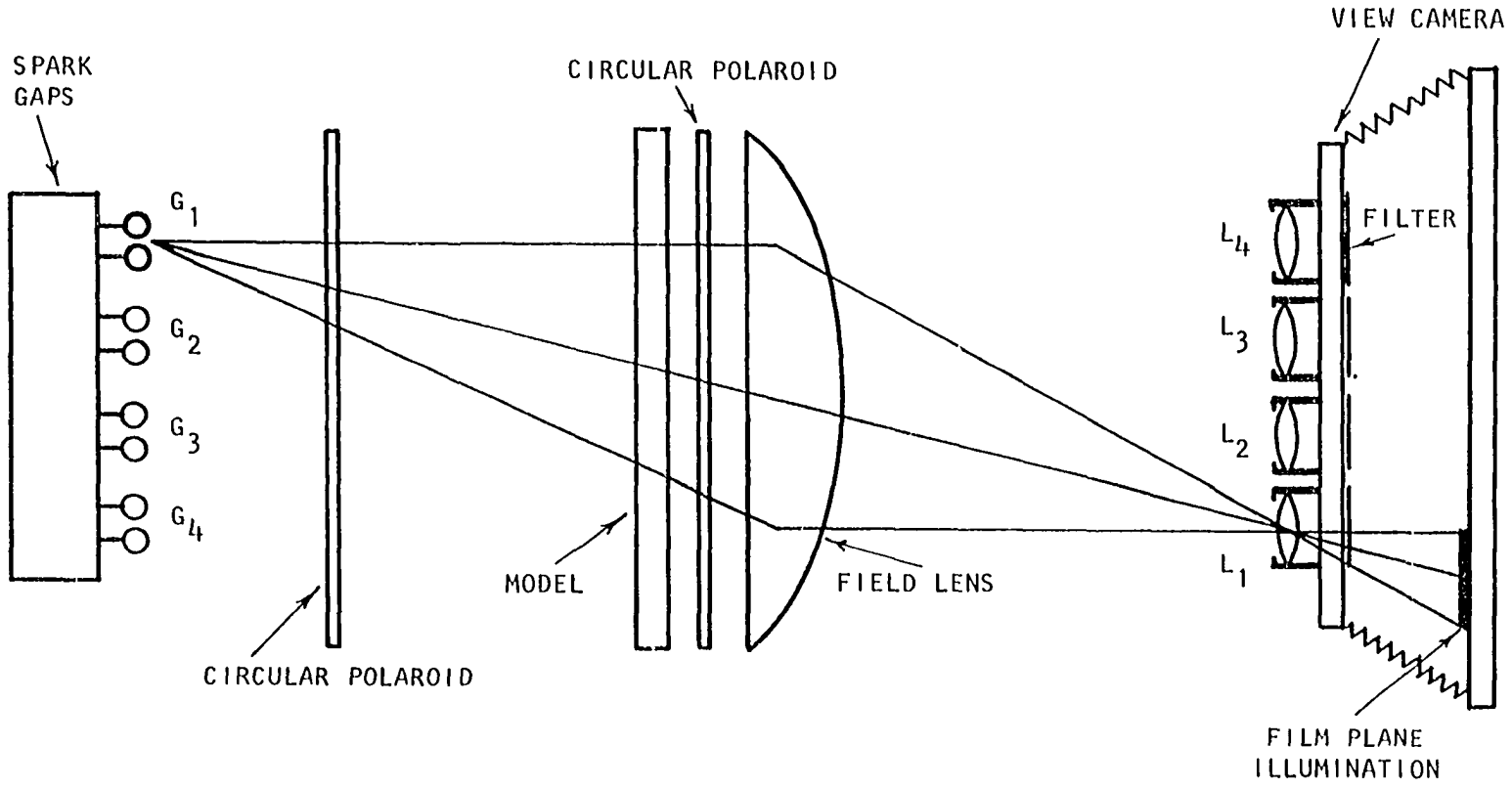

Figure 10. The optical alignment of the illuminating system

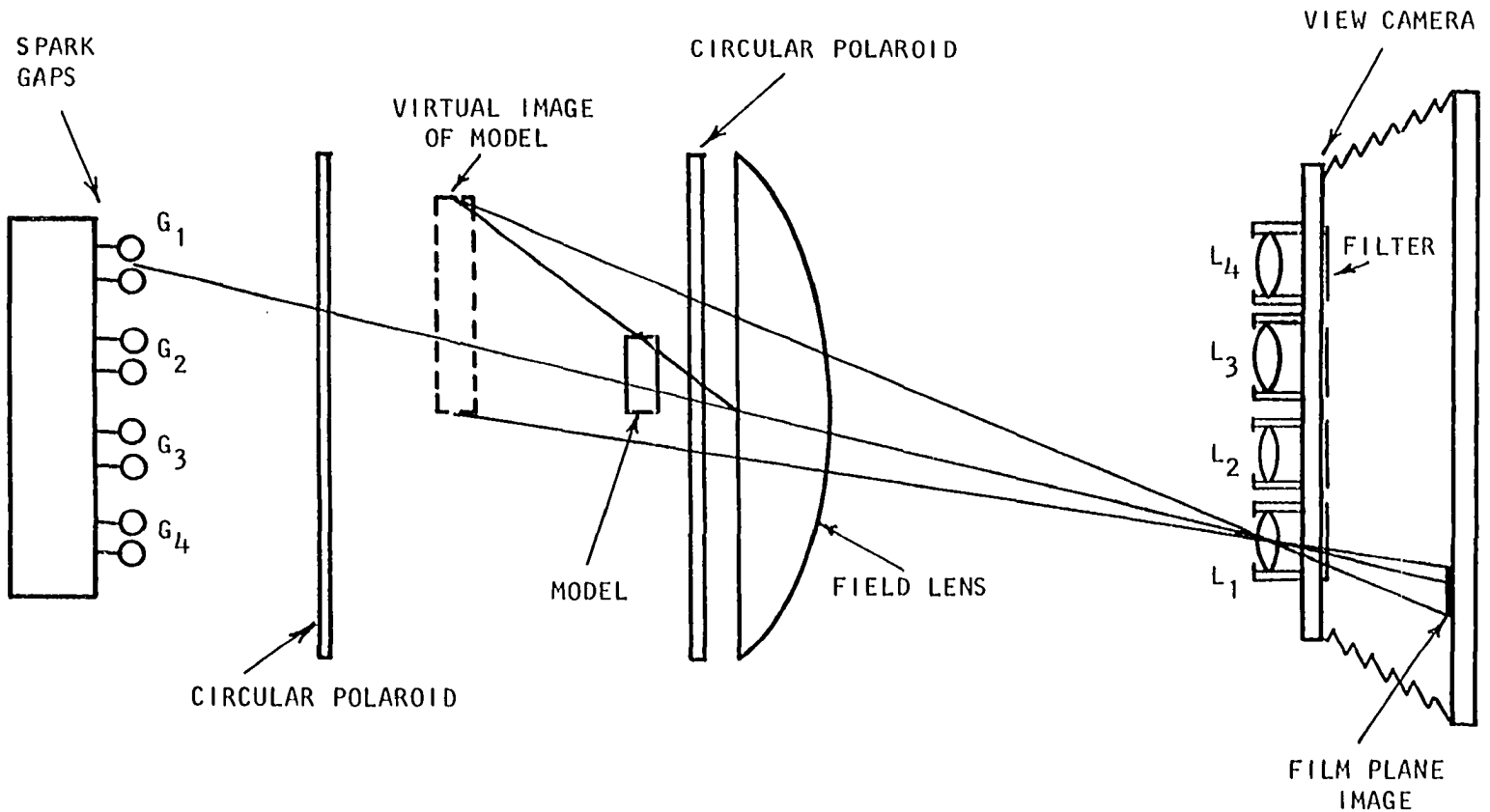

Figure 11. The optical alignment of the camera recording system

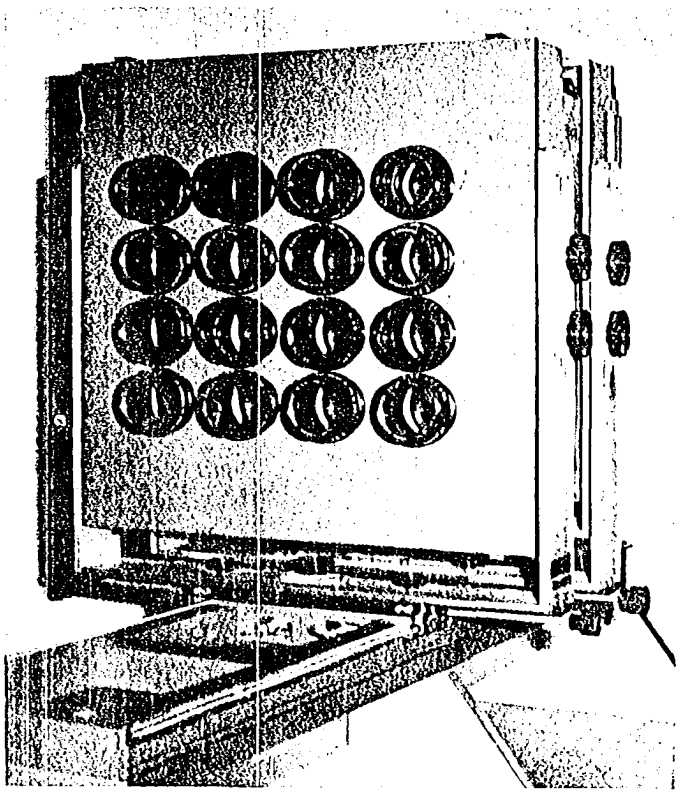

Figure 12. The lens array

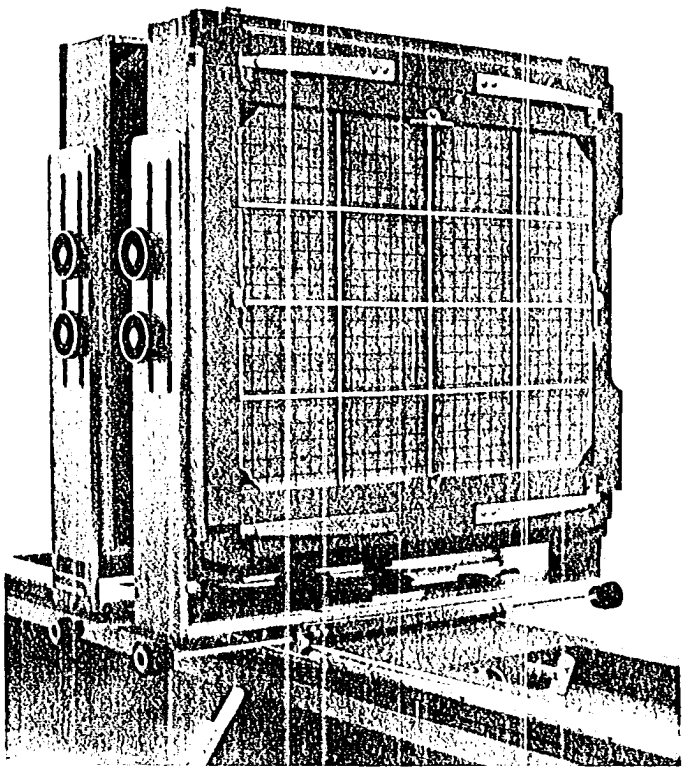

Figure 13. The camera back

an 11 inch by 14 inch film plane (Figure 13). The projection of a focused and illuminated, undistorted model image onto the film plane is accomplished by the careful alignment of the model and optical elements in accordance with design conditions presented in Appendix B. To assess the tolerances that are allowed in the optical alignment of the elements, the image recording system and the illumination system can be examined independently. The image of the model can be focused easily onto the film plane with a large latitude in element alignment if the spark gap illumination requirements are ignored. In the same manner, the light from each gap can be projected through the lens system to produce a wide range of illumination on the film plane if the image focus requirements are not considered. The fact that both the illumination and the undistorted focused magnification of the model must be compatible on the film plane introduces the necessity of a small latitude in tolerances in the alignment of the optical system as shown in Appendix B.

Two combinations of circular polaroids are used to produce the dynamic photoelastic polariscope within the lens system. The sheet of circular polaroid that the light initially passes through was laminated between two sheets of glass which were placed in a rectangular mounting, Figure 2. This element remains at a fixed orientation in the system. The second laminated circular polaroid is held in the optical

field in an easily accessible recessed mounting on the flat side of the field lens assembly (Figure 9). This element is interchangeable between two orientations of a polaroid and quarter wave plate combination that can provide for either light or dark field polarization of the illuminated field when properly inserted in the recessed mounting. The option of providing for a means of rotation of the elements was waivered in the original design in lieu of the unfeasibility of changing the element orientation during a transient dynamic event.

The field lens is a 16 inch plano-convex condensing lens with a focal length of 24 inches. The lens is not of a stress relieved quality, which would have tripled the cost, since it is not located in the polarized field.

Each of the sixteen f-4.5 lenses (focal length - 7.5 inches) used to construct the view camera were of very high optical quality. Since it was desirable to minimize the angle of incidence of the light passing through the model and the lens system (page 205, Appendix B), the optical elements as well as the illumination gaps were located as close to the optical axis as physically possible. Because of the physical diametrical dimension of 2.25 inches of each view camera lens, a minimum of 2.375 inches between the optical centers of the lenses was established as the base for the alignment design of the optical system. In order to evenly space the images on the film plane with

an 11 by 14 ratio, the horizontal spacing of the lens array was on 3.02 inch centers. The typical element and model alignment used for this study of wave mechanics produced a model image magnification of -.21.

A discharge of electricity in the air between two electrodes produces a flash of light that includes most of the wave frequencies in the visible spectrum although it peaks between 3500 to 5100 angstroms. Therefore, a Kodak Wratten filter (No. 34-A) was inserted in the field of each of the view camera lenses to minimize the transmitted light band to a region between 4900 to 5100 angstroms in order to approximate monochromatic light. Since colored (white light) pictures are sometimes desirable, the filters were mounted behind each of the sixteen lenses on a sheet of glass that could easily be removed from the back side of the lens array panel.

Synchronization and Calibration System

In order to photographically record a sequence of photoelastic stress wave patterns that are produced in a temporarily birefringent material by an explosive load, a reliable sychronization system had to be employed to capture the event that is terminated in 10 to 300 microseconds.

The central nerve center of the synchronization system is a Tektronix Type 547 Oscilloscope (Figure 14) which has a time delay mechanism built into the main time base B.

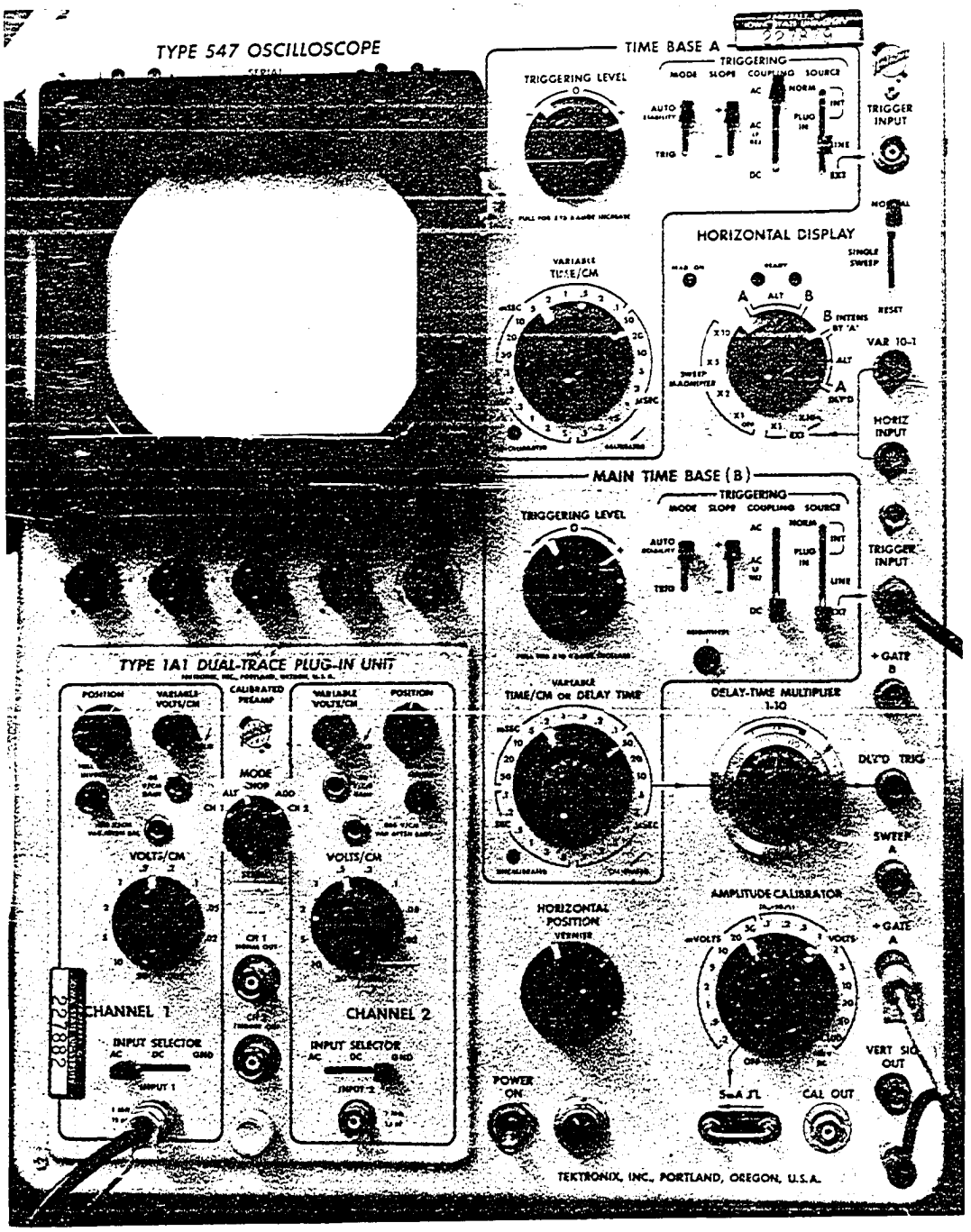

Figure 14. The synchronization oscilloscope

A 20 volt pulse received at the trigger input terminal of time base B is required to activate the sweep as well as the delay generation circuit in the oscilloscope. At the end of the preset delay period, a shielded lead from the gate A output terminal transmits a positive 20 volt pulse to a silicon controlled rectifier (SCR) mounted within the trigger module. The module amplifies the pulse to 20 KV which is discharged across the triggered spark gap initiating the firing sequence of the camera.

In order to establish an accurate calibration of the framing rate of the camera for each test, a properly adjusted (Appendix D) high frequency photodiode (EGG Lite-Mike) is used to sense the time sequel illumination from each gap (Figure 15). The Lite-Mike then transmits a low voltage signal to the vertical trace input of the oscilloscope where the firing sequence is permanently recorded on polaroid film (Figure 16). Since the sweep of the trace is activated internally by the initial 20 volt triggering signal, the actual time delay from when this signal is sensed until the camera begins to shutter is also obtainable from the oscilloscope trace. An expanded view of two sequential sparks (Figure 17) indicates the short duration of the rise time (less than 1 microsecond).

Figure 15. The photodiode framing rate calibrator

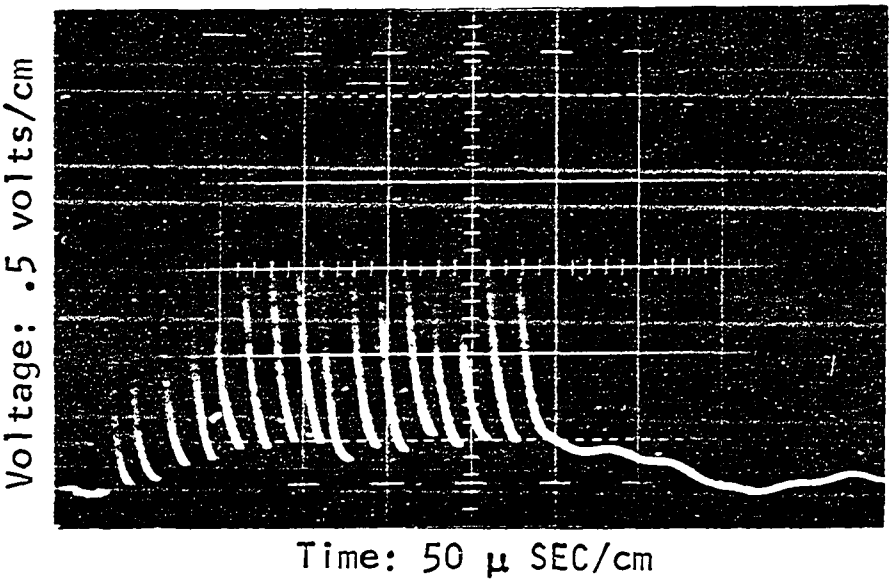

Figure 16. Relative ligh intensity as a function of time

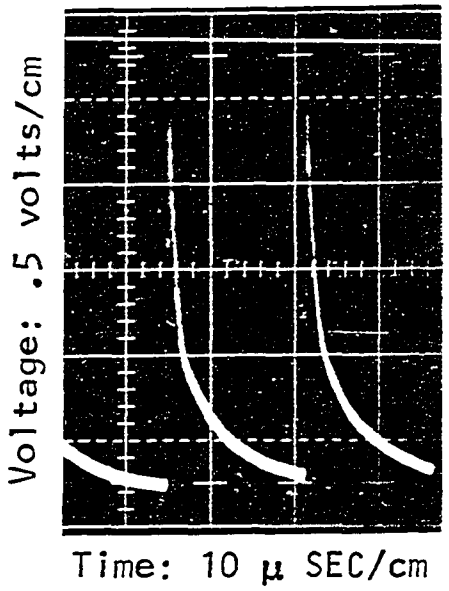

Figure 17. Expanded light intensity record

Detonation Systems

Since the photographic system is electronically regulated once the oscilloscope receives the 20 volt pulse, the circuitry needed to detonate the explosive was designed to be compatible with this system for complete synchronization of the dynamic test. Depending on the information that was desired, three different detonation systems were developed to ignite the explosive and initiate the dynamic event. These are categorized as the exploding wire, the heating wire, and the arcing wire systems.

Exploding wire system

The exploding wire system (Figure 18) is the standard means of ignition used in most of the earlier constructed multiple spark cameras (53), (62). Although this system is the most time consuming of the three systems in experimental set up, it is the only feasible method of initiating an event involving a multiple explosion (56). The circuit (Figure 19) was designed such that when switch S_1 is closed, a 2 KV pulse as well as a 20 volt pulse are simultaneously available from the terminals shown on the circuit housing in Figure 20. The 2 KV pulse is used to explode a 0.001 inch diameter cupro-nickel bridge wire detonator (Figure 21) which is mounted in the charge cavity of the test model. The 20 volt pulse is transmitted to the trigger input of the oscilloscope. Since the time delay from the closing

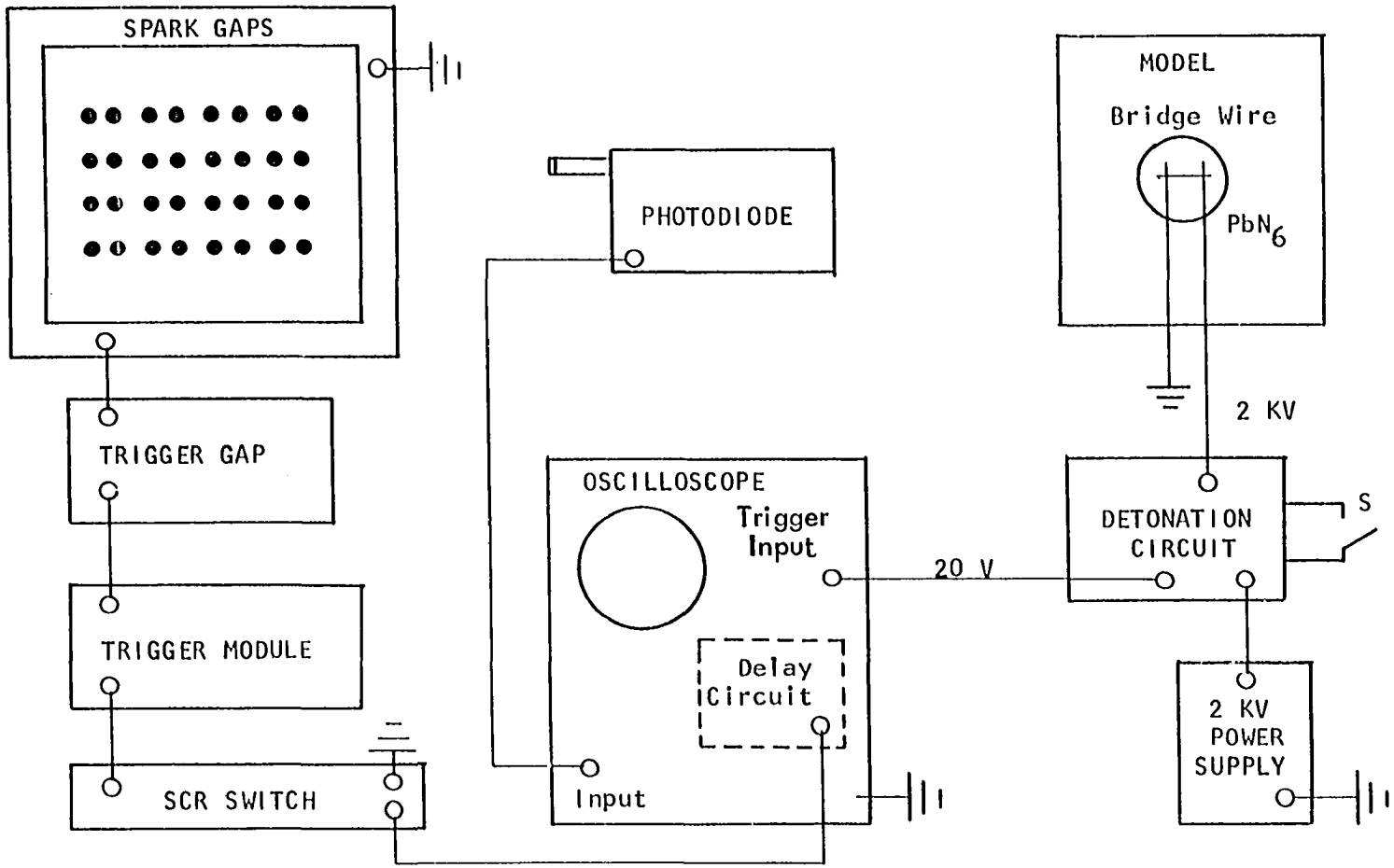

Figure 18. Block diagram of the exploding wire system

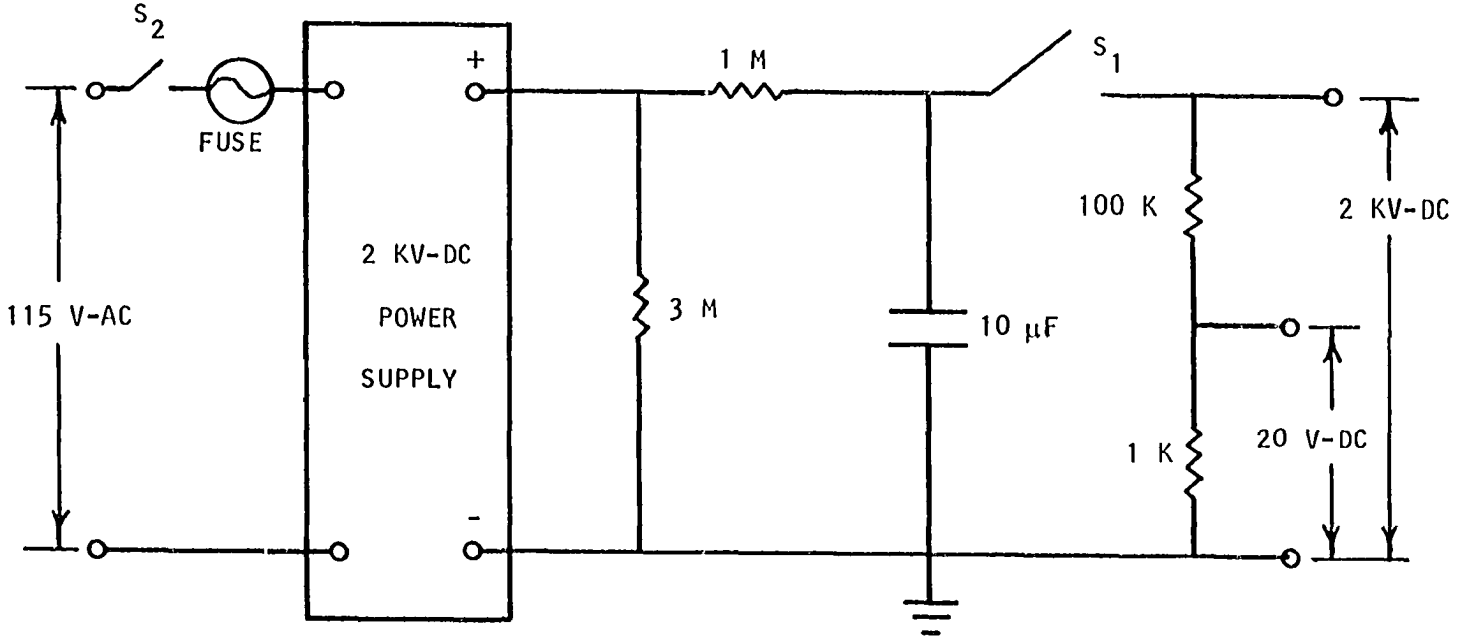

Figure 19. The exploding wire detonation circuit

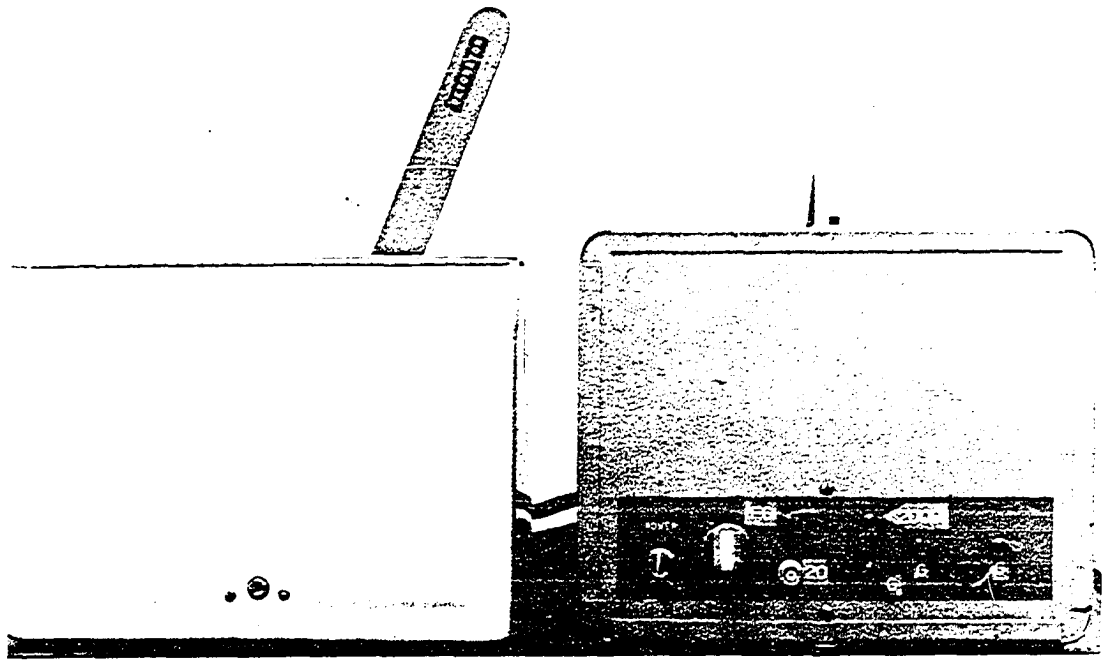

Figure 20. The detonation circuit housing

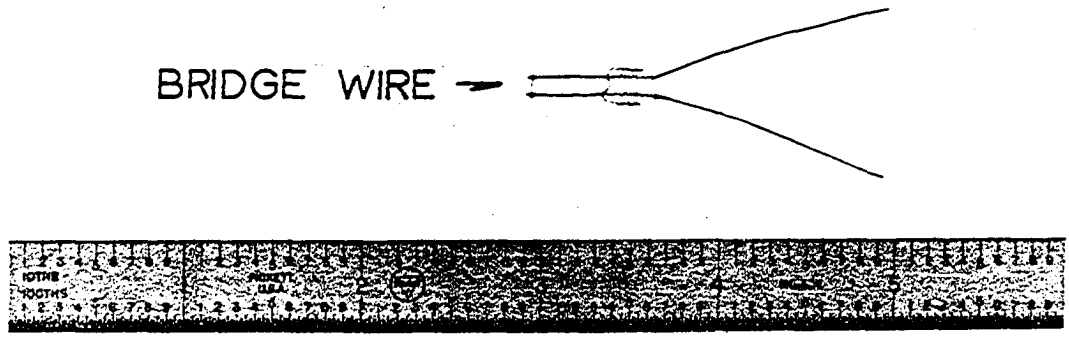

Figure 21. The cupro-nickel bridge wire detonator

of the detonation switch until the two pulses have performed their predetermined function is less than a microsecond, any inherent delay of sizeable magnitude in the system can be obtained from the oscilloscope trace. Because the inherent delay in this system was found to be approximately 24 microseconds, the first photographic recording of any event does not occur until the wave is several inches into the model. Although this precludes its use for obtaining data close to the explosive charge, it still remains a reliable system for use in far field experimental wave propagation since the framing sequence of the camera can be accurately delayed from 24 microseconds until any desired length of time.

Heating wire system

The heating wire system (Figure 22), which was developed for the present multiple spark camera for use in far field studies, involves the coupling of a heating wire, which ignites the explosive, and an electronic light sensor, which acknowledges the initiation of the event (Figure 23). The heating mechanism consists of a 0.012 inch diameter chromium alloy wire which is connected through electrical leads to a 10 ampere DC power supply. The wire is mounted such that it can be easily brought into contact with the explosive charge placed in a model which is mounted in the camera field (Figure 25). The output voltage of the power

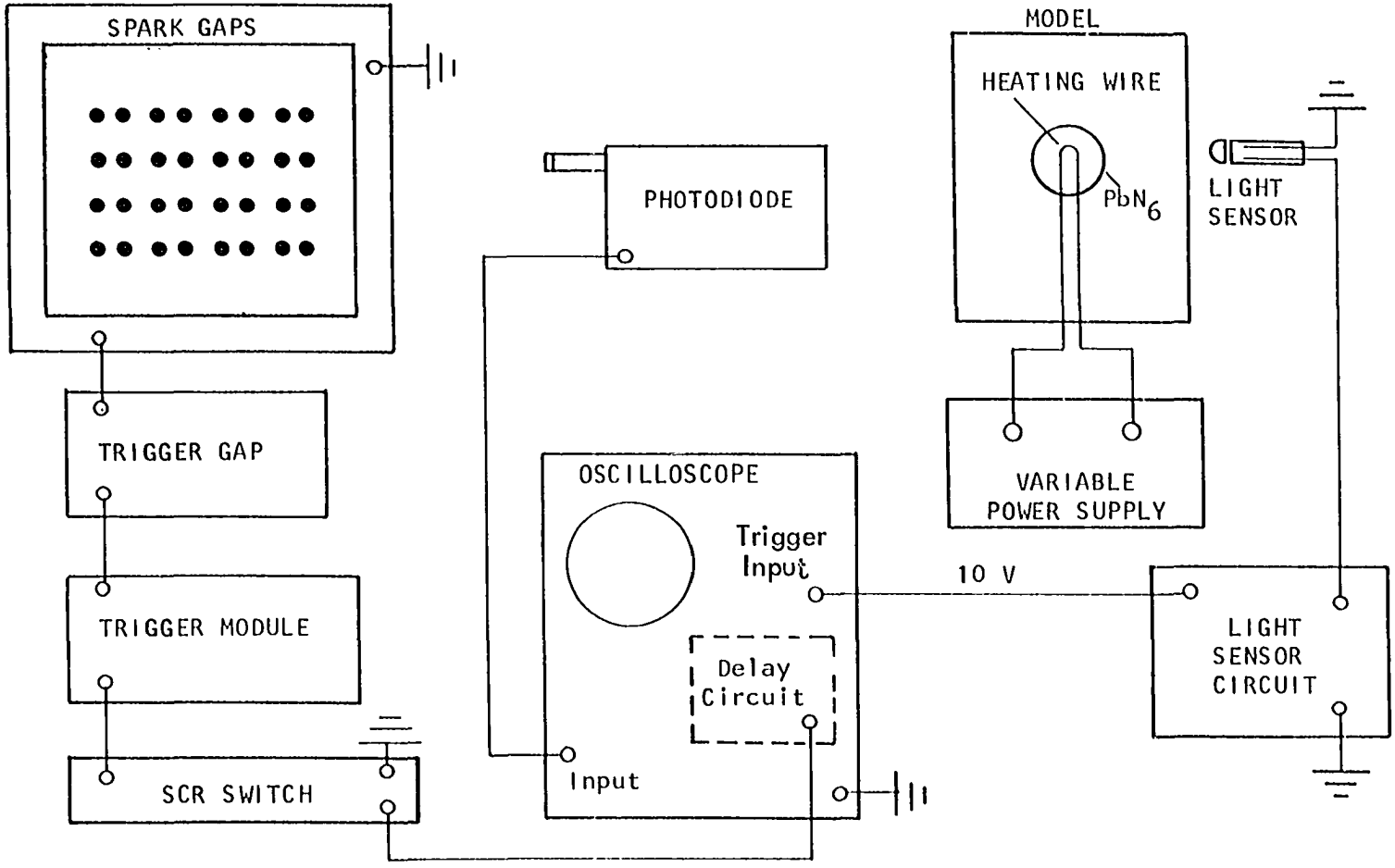

Figure 22. Block diagram of the heating wire system

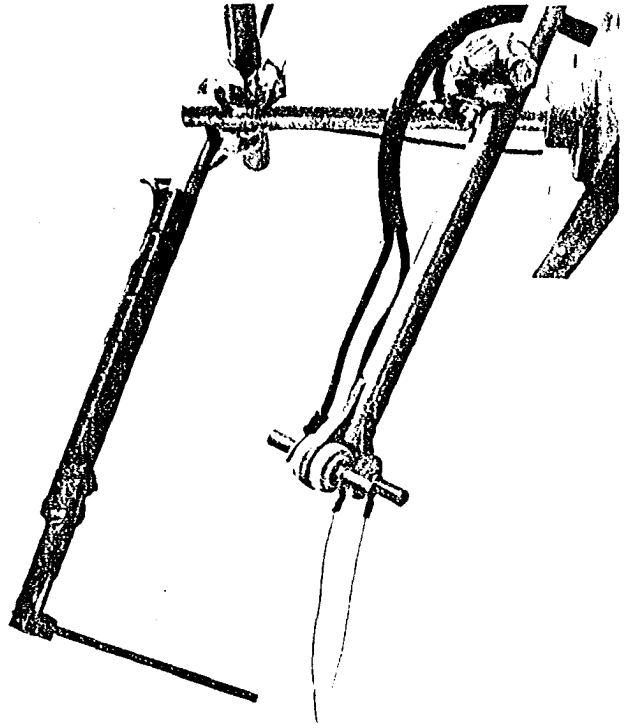

Figure 23. The heating wire and light sensor assembly

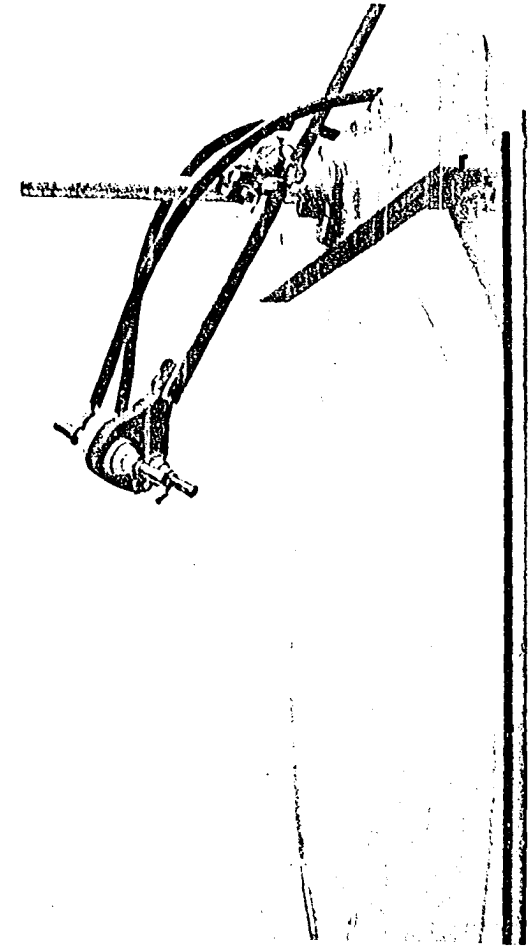

Figure 24. The arcing wire electrodes

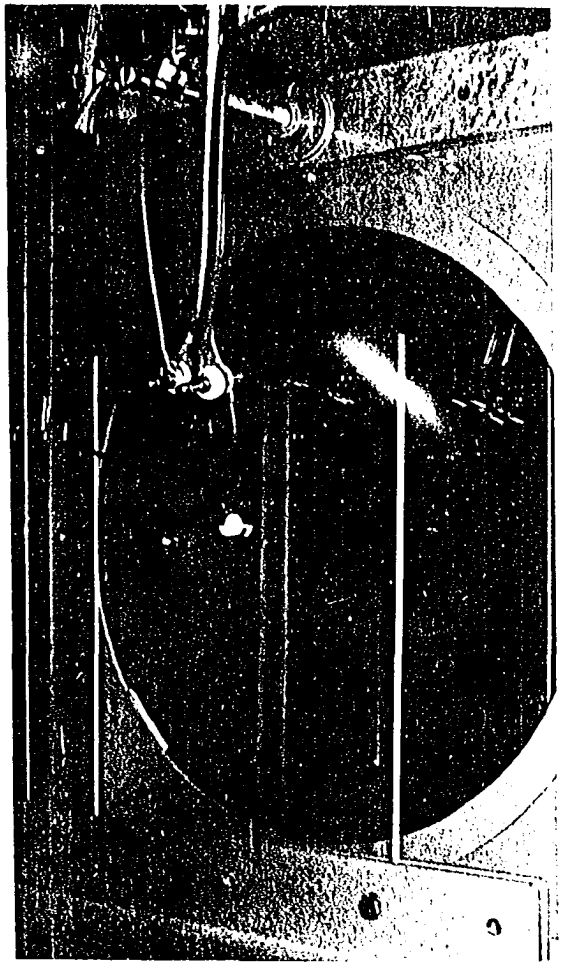

Figure 25. The heating wire and model arrangement

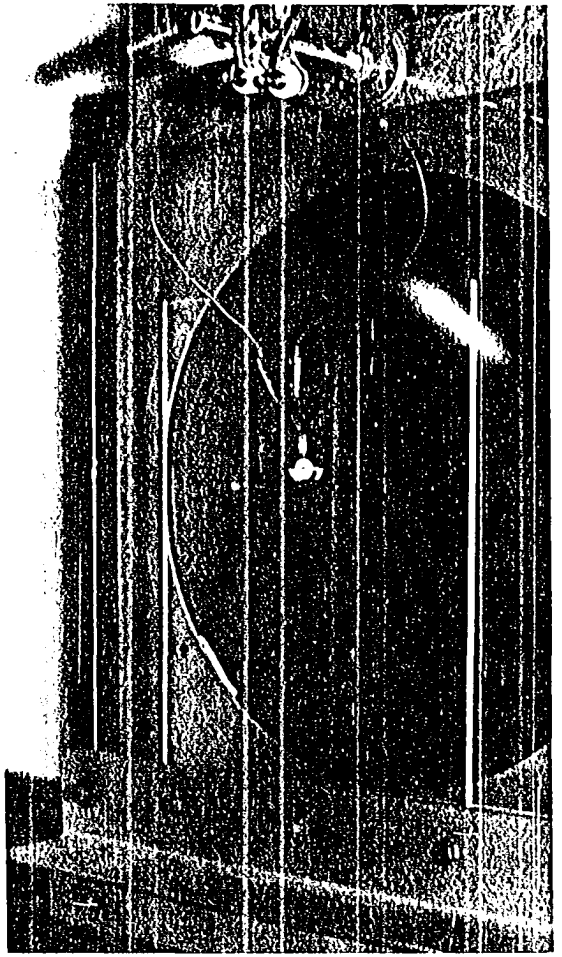

Figure 26. The exploding wire and model arrangement

supply is gradually increased in the chromium wire until it reaches a sufficient temperature to ignite the explosive. The illumination of the detonating explosive is transmitted through a 0.125 inch diameter fiber optic tube to a lensed sensor (T.I.I.- IN 2175). The light sensor information is converted by the circuit shown in Figure 27 into a 10 volt pulse that is sent to the trigger input of the oscilloscope. Since the rise time for 90 per cent continuity of the light sensor circuit is 2 microseconds, the only inherent delay in the synchronization system is the 24 microseconds which are expended between the time the oscilloscope receives the signal until the first gap illuminates.

The main advantage of the heating wire system is that the experimental set up time is much shorter than that needed for the exploding wire system. For the exploding wire circuit, elaborate shielding is necessary to isolate the arcing of the knife switch, the surging of the 2 KV pulse through the detonation circuit, and the electrical discharge of the exploding wire. Even with the shielding, the exploding wire system was found to trigger the delay mechanism of the oscilloscope prematurely in some isolated cases. Therefore, the heating wire eliminates all electrical noise problems from the detonating circuit. The only disadvantage of the heating wire over the exploding wire is that the type of explosive is limited to one that does not need a large amount of energy to ignite. This usually

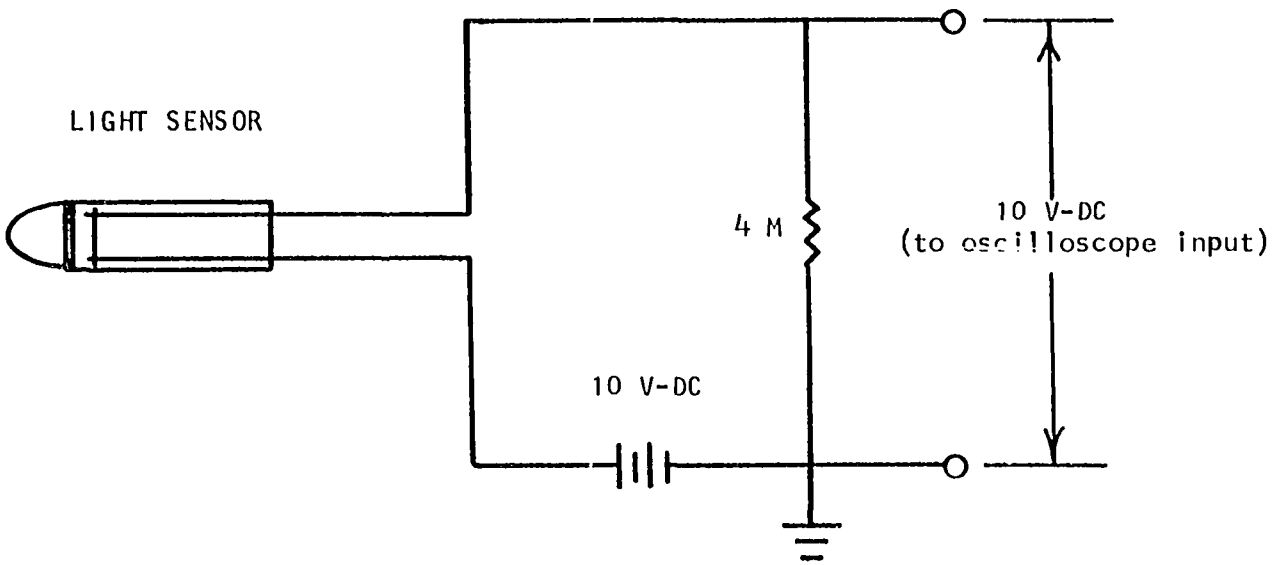

Figure 27. The light sensor circuit

means employing a primary explosive such as mercury fulminate or lead azide which must be handled with extreme care.

Arcing wire system

In order to photographically record a stress pattern as it is being transmitted into the model by the explosive, the arcing wire system (Figure 28) was developed. This allows for photographs of the event to be recorded from the exact moment the charge is ignited until a maximum of 256 microseconds after detonation. This system is basically an extension of the first spark gap location into the explosive charge. This is accomplished by connecting two high voltage leads from the electrodes of the first gap to a pair of chromium alloy wires that are inserted into the explosive (Figure 24).

The 20 volt output of the detonator power supply shown in Figure 20 is used to activate the trigger input of the oscilloscope. Although the sweep is started at this instant, the charge is not detonated until the arcing sequence of the spark gaps is initiated. Therefore, any delay indicated on the oscilloscope record occurs before the initiation of the event. Since the two high voltage leads from the first spark gap are connected in such a manner as not to interfere with the illumination from the first gap, the voltage is divided between the gap and the

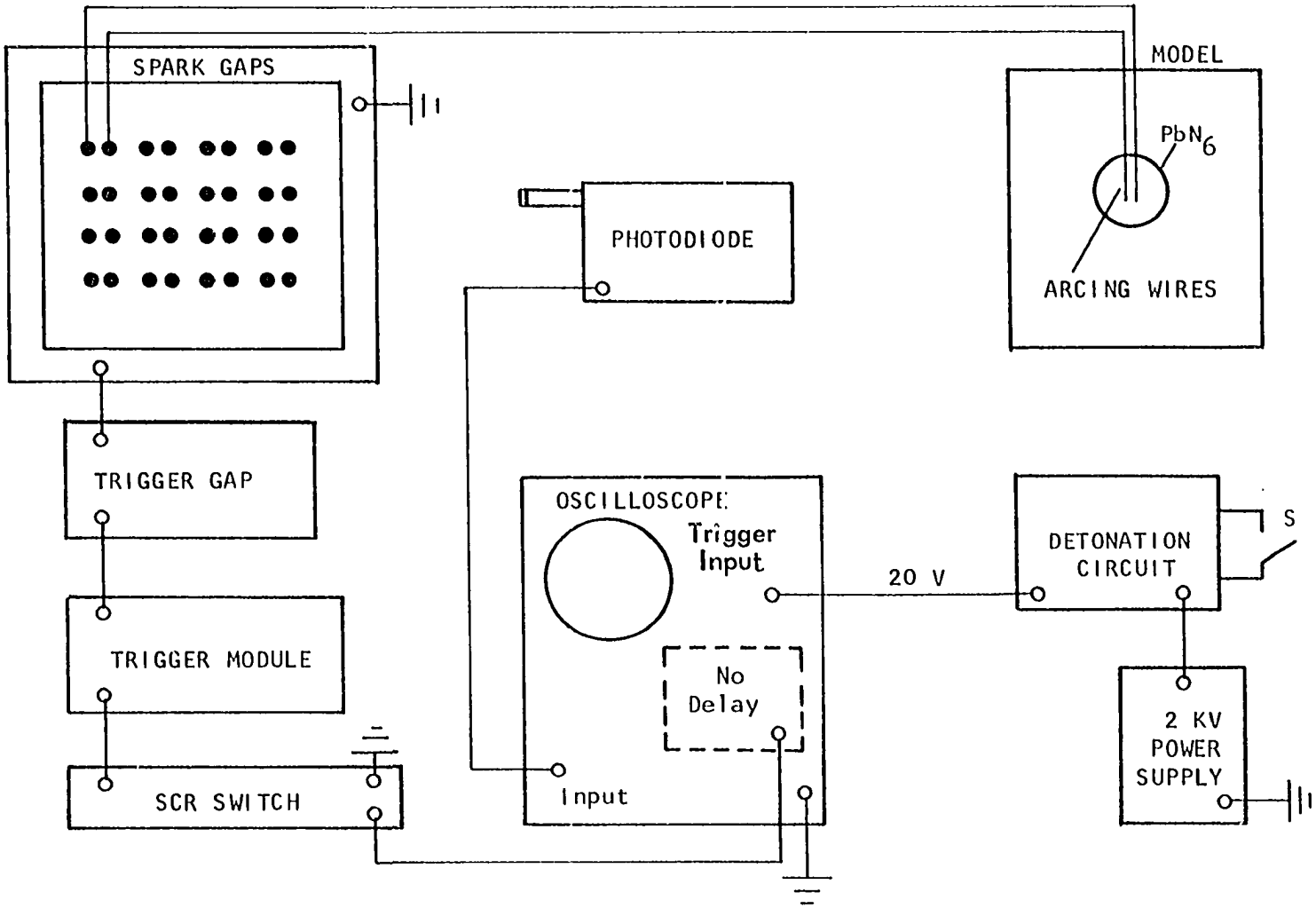

Figure 28. Block diagram of the arcing wire system

electrical wires in the explosive. This does not seem to affect the function of either set of electrodes.

In some instances in the current study it was desirable to use this system with a cupro-nickel bridge wire that was mounted in the explosive in lieu of the arcing wires (Figure 26). The only danger in this system is that the high voltage circuit is initially charged to 14 KV potential through the bridge wire and thus the explosive.

The hardware for all synchronization and detonation systems was arranged in such a fashion that convenient operation from behind the capacitor cabinet was permissible for protection against accidental visual exposure to the harmful rays of the sparks and flying debris from the explosion (Figures 29 and 30).

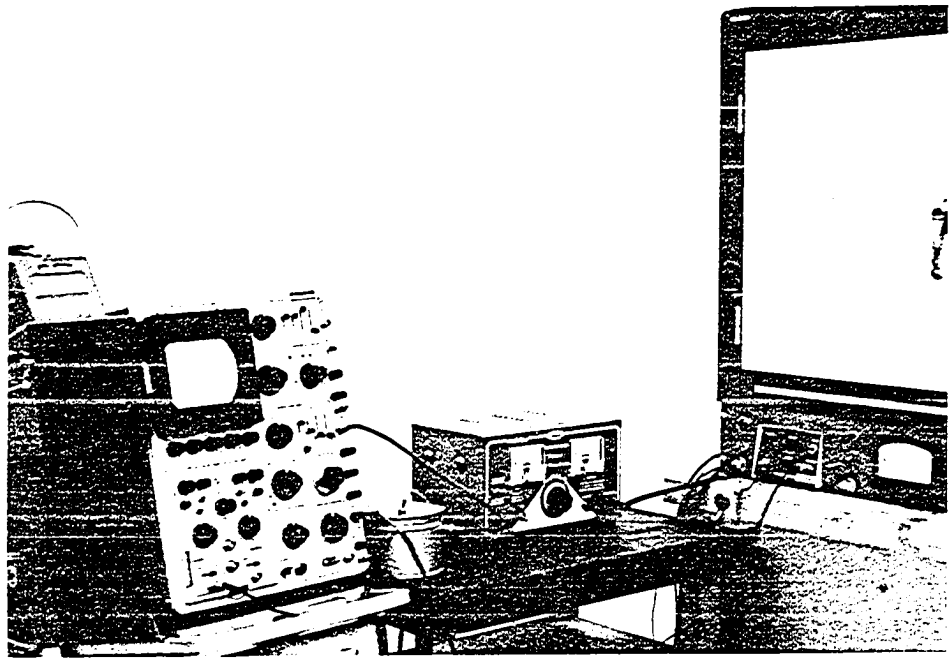

Figure 29. The heating wire synchronization control hardware

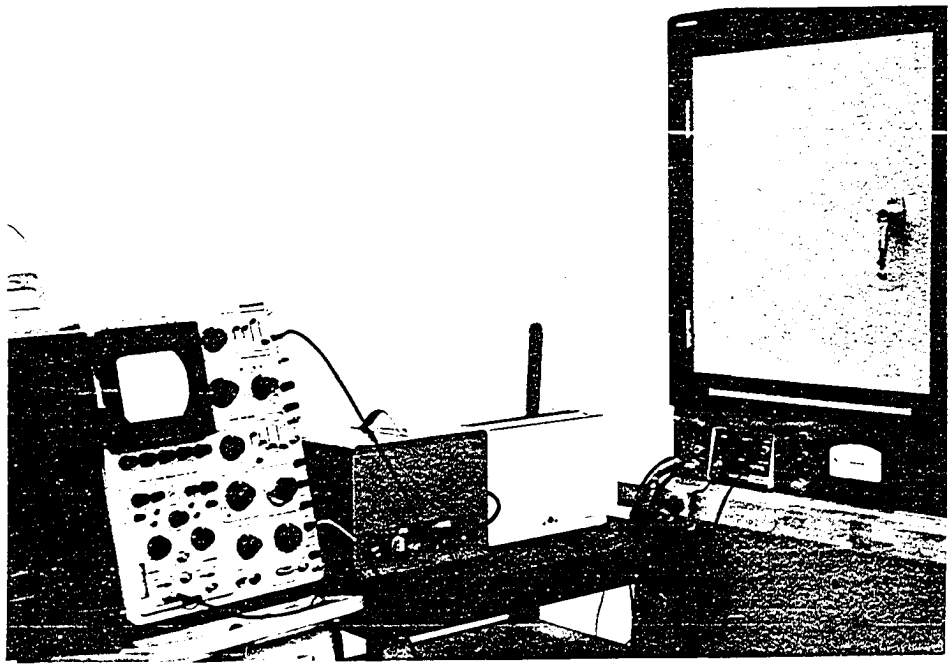

Figure 30. The exploding and arcing wire synchronization control hardware

MODEL MATERIALS

The selection of a model material to be used for a photoelastic analysis of stress wave propagation is governed by the objective of the investigation and by the type of photographic system to be used for recording data.

Material Properties

Several investigations have considered the optical-mechanical response of model materials under various dynamic loading conditions (50), (53), (131-132). Low modulus materials, such as the urethane rubbers (E around 500 psi) have wave velocities that are low enough that adequate fringe photographs can be obtained with the relatively simple moderate speed camera (about 16,000 frames per second). However, these materials usually deform extensively under loading and have the undesirable feature of being viscoelastic rather than elastic (35), which may result in some error if a classical-elastic theory is assumed. On the other hand, some of the higher modulus glassy materials (about 300,000 psi) approximate elastic behavior with small deformations under conditions of very high strain rates. This can be explained by considering Mindlin's theory that any viscoelastic material can be simulated mathematically by a sufficient series of dashpots and springs (67). Therefore, an event that occurs over a

very short length of time does not provide sufficient time for the viscous (dashpot) mechanism to come into play. In this circumstance, the quasi-elastic material can be considered elastic for practical purposes. Of course, a stress wave moving in a high modulus material has a velocity of such a magnitude that it can only be captured with an ultra high speed photographic system (over 100,000 frames per second).

In the multiple spark camera, approximately 99 per cent of the original light output of the gaps is lost during transmission through the optical system. Therefore, models with a high degree of light transmissibility are the most desirable for dynamic tests.

For close field studies, the material must be relatively insensitive optically if the fringe gradients are to be resolved at the extremely high stress levels encountered near the explosive pulse. For far field work, the material should have sufficient optical sensitivity so that a reasonable amount of optical response is still present in the far field where waves are of much smaller magnitude due to geometric attenuation. Obviously, one material will not satisfy both these criteria; therefore, two materials of similar mechanical properties, but different optical properties, were sought for the current study.

Several materials were initially investigated for mechanical and optical suitability of their properties. Two

model materials, allyl diglycol carbonate (CR-39) and polymethymethacrylate (Plexiglas), which satisfy most of the above requirements, were employed in this investigation. These materials were readily available and could be machined with considerable ease with a high speed (24,000 rpm) router.

Allyl diglycol carbonate

Allyl diglycol carbonate, columbia resin CR-39, which is a member of the allyl carbonate series of thermosetting plastics, was purchased from the Homolite Corporation in the form of 24 inch by 36 inch sheets 0.27 inch in thickness. Although this material is optically transparent, previous investigators (132-133) have shown that it exhibits both optical and mechanical creep. Since the properties of CR-39 are dependent on loading rate and since CR-39 continues to polymerize with age, static and dynamic calibrations must be conducted shortly before it is used in actual tests.

Clark developed a technique for a dynamic calibration from a static test (132). By placing a piece of CR-39 in tension under a state of constant stress, he observed that the fringe order increased due to optical creep. A plot of fringe order versus time on a semi-logarithmic scale produced a near linear relation between the material fringe value and time. The plot was then extrapolated to

determine the material fringe value at different points in time. Clark verified his method in the short time region ($t = 10^{-5}\mu$ sec) by obtaining additional experimental data from combined photoelasticity and strain gage information taken from a CR-39 specimen under a high loading rate. He also obtained experimental data on the manner in which the elastic modulus changed under high loading rates. The dynamic modulus appeared to have increased in the same manner as that of the stress optic coefficient.

In the current study, actual stress values were never calculated from the fringe data obtained from the explosive loading sequence in which CR-39 was utilized as a model material. However, it was desirable to perform dynamic and static material coefficient calibration tests on a CR-39 model (Figures 31, 32) in order to verify the procedure outlined by Clark before extending the method to Plexiglas. Also, since comparisons were made throughout this study to published results of other investigators who used CR-39, it was beneficial to have verification that the CR-39 material purchased for this study was the same as that used by the previous investigators.

There is some controversy over whether Poisson's ratio changes under dynamic conditions. Sutton found that dynamic Poisson's ratio is the same as that for the static case, within experimental error (134). However, Dally and Lewis have shown that the dynamic value of Poisson's ratio can

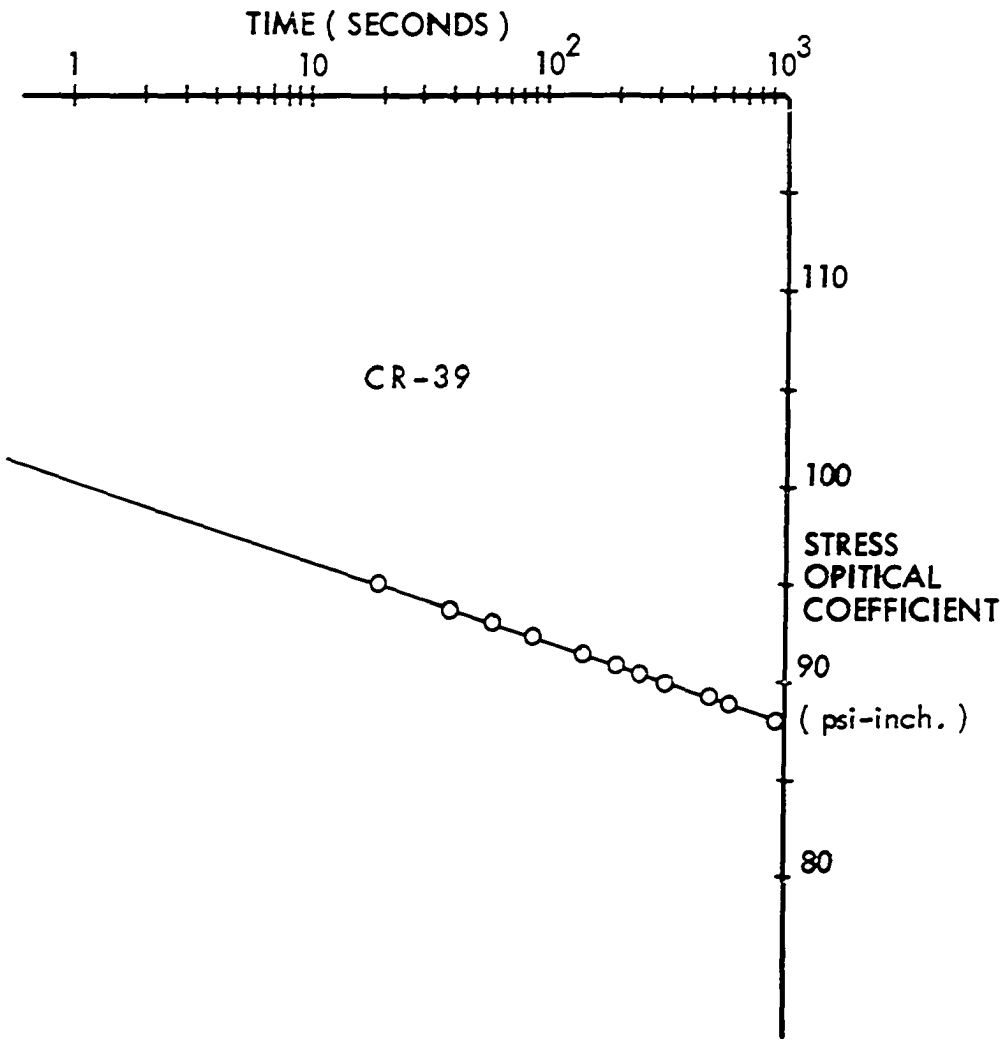

Figure 31. Optical creep calibration of CR-39

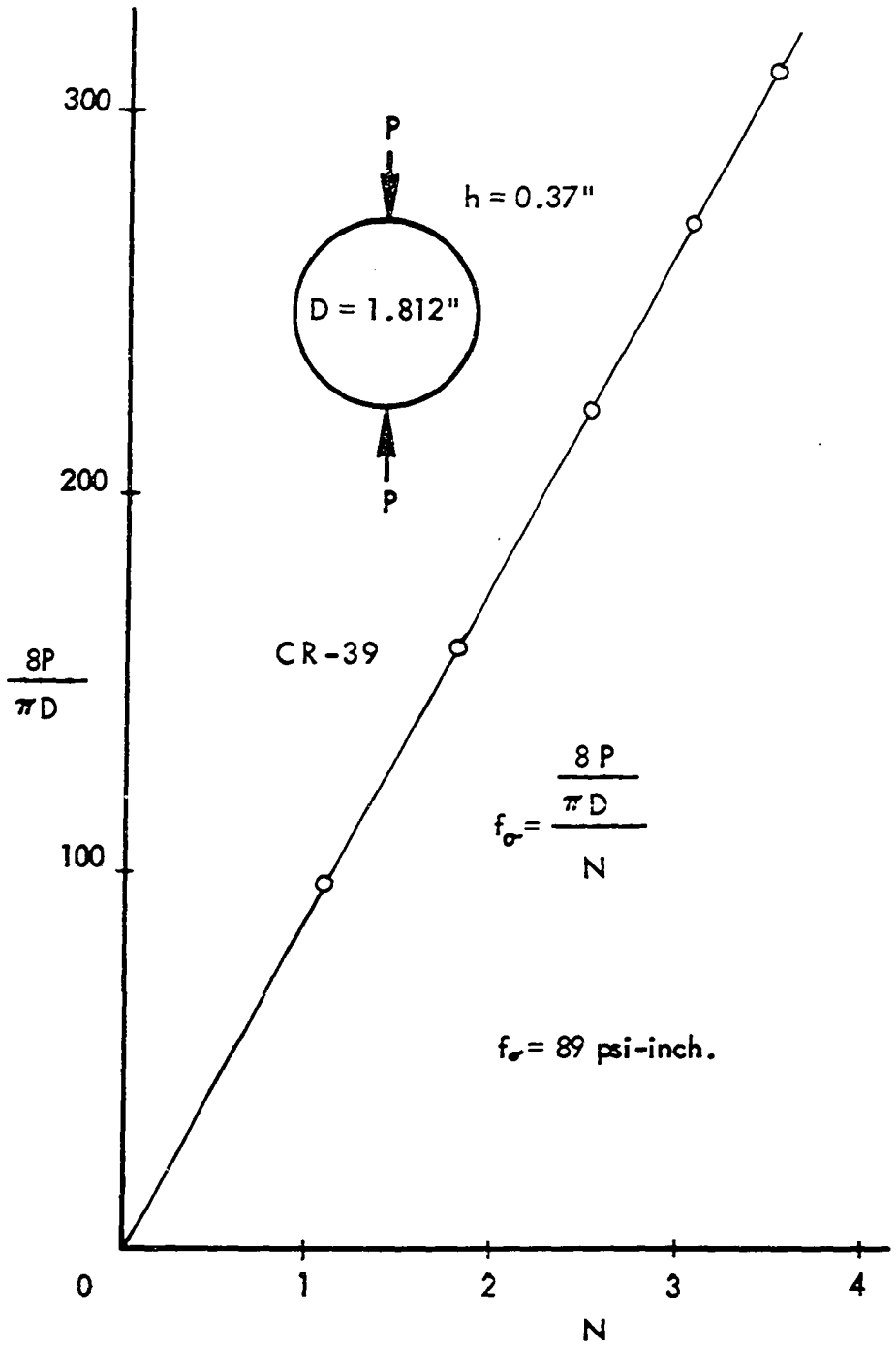

Figure 32. Static calibration of CR-39

be up to 30 per cent lower than the static value for certain loading rates (58, p. 541).

The significant mechanical and optical properties of CR-39 are listed below:

static elastic modulus	$(E)_s$	312,000 psi
dynamic elastic modulus	$(E)_d$	520,000 psi
static Poisson's ratio	$(\nu)_s$	0.43
dynamic Poisson's ratio	$(\nu)_d$	0.329
density	ρ	.047 lb./in.^{3}
static tensile strength	σ_u	6,500 psi
static proportional limit	σ_{pl}	3,600 psi
static stress fringe value	$(f_\sigma)_s$	89 psi-in.
dynamic stress fringe value	$(f_\sigma)_d$	122 psi-in.

Polymethymethacrylate

Polymethymethacrylate, Plexiglas, is a commercially available, colorless, transparent plastic with excellent optical properties. Since Plexiglas is usually cast between heat-resistant glass plates, a highly smooth optical surface is formed.

Plexiglas was chosen for close field studies because of the similarity of its mechanical properties to that of CR-39 as well as its insensitive optical response which was necessary in the high stress region near the explosion.

Using the technique established by Clark for CR-39, calibration tests, to establish the stress fringe coefficient

and optical creep characteristics, were conducted on Plexiglas specimens (Figures 33 and 34). The variation of elastic modulus with time was determined from strain gage measurements under constant load and checked with short time dynamic elastic modulus data obtained from wave velocity measurements. The manner in which the effective elastic modulus and the material fringe coefficient varied with time proved to follow the same trend that Clark observed for CR-39.

The significant mechanical and optical properties that were determined for Plexiglas are listed below:

static elastic modulus	(E)	326,000 psi
dynamic elastic modulus	$(E)_d$	800,000 psi
static Poisson's ratio	$(\nu)_s$	0.40
dynamic Poisson's ratio	$(\nu)_d$	0.40
density	ρ	.0426 lb./in.^{3}
static tensile strength	σ_u	11,700 psi
static proportional limit	σ_{pl}	5,400 psi
static stress fringe value	$(f_\sigma)_s$	740 psi-in.
dynamic stress fringe value	$(f_\sigma)_d$	1400 psi-in.

Model Preparation

Plates

The Plexiglas plates were fabricated from 12 inch by 9 inch by 0.235 inch plates. A hole for the liner and the

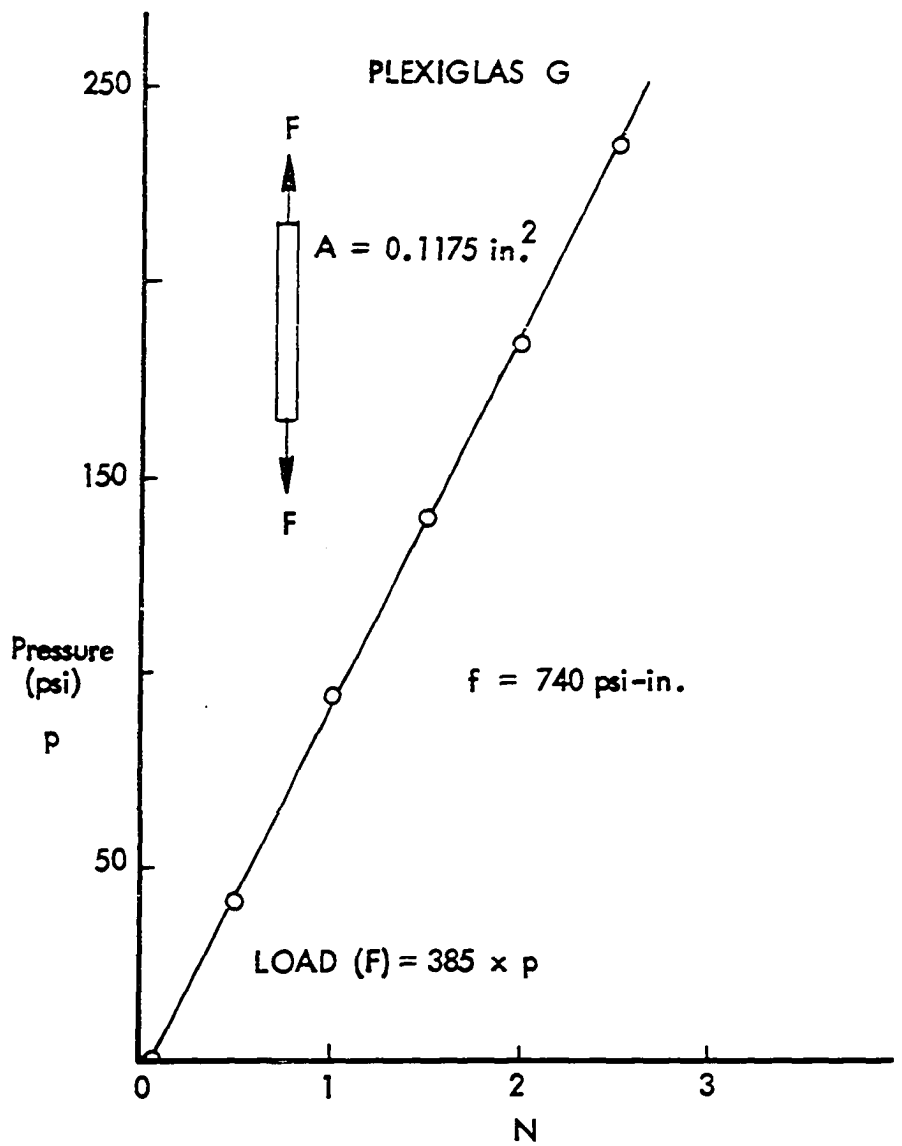

Figure 33. Static calibration of Plexiglas

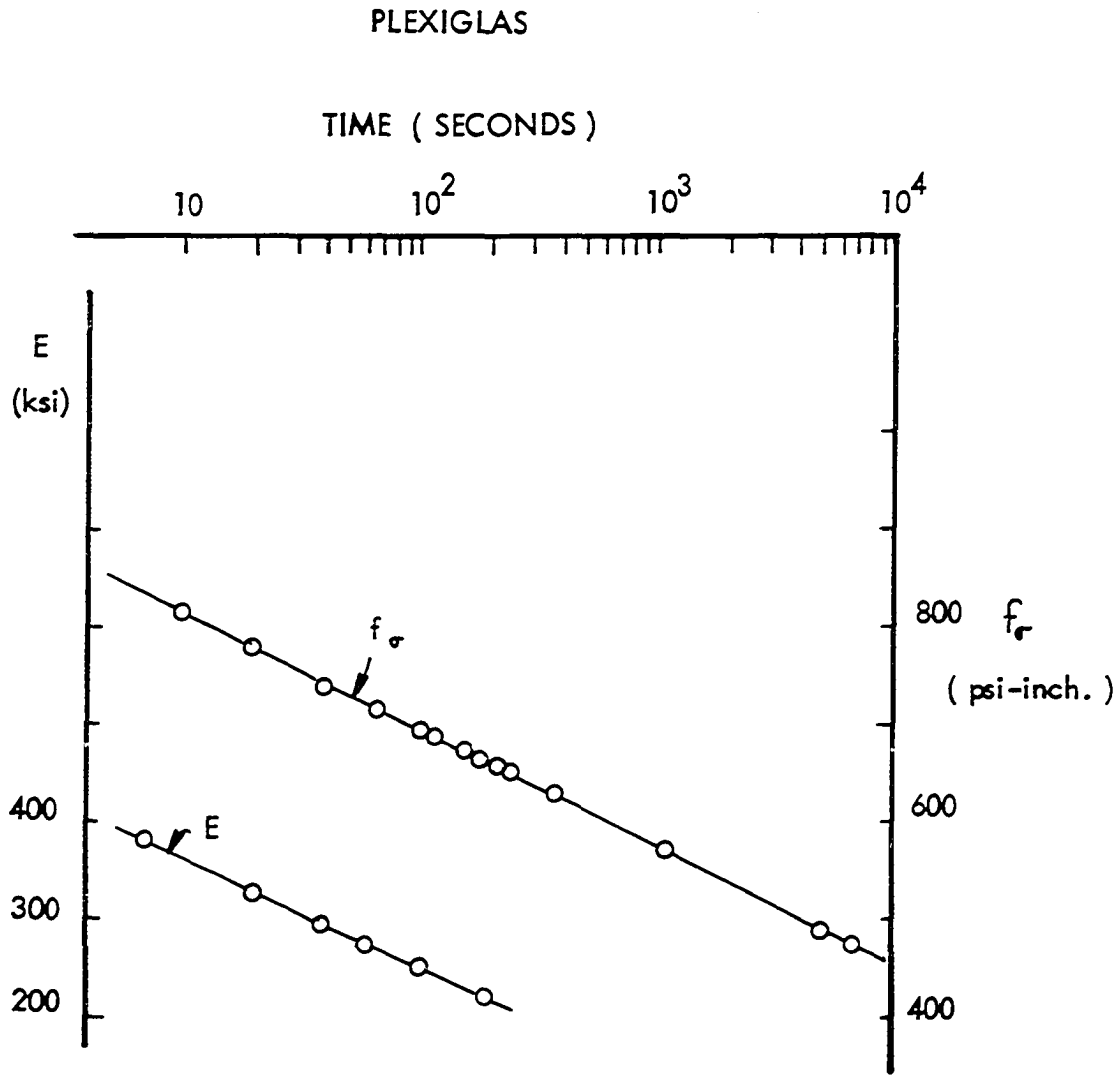

Figure 34. Optical creep calibration of Plexiglas

explosive charge was located 4 inches from the top and along the longitudinal center line of the model. Since production of a smooth 0.5 inch diameter hole free from residual stresses, scratches, or nicks, presented considerable difficulties, some detail was spent on its fabrication in the following paragraphs.

The following procedures were tried and eliminated because of the various reasons stated below.

Routing An aluminum template was used with various high speed routing bits in several attempts to produce the desired 0.5 inch hole. Although routing produced a relatively smooth hole, small chips were found on the sharp edges of the hole. These would have produced unwanted stress concentration when subjected to explosive loading. Care also had to be taken not to allow the material to become too hot while routing. This would have produced optically apparent high residual stresses around the hole. Although routing is a highly satisfactory and proven method for shaping photoelastic specimens with larger holes and straight edges, the procedure was eventually abandoned for producing the 0.5 inch hole.

Reaming Several reamers were tested for producing the finished hole. A new high speed 7/16 inch drill was used to introduce a pilot hole. Two pieces of plastic were bonded with double adhesive tape to both sides of the model before drilling. This eliminated a large amount of the

chipping on the edges of the hole. A light oil was constantly fed into the hole during drilling in order to cool the bit. Once the drilling was completed, a 0.5 inch spiral fluted reamer was slowly fed through the material. This proved to be undesirable since it had a tendency to pull its way through the model producing chipping and cylindrical scratches in the hole where shavings would lodge between the cutting edge and the hole wall. A straight fluted reamer eliminated the chipping, however, cylindrical scratches remained on the hole walls. Many variations of drill and reamer rotation speeds as well as feeding rates were investigated but satisfactory results were never achieved.

Lapping Several adjustable lapping tools were used in an attempt to remove the cylindrical scratches produced in the reaming sequence. A carefully honed lapping tool, which would produce a mirror finish on most metals, proved to be too harsh for soft plastics. Hand made Teflon lapping tools did not produce additional scratching but merely smoothed the existing ones into polished grooves which were still undesirable.

Boring Boring proved to be a highly successful method of producing the desired surface finish on the hole. A 0.375 inch hole was first drilled in the desired location using the technique established for initial drilling in the

reaming procedure. The model was then clamped in a vertical boring machine. A 0.25 inch single edge boring bit was used to continue to bore the hole to the 0.5 inch diameter. Ten cuts of 0.01 inch and four at 0.005 inch together with a small amount of polishing produced a stress free hole with the desired finish. The polishing was achieved with a piece of soft gauze wrapped around a 3/8 inch wooden dowel and rotated at 300 rpm in a drill press. The gauze was saturated with an antistatic polishing solution for removing scratches on Plexiglas. The result was a highly polished, scratchless, chipless, mirror smooth, stress free 0.5 inch diameter hole.

Liners

The major difficulty encountered in trying to produce a uniform, reproducible pulse from an explosive charge is the highly destructive nature of the loading mechanism. When lead azide, PbN_6, is detonated in an unprotected cavity in a glassy birefringent material, the pulse is distorted because of the melting and fracturing of the material subjected to the extremely high pressures and temperatures of the explosive. To shield the harsh explosive from the birefringent materials, a liner was sought that would: a) provide smoothing energy absorption b) serve as a means of diverting dense gases and smoke away from the area to be observed optically, and c) provide sufficient

protection for the model from the explosive so that fracture does not occur in the birefringent material. Several liners were investigated and eliminated for various reasons.

Bakelite, nylon, pheonlic, red fiber, and acrylic liners became extremely brittle under the high loading rates thus producing cracking which was transmitted into the model.

Although the steel, aluminum, and brass liners eliminated the cracking, the transmitted pulse did not exhibit radial symmetry. The explosive also produced a permanent set in the metal which resulted in a residual loading of the model. Aluminum was the most desirable of the metallics.

Polytetrafluoroethylene (Teflon) was found to exhibit most of the qualities desired for a liner. Ease in machineability was an added advantage of the material.

The liners were fabricated from 1.5 inch segments of 0.5 inch diameter rods. The rods were centered and drilled in a lathe with a 3/16 inch diameter high speed bit. Once the hole in the model had been machined, honed, and polished to the desired condition, the outside diameter of the Teflon rod was then carefully turned in a lathe until it would press fit into the hole. The liner was then counterbored (7/16 inch diameter) from both ends until the thickness was that of the model. The thin shell left from the counter bore was shaved slightly to allow the smoke to be directed

up and away from the side of the hole that was to be photographically recorded.

Explosives

Of several explosives considered, elimination of all but two was accomplished by a brief literature survey of the stability, access, and performance of these explosives. The two tested were pentaerythritol tetranitrate (PETN) and lead azide (PbN_6).

PETN Pentaerythritol tetranitrate which is readily available in the form of Primacord, has a highly desirable detonation velocity of 201,800 in./sec. (135, p. 45) and density of .036 lb./in.^{3}. In tests conducted by Daniels (62), 50 mg. of PETN was found to provide model loads that produced sufficient birefringent response without producing unnecessary fracturing.

The main disadvantage of PETN is the fact that it is a secondary explosive which takes a high level of energy for detonation (136, p.12). This level was impossible to achieve with the heating wire, while the exploding wire detonators caused some misfires. Daniels found that EBW headers, which are commercially available detonators, produced no misfires.

The EBW headers are constructed of two terminal pins embedded longitudinally in a cylinder of electrical insulation material. The terminals are flush at one end where

a 0.0015 inch diameter gold wire is soldered to the terminal pins which are 1/16 inch apart. The other ends of the terminals are connected to lead wires. When subjected to a 2000 volt detonation circuit, the exploding gold wire will produce sufficient energy to ignite the PETN. However, the main drawback to the EBW headers is their extreme cost compared to that of the detonators constructed by the author.

Although the 30,000 volt arcing wire produced sufficient energy to detonate the explosive, it was desirable to be able to use the same explosive for all detonation systems.

PbN_6 Lead azide is the more accessible explosive of the two since it can easily be precipitated in distilled water from a mixture of two readily available compounds. If left in the water as a precipitate, it can be stored safely for an indefinite period of time. When needed, it can then be poured through a fine filter paper and washed with acetone. The mixture will dry within a few minutes to a powdery primary explosive. Since it is a primary explosive, it can be made to ignite under any of the detonation systems previously discussed. This, of course, means it is also more dangerous to use than PETN. If common sense and reasonable caution is consistently practiced, it is not as dangerous as many household cleaning fluids. Since lead azide will ignite under pressure in a powdered state, it was kept in a polyethylene box when being used to load a

model. Cellophane and basal wood spatulas were all that was ever placed in contact with the PbN_6 while loading a model. A face shield and leather gloves were also used at all times when working with the lead azide. In exploding over 15,000 mg. of PbN_6, no unexpected explosion was ever encountered by the author.

Lead azide has a burn rate of 200,000 in./sec. at density of 0.044 lb./in.^{3} (135, p. 45), which is slightly less than the PETN. The charges used in this investigation compacted neatly into the 3/16 inch cavity of the liner with a density of 0.048 lb./in.^{3}.

Auxiliary Equipment

During the course of the study, several auxiliary assemblies and techniques were developed to determine information not readily available by any other means.

Material wave velocity determination

In the beginning of the twentieth century, B. Hopkinson (137) measured the maximum longitudinal displacement associated with a tensile elastic wave in a steel wire by placing an insulated metallic probe close to the surface of the wire. As the stress wave passed, the movement of the surface resulted in electric contact being made between the wire specimen and the probe. Since that time, many ingenious means have been employed to electron-

ically or optically sense the arrival and departure of stress waves and thus determine their speed in a particular material. Three methods were used in this investigation to determine the average rate at which a stress wave moves through a medium. These utilized resistance strain gages, photoelasticity, and quartz load cells as tools for determining the wave speeds.

Resistance strain gages The resistance strain gages were particularly suitable for this investigation since they could be bonded easily to the birefringent plate materials with epoxy or Eastman 910 pressure sensitive adhesive.

A 0.25 inch by 0.25 inch by 8 inch bar was constructed of each material to be tested. For a particular specimen, a 120Ω foil strain gage was bonded in a longitudinal direction at a distance of 4 inches from each end of the bar. A 0.25 inch by 0.25 inch by 0.20 inch aluminum cap was then bonded to one end of the bar with double adhesive tape. A small indenture in the cap accepted the tip of a cupro-nickel detonator embedded in a charge of PbN_6 which was held in place by cellophane tape. The bar was suspended by two threads as shown in Figure 35. The detonation wire was connected to the 2 KV output of the detonation circuit (Figure 19). The 20 volt output was connected to the trigger input of a 564 Tektronix Storage Oscilloscope. The

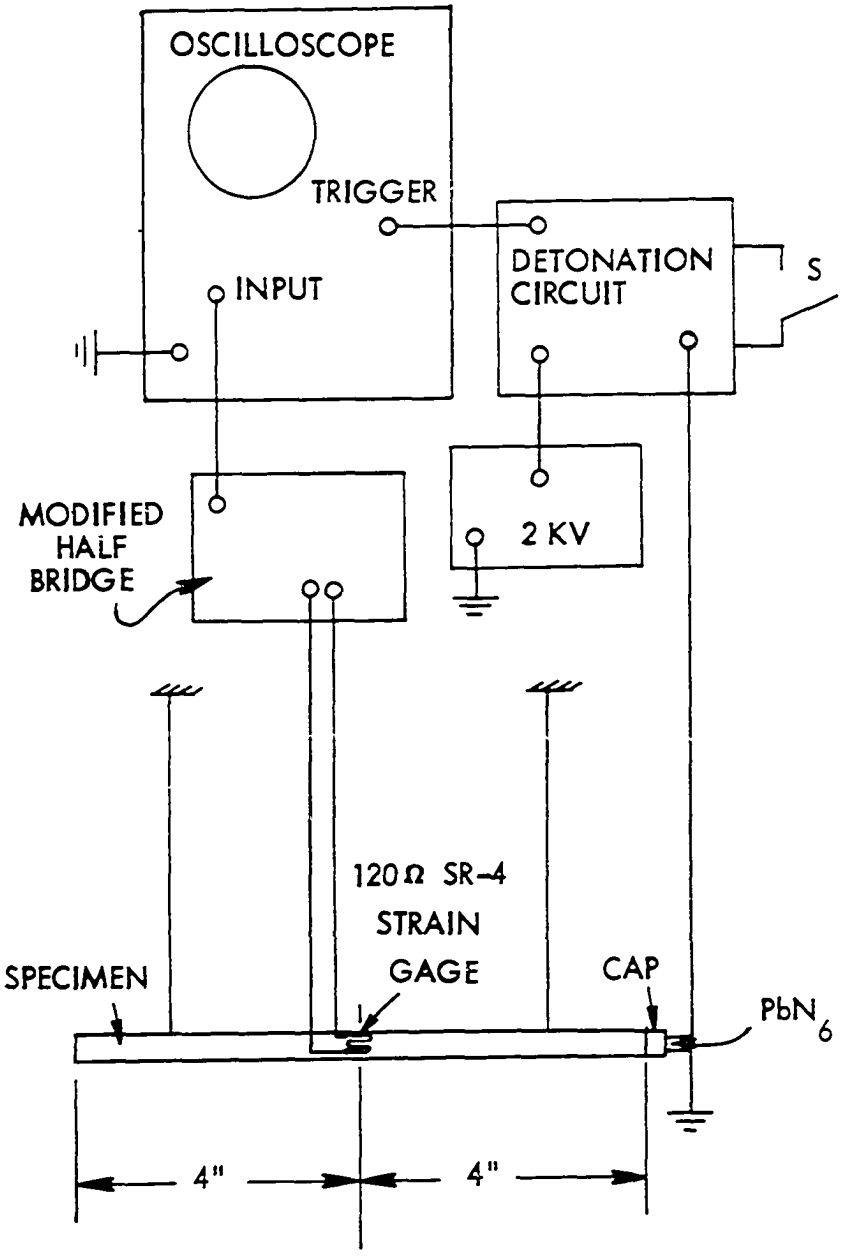

Figure 35. Instrument arrangement used to determine material wave speeds with an SR-4 strain gage

strain gage formed one arm of a modified half bridge circuit (Figure 36), which is commonly used for measuring dynamic strains. The 1 MFD capacitor was included in the circuit to serve as a low frequency filter. The system was calibrated such that a high frequency 1000 microinch/inch strain would produce a 7.5 MV signal which was fed to the vertical input of the storage oscilloscope. Once the detonation circuit switch was closed, the exploding charge of PbN_6 sent a compressive pulse down the bar. Simultaneously, the scope would start to sweep. As the compressive pulse moved past the strain gage, a voltage deflection was recorded and stored on the vertical trace of the oscilloscope. The average wave speed was then calculated from the known time and distance of travel of the pulse. Initially, two gages were spaced six inches apart along a 10 inch rod. Each gage recorded the pulse on the oscilloscope as it passed. From the arrival time of the pulse at each gage location together with the known distance of travel, an average plane wave velocity was calculated for the material. Although the method worked well, the information gained was the same as that from a single gage. Therefore, the additional gage was abandoned.

The advantage of the strain gage is that it is simple, sturdy and light. By using a suitable combination of these gages on the surface of the specimen, it is possible

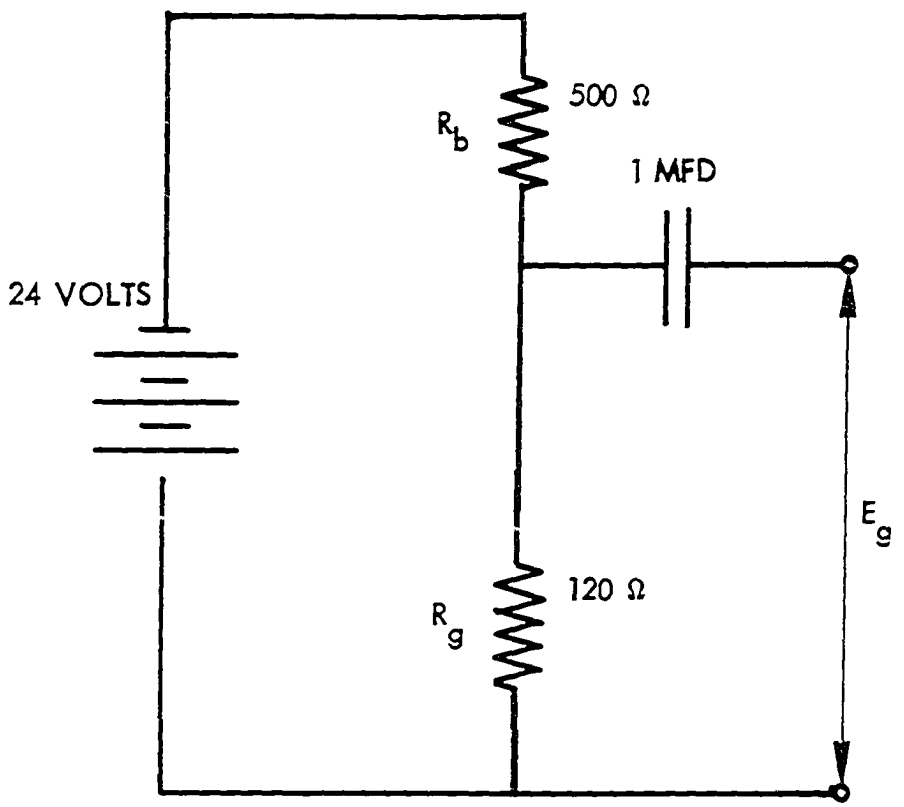

Figure 36. Modified half bridge dynamic strain gage circuit

to arrange for only one type of motion to be detected. The disadvantage of the gage is that it is of finite size which results in an integrated value of the strain over a region of the specimen. Another disadvantage is that a high modulus gage being bonded to a lower modulus specimen provides some local reinforcement which could conceivably interfere with the phenomenon being observed. Since the gage was used only to sense a time of arrival and not actually to measure the magnitude of a particular pulse, the disadvantages were minimal.

Photoelasticity The multiple spark camera provides a visual representation of the wave movement during a known time interval. This method is particularly advantageous since no detecting device is in contact with the surface of the model during testing. Of course, it is limited to transparent birefringent materials. Since approximately 99 per cent of the light output of the multiple spark gaps is lost during transmission through the optical elements (polaroids, wave plates, etc.), most epoxies of light amber color are too translucent to investigate by this method.

The photoelastic method was used primarily on large plates as opposed to rods. The plate velocity could then be easily converted to that of the rod if so desired. One quarter to one inch reference lines were drawn or scratched on a particular birefringent plate. Once the PbN_6 charge was

detonated, the progression of the wave was easily measured by using the lite mike outputs and fringe positions from the reference lines. This method has the advantage of being able to measure the velocity of any of the waves observed in a plate for a particular loading situation.

Quartz load cell When the time came for the Teflon to be examined, a different method for determining wave velocities had to be devised. Since Teflon is made to resist adhesives, resistance strain gages could not be bonded to the Teflon specimens. Photoelastic analysis was excluded as well since Teflon is opaque. A testing procedure was then employed which utilized a quartz force transducer (load cell) as a sensor. This method proved very satisfactory for Teflon as well as providing some advantages over the previously discussed procedures for other materials.

The bar or rod of the specimen tested was supported by three small V-blocks on a set of tracks used to align the specimen with a 50 lb. steel mass (Figures 37 and 38). The mass was tapped to accept the 10-32 threads of a beryllium copper mounting stud of a Model 912 Kistler load cell. A small brass plate was attached to the opposite end of the load cell. The specimen was mounted to the brass plate with a thin coat of silicon grease. The grease held the rod in position and allowed a small amount of tension to develop in the rod when loaded. A 0.25 inch thick

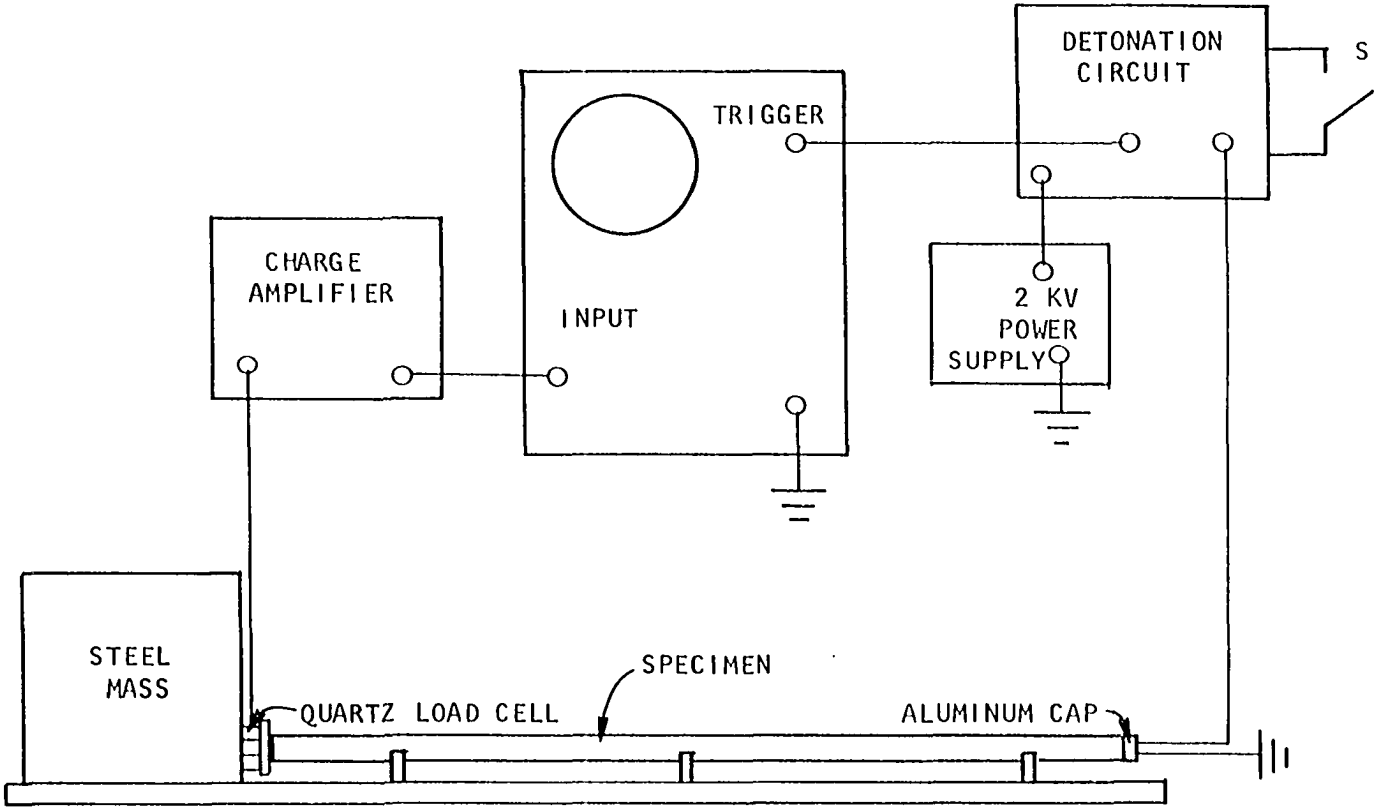

Figure 37. The quartz load cell circuit for determining material wave velocities

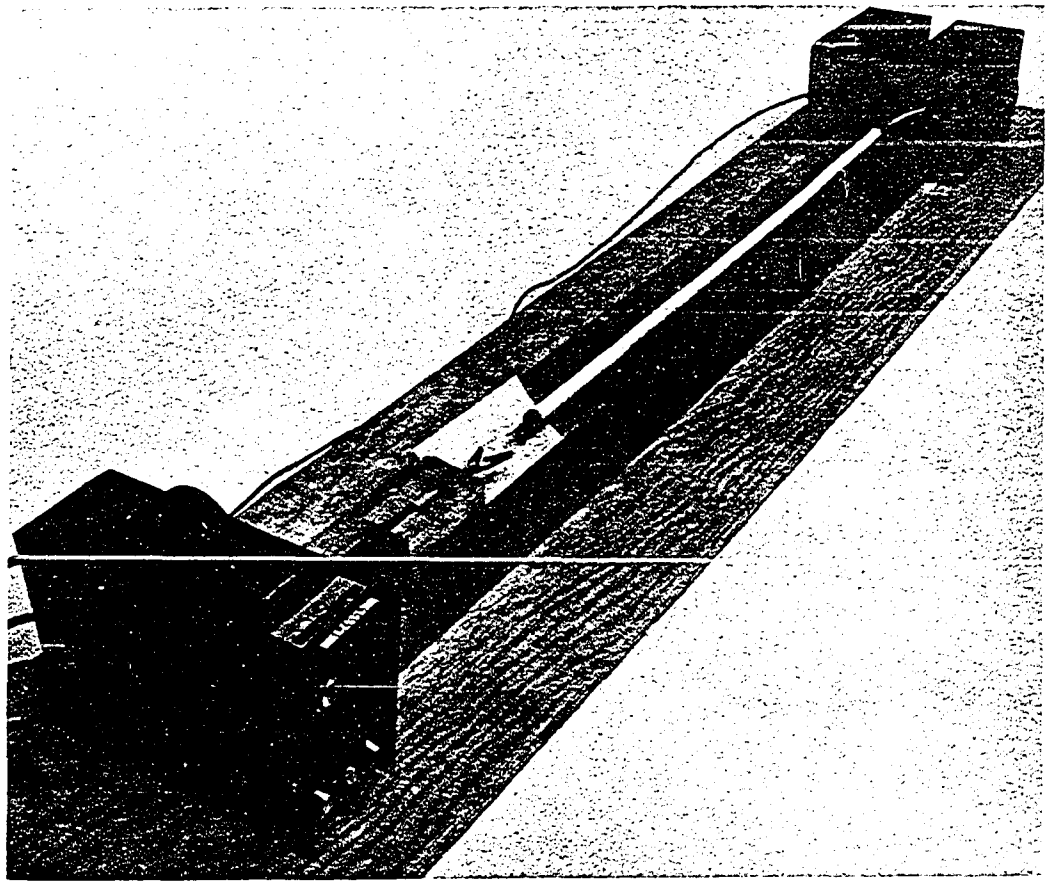

Figure 38. The quartz-load cell arrangement for determining wave velocities

aluminum cap, sized to fit the end of the specimen, was taped to the opposite end of the rod. A small cavity on the end of the cap held the required amount of PbN_6 explosive which was detonated with a cupro-nickel detonator embedded in the charge. Since 0.50 inch diameter Teflon rods of 36 inch lengths were easily obtained from suppliers, these were used for testing and as stock for liners.

When switch S in Figure 19 was closed, the PbN_6 was detonated at the same instant that the oscilloscope was triggered. A compressive plane wave traveled to the end of the rod where it impinged upon the brass plate connected to the load cell. A portion of the pulse was reflected as a compressional wave which traveled back down the length of the rod. It was then reflected from the free end of the rod as an extensional wave which again traveled the length of the rod where it registered as a tensile pulse on the force transducer. The electrostatic charge output of the transducer was converted to a standard voltage signal by means of a Kistler Model 504 solid state charge amplifier. The signal was then recorded on the vertical input of the Model 547 Oscilloscope. The signal was calibrated such that a 200 lb. force on the transducer would produce a one volt output signal from the amplifier.

A sequence of twelve different tests were conducted for an 18 inch long Teflon rod in order to obtain the average time of travel of the pulse. The test results proved to be

highly repetitive in that no recordable difference was observed in the arrival times of the compressive and the tensile pulses for the sequence. The oscilloscope traces shown in Figures 39 and 40 present a typical example of two separate tests on the same rod. Although there was a marked difference in the pulse magnitudes between the two tests, since the size of the PbN_6 charge was increased from 10 mg. in Figure 39 to 25 mg. in Figure 40, the wave speed was the same in both cases. Figure 41 illustrates the effect of varying the charge in step increments from 10 mg. to 60 mg.

In order to detect the very low voltage output of the transducer associated with the arrival of the compressive wave, the voltage sensitivity on the oscilloscope was increased to 0.01 volt per cm. This produced a sharp, distinct rise in the voltage trace. Since this method would be in error if the inherent delay in the electronic system significantly increased the observed arrival time of the pressure wave, tests were made on several different lengths of rod cut from a single specimen. By plotting the initial arrival time of the pressure wave for each of the different rod lengths, the inherent delay in the circuitry was found to be negligible as illustrated in Figure 42.

The advantages of this method are numerous. The experimental apparatus arrangement is easy to set up, simple

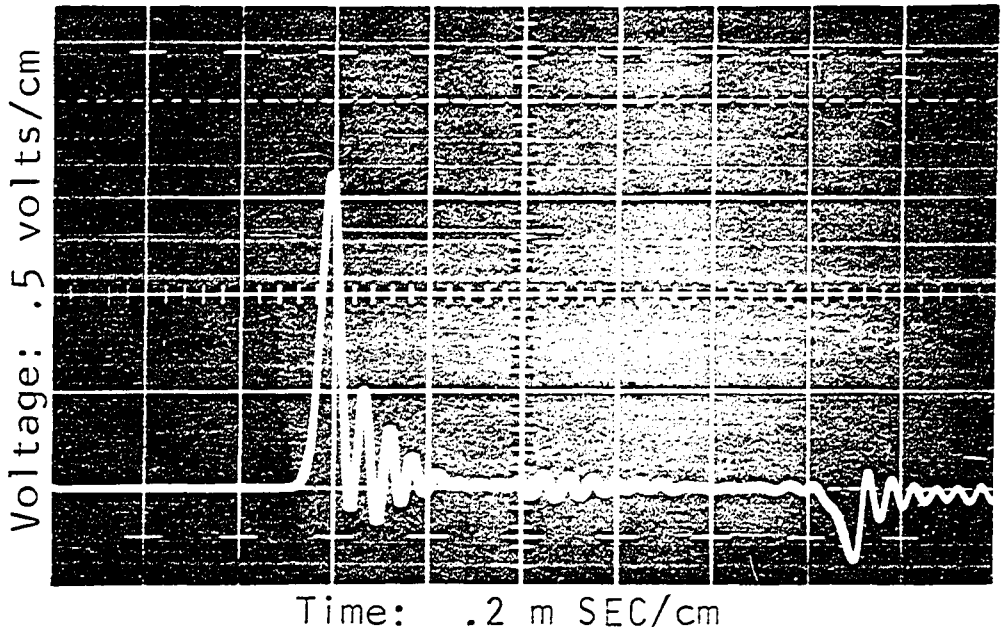

Figure 39. Oscilloscope trace of compressional and extensional plane wave moving in a Teflon rod (10 mg)

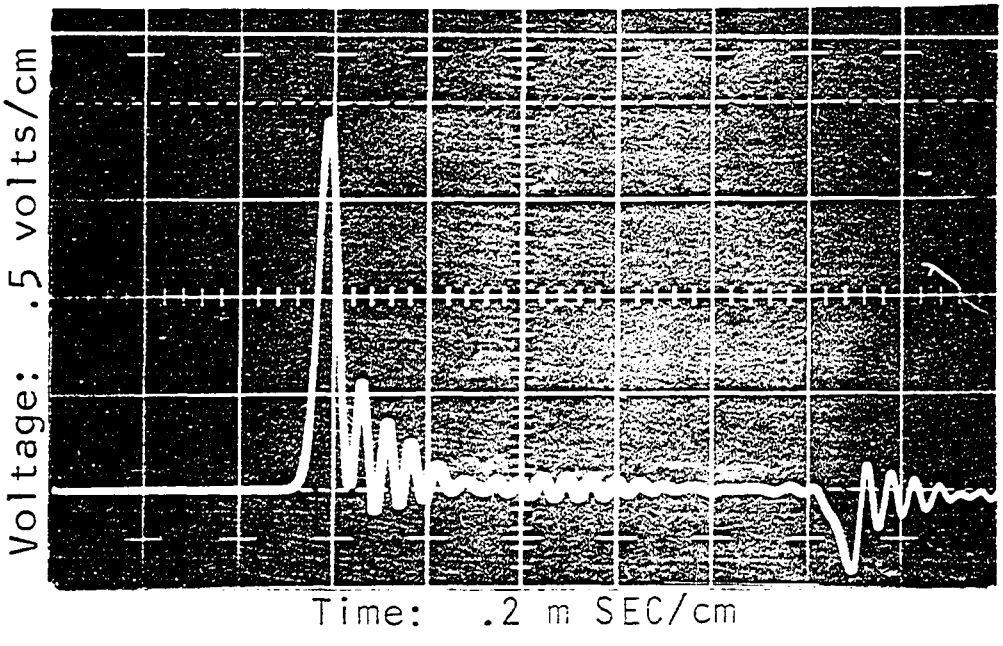

Figure 40. Oscilloscope trace of compressional and extensional plane wave moving in a Teflon rod (25 mg)

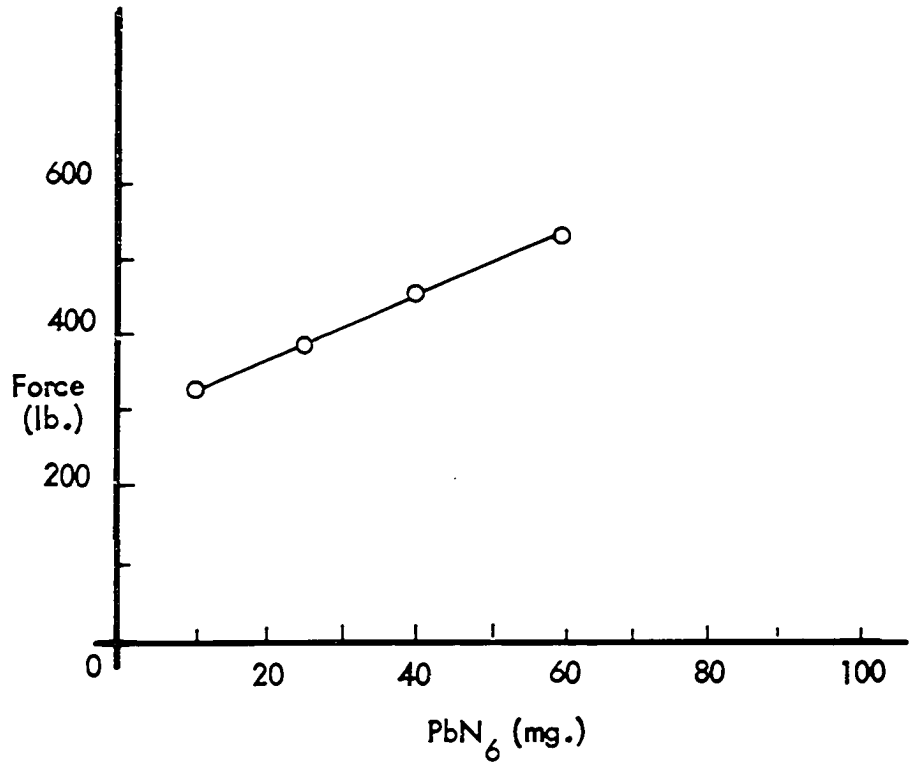

Figure 41. Compressive load cell force as a function of PbN_6 quantity for an 18 inch Teflon rod

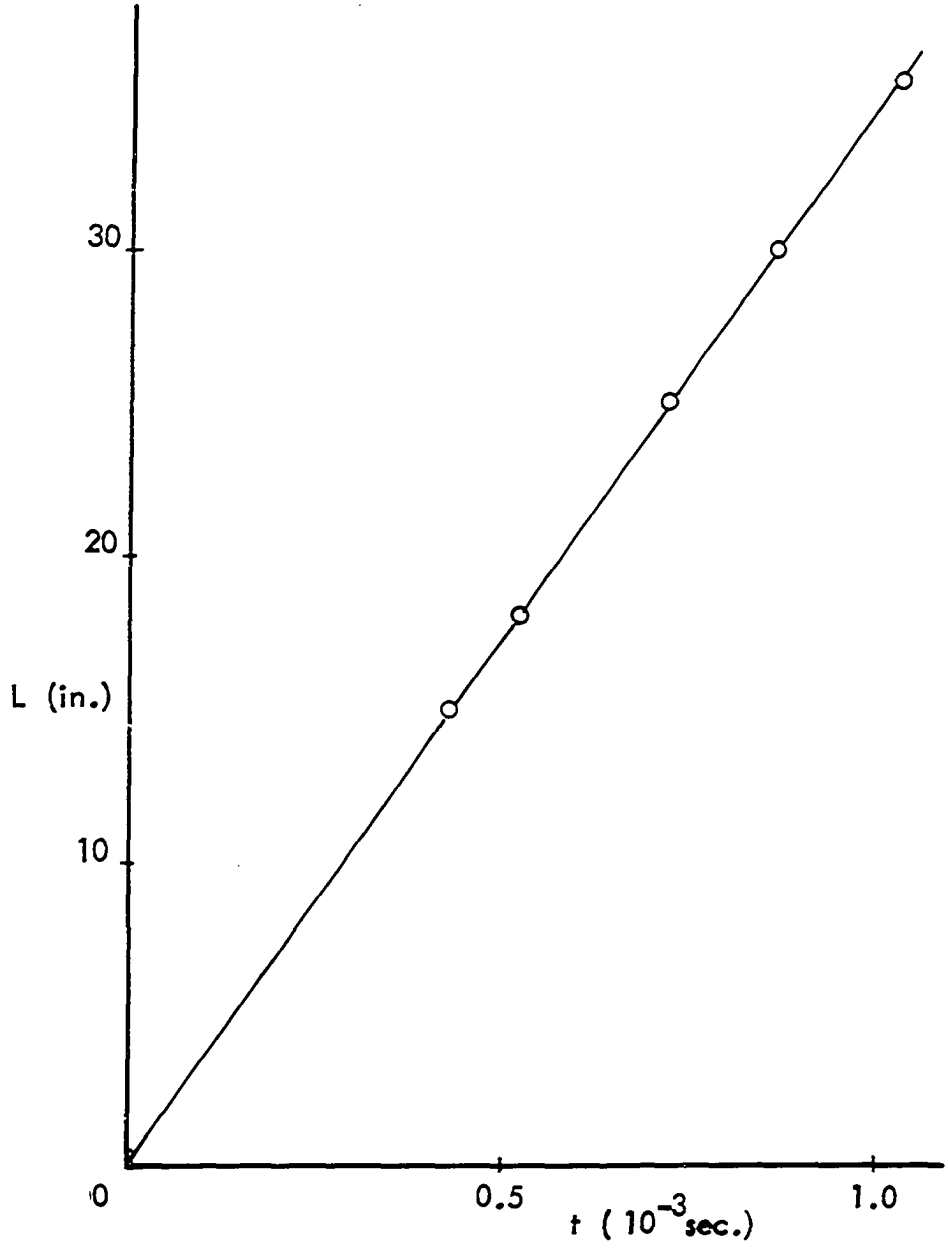

Figure 42. Several different Teflon rod lengths as a function of wave travel time

to use, and provides data that can be analyzed quickly. The system does not use any sensors bonded to the surface of the specimen where they could conceivably alter the wave phenomenon. The test procedure is completely nondestructive.

Kolsky (138) suggested a similar method which employed a heating wire detonation, a photocell relay for triggering, and a condensor detector for the pulse sensor. Although very good results could be expected from Kolsky's method, the sensitive adjustments of the condensor gap and the careful electrical shielding that was essential to suppress the electromagnetic pulse emitted by the explosive charge made this system appear somewhat less convenient.

Photographic techniques

Except for the quality of the lens system, the selection of the film is the major contributor to the quality of results obtained in a photoelastic photograph. Two films were used throughout this investigation. The reason for their selection is expanded upon below.

Black and white Relatively high contrast black and white film is used in photoelasticity since these films produce the sharpest fringes. Kodak Professional Copy Film 6125 (formerly Gravure Copy Film) was found to be a suitable film for the multiple spark camera. Although Gravure is a relatively slow speed film with a white flame arc ASA speed of 25, it proved highly sensitive in the blue

light of the spark camera. Since the film is orthochromatic, it has relatively fine grain and is insensitive to red. This attribute allows for handling of the undeveloped negative in a red safelight, which is a significant advantage when working with large sheet films.

In black and white photography, the density of the recorded image on a negative is a function of the exposure of the film. The exposure is the total amount of light of a given intensity that reaches the film in a given length of time. Since the spark camera had a fixed intensity of light of a fixed duration of 0.5 microseconds, any adjustment in the image density had to be accomplished with the film and chemicals and not mechanically with the camera. Since the spark camera produces a point light source, any adjustment of the diaphragms in the lens array would only accomplish a change in the diameter of the light field and not its intensity.

Hurter and Driffield established a density-exposure relationship that indicated a photographic film had to overcome a certain amount of inertia exposure before the film would record small variations in density (in 7, p. 183) Any exposure before this inertia was overcome resulted only in a light, uniform fogging of the negative. One means used in this investigation to increase the sensitivity of the film was to overcome this inertia by prefogging prior to loading the film in the spark camera back.

Kodak Developer D-11, a high contrast developer that produces good resolution with low graininess, was chosen for developing the Gravure film. The developer was used in a one to one solution at the recommended developing temperature of 68° F. However, a developing time of eight minutes as opposed to the recommended four minutes produced the desired density of the image. Doubling the developing time of the film is another means of increasing the sensitivity of the film (approximately doubles the ASA speed) at the expense of producing a grainier image. The grain becomes a problem in extreme enlargements, but produced no noticeable effect on the small five to one enlargements used for analysis. The chemical "pushing" of the film seemed to produce superior results to prefogging.

Color Color photographs of isochromatic patterns have long been of value in static photoelastic analysis. For a given stress situation, the position of the fringes is dependent on the wave length of the light used. If a white light source is used, then the fringe value is obtained by determining the maximum shear stress necessary to produce a change from one color order to the next. Since this relies on the subjective color vision of the investigator, as well as the correct color rendition of the photographic system, the personal element inevitably induces errors. Since very accurate fringe definition is easily obtainable with monochromatic light, colored

photographic records of isochromatics are reserved for situations where other than quantitative results are desired from photoelasticity. Such a situation occurred in this investigation. In observing the fringes propagating out from an explosive cavity, the order is not readily distinguishable. Once the pressure wave propagates several inches into the material, the separation of the higher order fringes usually makes the peak location apparent. However, because of the low sensitivity of Plexiglas, the fringes are extinguished by geometric attenuation before they have propagated to this extent.

In a region where information is obtained from a small number of monochromatic fringes, white light will yield the increasing or decreasing order of the isochromatics by a comparison of their color order in the spectrum. The point or region where the difference in principal stress is zero also appears as a black isochromatic in a circular polarized dark field polariscope subjected to white light.

By removing the filter plate from the lens array, the frequency range of the spark spectrum is broadened, thus producing some gradiation in color among the isochromatics. Most important, however, is the fact that the isotropic band appears to be darker than any other isochromatic thus locating the point at which the compressive pulse is complete.

With the exception of some mention of color experimentation by Christie (20) in 1955, no information was available on recording photoelastic stress waves with colored film. Christie experimented with an Ektachrome film where he varied the color balance with a liquid filter. Since his interest appeared to be one of curiosity, no technical data was supplied in his paper concerning the exact film or filter spectrum with which he experimented.

In comparing the various colored sheet films available, Kodak Ektacolor Professional Film 6101, Type S was chosen because of its excellent quality in color reproduction for exposure times less than 1/10 second. Type S film has a daylight ASA speed of 100. Since the spark camera does not produce white light, various calibration tests were performed to establish meaningful results. A 2.0 inch diameter CR-39 disk was loaded in a small portable loading frame. A photograph of the loaded disk in a white light (dark field) polariscope was taken at a speed of 1/60 second to check the quality of the color reproduction of the film. By observing the isochromatics in the disk and then adjusting the filter density in the enlarger, the correct color rendition was achieved. The disk was then placed in the polarized dark field of the spark camera. A single shot was taken at 0.5 microsecond with several of the lenses in the array each having a different filter attached. The results of the various

filters were compared for the best color rendition. The best results were achieved with a lens that had no filter. The film was pushed in development to the extent that the density was sufficient to distinguish the isochromatics. The filter density in the enlarger was varied until the color rendition best represented that of the known stress situation. Since black is an easy base-color to work with in colored photographic enlarging, the zero order isochromatic was used as the reference. When the enlarger filter combination produced a very dense, black fringe, the remaining isochromatics were in good agreement with their expected color.

When an actual test was conducted on a dynamic isochromatic pattern, the color distinction was somewhat inferior to that produced from a static shot. This was attributed to the slight overlapping and mixing of the many close knit moving isochromatics. The variable nature of the light output was also believed to be a contributor. However, the primary motive for using colored film was in locating the points of zero fringe order, which are easily distinguishable in the two frame sequence of the 2 $\frac{1}{4}$ inch wide strip recorded in Figure 43.

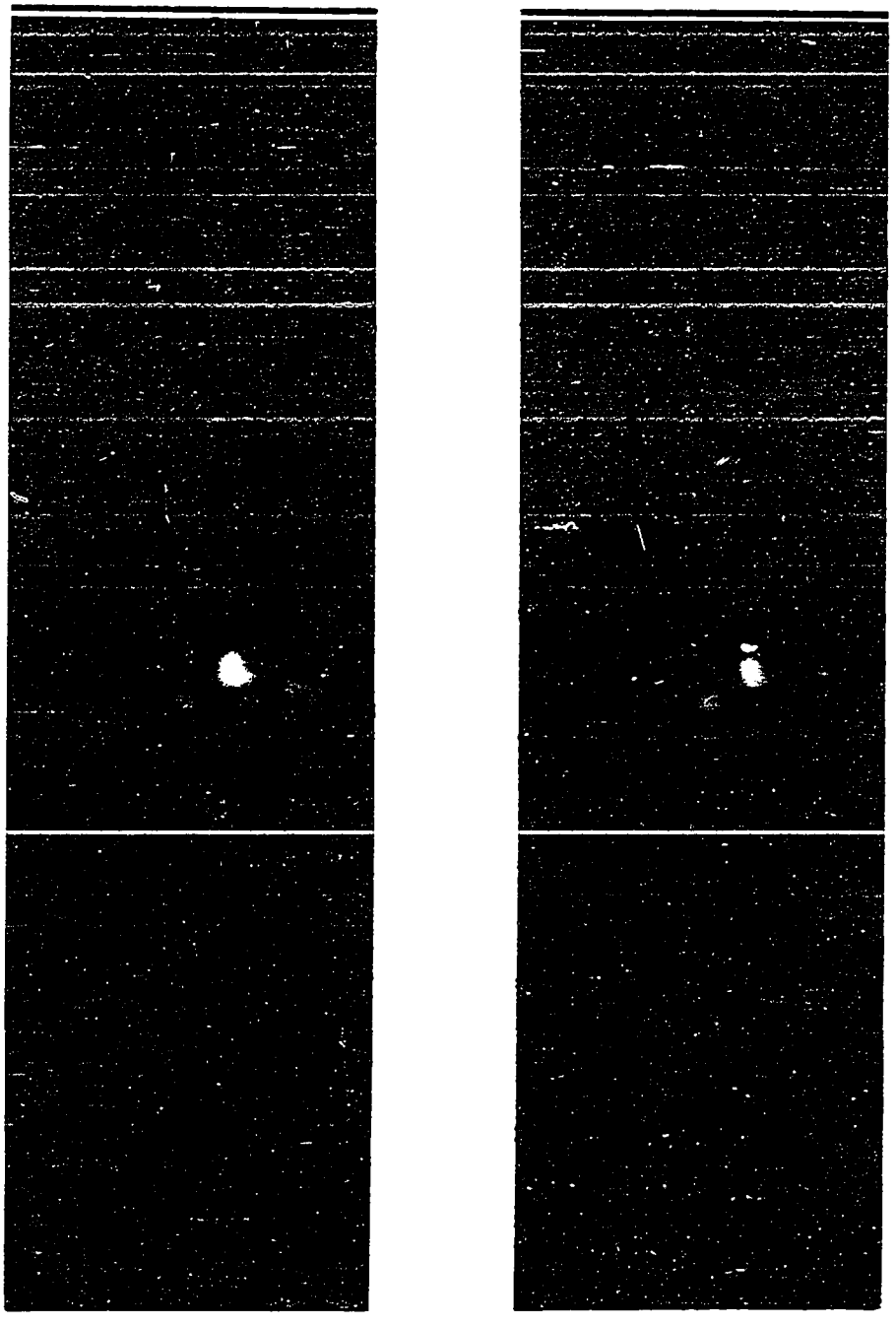

Figure 43. Two frames sample sequence of CR-39 color test strip for explosive loading

WAVE PROPAGATION

Kolsky (115, p. iii) states that

> "The theory of the propagation of elastic waves in solids was developed during the last century by Stokes, Poisson, Rayleigh, Kelvin, and others as an extension of the theory of elasticity to the problem of vibrating bodies."

In working with experimental wave propagation, meaningful information cannot be obtained without some understanding of the mathematical approach. Analytic expressions together with experimentally measured values for phase velocities obtained in wave propagation studies in special geometries, such as rods and plates, were used to calculate the dynamic values of the elastic modulus and Poisson's ratio. In the first few sections, the generalized equations for plane and cylindrical waves will be reviewed briefly in order to evaluate the effects that any limiting assumptions may have on the computed values of the material properties. In the remaining sections, a theoretical solution as well as a numerical computer solution to the plane strain problem of the transient loading of a cylindrical cavity in an infinite elastic medium will be considered because of the similarity of these two different approaches to the current problem.

Plane Waves in Bars

An approximate theory of the propagation of a plane

wave in an isotropic, perfectly elastic bar can be derived if each cross section of the bar remains plane during the passage of longitudinal stress waves and the stresses over the cross are uniform. By neglecting body forces and utilizing Newton's second law of motion, an equation of motion is obtained from the forces acting on a small element in the uniform bar illustrated in Figure 44.

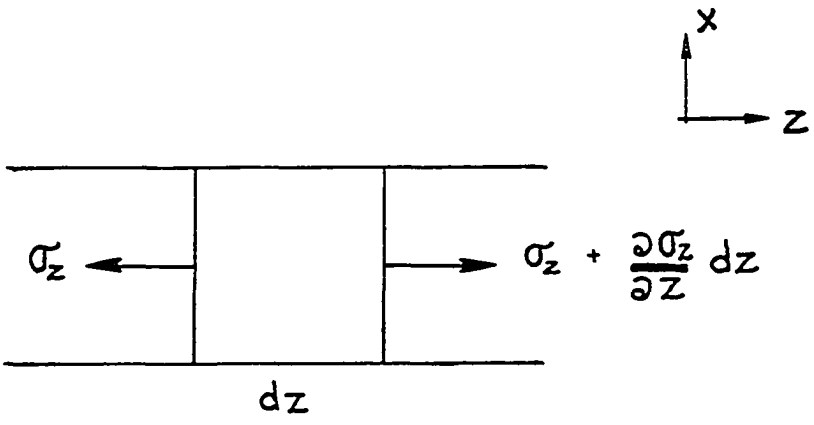

Figure 44. The one dimensional element

The equilibrium equation becomes

$$\rho A\, dz\, \frac{\partial^2 w}{\partial t^2} = A\, \frac{\partial \sigma_z}{\partial z}\, dz \qquad (3)$$

where

w = displacement of a cross section in the z direction

ρ = mass density

A = area of cross section

The relationship between stress and strain is obtained from the reduction of generalized Hooke's law to one dimension since

$$\sigma_y = \sigma_x = 0$$

Therefore,

$$\sigma_z = \left\{\frac{3\lambda + 2\mu}{\lambda + \mu}\right\} \epsilon_z \tag{4}$$

where:

λ = Lamés constant

μ = shear modulus

This can be rewritten in terms of the displacement in the z direction, w, as

$$\sigma_z = \left\{\frac{3\lambda + 2\mu}{\lambda + \mu}\right\} \frac{\partial w}{\partial z} \tag{5}$$

since the longitudinal strain, ϵ_z, is given by

$$\epsilon_z = \frac{\partial w}{\partial z} \tag{6}$$

By eliminating σ_z from Equations 3 and 5, the expression for plane waves moving in bars of any cross section, within the limiting assumptions, is given by

$$\frac{\partial^2 w}{\partial t^2} = \frac{1}{\rho}\left\{\frac{3\lambda + 2\mu}{\lambda + \mu}\right\} \frac{\partial^2 w}{\partial z^2} \tag{7}$$

which can be rewritten in terms of the elastic modulus as

$$\frac{\partial^2 w}{\partial t^2} = \frac{E}{\rho}\left\{\frac{\partial^2 w}{\partial z^2}\right\} = c^2 \frac{\partial^2 w}{\partial z^2} \tag{8}$$

since

$$E = \left\{ \frac{3\lambda + 2\mu}{\lambda + \mu} \right\} \mu \tag{9}$$

and where

$$C_o = \left\{ \frac{E}{\rho} \right\}^{1/2} \tag{10}$$

is the velocity of propagation of longitudinal waves along the bar.

The solution of Equation 8 is given by

$$w = f(C_o t - z) + g(C_o t + z) \tag{11}$$

where f and g are arbitrary functions depending on the initial conditions. The treatment is considered approximate since the basic assumptions made in the derivations are questionable. When the stress wave propagates down the bar, the longitudinal extensions and contractions will respond to Poisson's effect in lateral expansions and contractions of the bar. The consequence of this lateral motion may result in a nonuniform distribution of stress across the sections of the bars. As a result, the plane transverse sections would become distorted.

In addition to the uniformity of the stress, the velocity of propagation, C_o, derived from the approximate theory, is independent of the frequency of the stress waves. This nondispersive behavior, however, is only true for a stress pulse whose predominant wave lengths are long in comparison with the lateral dimensions of the bar.

An exact theory for longitudinal vibrations in

cylindrical bars has been obtained by Pochhammer (139) and Chree (140), where the stress wave velocity is a function of the wave length, and the longitudinal stress and displacements vary over the cross section of the bar.

In the current study, the characteristic stress waves were calculated to be of sufficient wave length that the one-dimensional mathematical model given previously provided suitable accuracy. Therefore, once the wave velocity, c, of a particular bar material is obtained from the experimental data, the dynamic modulus is easily obtainable since ρ is considered constant in linear elastic wave propagation.

Cylindrical Waves in Two Dimensions

Generalized plane stress

The generalized plane stress assumption in plates is valid when deformations are produced whose characteristic wave lengths are large compared to the plate thickness.

Since the wave that is generated by an explosion in a circular cavity is circumferential in geometry, the plate wave equation was derived in terms of a polar-coordinate reference frame. While neglecting body forces in an isotropic, perfectly elastic plate, consider the free body diagram of the polar element shown in Figure 45. Because of symmetry of geometry and loading, no shear stresses will be formed on the faces of the element.

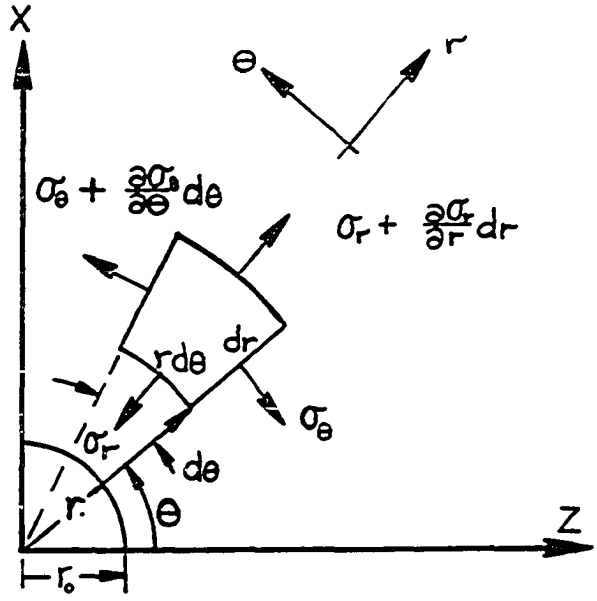

Figure 45. Free body diagram of polar element

In generalized plane stress, the elastodynamic field quantities are averaged across the thickness of the plate. For example, the average displacement in the radial direction, $U_r(r,t)$, is given by

$$U_r(r,t) = \frac{1}{h} \int_{-h/2}^{h/2} \underline{U_r}(r,y,t)dy \qquad (12)$$

where

h = thickness

$\underline{U_r}$ = actual three-dimensional radial component of displacment

From Newton's second law of motion, therefore

$$\left\{\sigma_r + \frac{\partial \sigma_r}{\partial r} dr\right\}\{r+dr\} h d\theta - \sigma_r h r d\theta$$
$$-\left[\sigma_\theta dr + \left\{\sigma_\theta + \frac{\partial \sigma_\theta}{\partial \theta} d\theta\right\} dr\right] \frac{d\theta}{2} h \qquad (13)$$
$$= \rho \frac{\partial^2 u_r}{\partial t^2} \{r\, dr\, d\theta\, h\}$$

which reduces to

$$\frac{\partial \sigma_r}{\partial r} + \left\{\frac{\sigma_r - \sigma_\theta}{r}\right\} = \rho \frac{\partial^2 u_r}{\partial t^2} \qquad (14)$$

as $d\theta$ and dr approach zero where σ_r and σ_θ are the average radial and tangential stresses in the plate. In order to obtain an expression for the plate wave velocity, Equation 14 must be written in terms of the displacement.

A relationship between stress and strain for the plate can be obtained from generalized Hooke's law for a state of plane stress where $\sigma_y = 0$, i.e. the radial stress is

$$\sigma_r = \frac{2\lambda\mu}{\lambda+2\mu}\left\{\epsilon_r + \epsilon_\theta\right\} + 2\mu\epsilon_r \qquad (15)$$

and the tangential stress is

$$\sigma_\theta = \frac{2\lambda\mu}{\lambda+2\mu}\left\{\epsilon_\theta + \epsilon_r\right\} + 2\mu\epsilon_\theta \qquad (16)$$

where

λ = Lamés constant

μ = shear modulus

In order to obtain a relation between strains and displacement, consider the deformation of element ABCD in

the quarter space shown in Figure 46 as it is displaced to position A'B'C'D'.

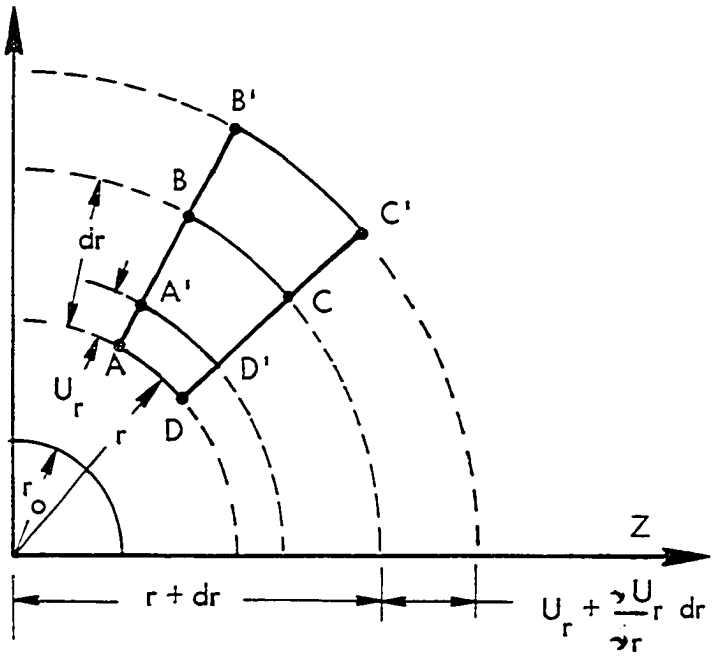

Figure 46. Deformation of a two dimensional element in a quarter space

The radial strain in terms of displacement is

$$\epsilon_r = \frac{u_r + \frac{\partial u_r}{\partial r} dr - u_r}{dr} = \frac{\partial u_r}{\partial r} \tag{17}$$

and the tangential strain becomes

$$\epsilon_\theta = \frac{2\pi (r + u_r) - 2\pi r}{2\pi r} = \frac{u_r}{r} \tag{18}$$

Combining Equations 15, 16, 17, and 18 yields

$$\sigma_r = \frac{2\lambda\mu}{\lambda + 2\mu} \left\{ \frac{\partial u_r}{\partial r} + \frac{u_r}{r} \right\} + 2\mu \frac{\partial u_r}{\partial r} \tag{19}$$

and

$$\sigma_\theta = \frac{2\lambda\mu}{\lambda+2\mu}\left\{\frac{u_r}{r} + \frac{\partial u_r}{\partial r}\right\} + 2\mu\,\frac{u_r}{r} \qquad (20)$$

Eliminating σ_r and σ_θ from Equations 14, 19, and 20, we obtain

$$\frac{\partial^2 u_r}{\partial r^2} + \frac{\partial}{\partial}\left\{\frac{u_r}{r}\right\} = \rho\left\{\frac{\lambda+2\mu}{4\mu(\lambda+\mu)}\right\}\frac{\partial^2 u_r}{\partial t^2} \qquad (21)$$

where the wave velocity is easily recognized as

$$C_L = \left\{\frac{4\mu(\lambda+\mu)}{(\lambda+2\mu)\rho}\right\}^{1/2} \qquad (22)$$

Recall that

$$E = \frac{\mu(3\lambda+\mu)}{\lambda+\mu} \qquad (9)$$

and since Poisson's ratio, ν, is given by

$$\nu = \frac{\lambda}{2(\lambda+\mu)} \qquad (23)$$

The wave velocity can be rewritten in terms of the elastic modulus and Poisson's ratio to give

$$C_L = \left\{\frac{E}{\rho(1-\nu^2)^2}\right\}^{1/2} \qquad (24)$$

Note that Equation 24 is the same expression derived by Kolsky for the phase velocity of a plane wave moving through a plate.

From the combination of Equations 14 and 10, along with the experimentally determined wave velocities C_0 and C_L, the dynamic value for Poisson's ratio is easily obtained.

Equations 4, 8, 9, 14, 15, 16, 21, and 23 can be written as one set of generalized equations for plane and cylindrical waves as done by Chou and Koenig, i.e. (141)

$$\frac{\partial \sigma_r}{\partial r} + \frac{N(\sigma_r - \sigma_\theta)}{r} = \rho \frac{\partial^2 u}{\partial t^2} \qquad (25)$$

$$\epsilon_r = \frac{\partial u_r}{\partial r} = \frac{1}{E}(\sigma_r - N\nu\sigma_\theta) \qquad (26)$$

$$\epsilon_\theta = N\left\{\frac{u}{r}\right\} = \frac{N}{E}\left\{\sigma_\theta\left[1-(N-1)\nu\right] - \nu\sigma_r\right\} \qquad (27)$$

and

$$\frac{\partial^2 u}{\partial r^2} + N\frac{\partial}{\partial r}\left\{\frac{u}{r}\right\} = \frac{1}{C^2}\frac{\partial^2 u}{\partial t^2} \qquad (28)$$

where N has a value of zero and one for plane and cylindrical waves respectively.

Generalized plane strain

Often it is convenient to utilize a generalized plane strain mathematical model in conjunction with a generalized plane stress experimental model. The two treatments are analogous (128) since the equations that must be satisfied for plane stress have the same form as those for plane strain with the exception of the Lamé constant combinations in generalized Hooke's law. For example, Equation 15 can be converted to the case of plane strain if $\frac{2\lambda\mu}{\lambda+2\mu}$ is replaced by λ and μ is left unchanged, which is equivalent to replacing ν by $\frac{\nu}{1-\nu}$. Therefore generalized Hooke's law for plane strain is written as

$$\sigma_r = \lambda (\epsilon_r + \epsilon_\theta) + 2\mu \epsilon_r \qquad (29)$$

Analytic approach Selberg (127) has considered theoretically the plane strain problem of the transient loading of a cylindrical cavity in an infinite elastic medium. His solution will be outlined here since the simple conversion from plane strain to generalized plane stress problems mentioned above makes Selberg's mathematical approach applicable to the current experimental problem.

Consider that at $t = 0$, the medium is in an unstressed state. For $t > 0$, a transient uniformly distributed pressure $P(t)$ is applied at $r = r_o$, $-\infty < y < \infty$, as illustrated in Figure 47.

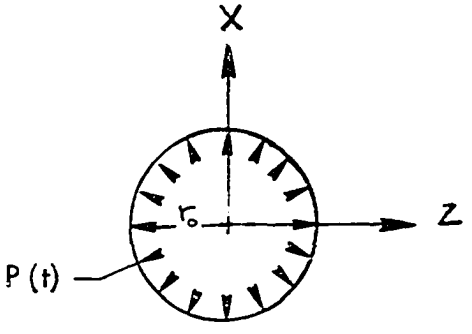

Figure 47. Uniformly distributed transient pressure applied to the boundary of a cylindrical cavity

From the basic field equation in the absence of body forces, recall

$$\frac{\partial \sigma_r}{\partial r} + \frac{\sigma_r - \sigma_\theta}{r} = \rho \frac{\partial^2 u_r}{\partial t^2} \qquad (14)$$

as well as Equations 17 and 18 where

$$\epsilon_r = \frac{\partial u_r}{\partial r} \qquad \text{and} \qquad \epsilon_\theta = \frac{u_r}{r}$$

If we now consider the first invariant of strain, J_1, with $\epsilon_y = 0$, then

$$J_1 = \epsilon_r + \epsilon_\theta \tag{30}$$

Eliminating ϵ_r and ϵ_θ from Equations 17, 18, and 30, then

$$J_1 = \frac{u_r}{r} + \frac{\partial u_r}{\partial r} = \frac{1}{r}\frac{\partial (r u_r)}{\partial r} \tag{31}$$

The radial stress can be rewritten, using Equations 29 and 30, in the form

$$\sigma_r = (\lambda + 2\mu) J_1 - 2\mu \frac{u_r}{r} \tag{32}$$

while the tangential stress becomes

$$\sigma_\theta = \lambda J_1 + 2\mu \frac{u_r}{r} \tag{33}$$

After eliminating σ_r and σ_θ from Equation 14, by use of Equations 32 and 33, and then taking the partial derivative with respect to r, the following form of the wave equation was obtained.

$$\frac{\partial^2 J_1}{\partial r^2} + \frac{1}{r}\frac{\partial J_1}{\partial r} = \left\{\frac{\rho}{\lambda + 2\mu}\right\} \frac{\partial^2 J_1}{\partial t^2} \tag{34}$$

where the wave velocity is given by

$$C_L = \left\{\frac{\lambda + 2\mu}{\rho}\right\}^{1/2} \tag{35}$$

Note that if Equation 34 is written in terms of U_r, i.e.

$$\frac{\partial^2 u_r}{\partial r^2} + \frac{\partial}{\partial r}\left\{\frac{u_r}{r}\right\} = \frac{\rho}{\lambda+2\mu}\frac{\partial^2 u_r}{\partial t^2} \tag{36}$$

then it is in the same form as Equation 21 with the exception of the wave speed.

The Laplace transform

$$\bar{J}_1(r,s) = \int_0^\infty J_1(r,t)\, e^{-st}\, dt \tag{37}$$

satisfies the differential equation

$$\frac{\partial^2 \bar{J}_1}{\partial r^2} + \frac{1}{r}\frac{\partial \bar{J}_1}{\partial r} = \frac{s^2}{c^2}\bar{J}_1 \tag{38}$$

which has a solution representing outgoing waves given by

$$\bar{J}_1 = \beta(s)\, K_0(\lambda r) \tag{39}$$

where $K_n(\lambda r)$ is a modified Bessel function of the second kind which is the solution to the differential equation

$$r^2 K'' + r K' - \left\{(r\lambda)^2 + n^2\right\} K = 0 \tag{40}$$

Since $\lambda = s/c$, then

$$\bar{J}_1 = \beta(s)\, K_0\left(\frac{rs}{c}\right) \tag{41}$$

Introducing the Laplace transform

$$\bar{\sigma}_r(r,s) = \int_0^\infty \sigma_r\, e^{-st}\, dt \tag{42}$$

we obtain from Equation 32

$$\bar{\sigma}_r = (\lambda+2\mu)\,\bar{J}_1 + \frac{2\mu}{r}\int_r^\infty \bar{J}_1 r\, dr \tag{43}$$

thus

$$\bar{\sigma}_r = \beta(s) \left\{ (\lambda+2\mu)\, K_0\left(\frac{rs}{c}\right) + \frac{2\mu c}{rs}\, K_1\left(\frac{rs}{c}\right) \right\} \quad (44)$$

where the second term in the bracket comes from the recurrence relations for $K_n\left(\frac{rs}{c}\right)$ (142).

If we let $r = r_0$ in Equation 44, then

$$\beta(s) = \frac{\bar{\sigma}_r(r_0, s)}{(\lambda+2\mu)\, K_0\left(\frac{r_0 s}{c}\right) + \frac{2\mu c}{r_0 s}\, K_1\left(\frac{r_0 s}{c}\right)} \quad (45)$$

Substituting Equation 45 into Equation 44 and inverting, we obtain

$$\sigma_r = \frac{1}{2\pi i} \int_{\omega-i\infty}^{\omega+i\infty} \frac{(\lambda+2\mu) K_0\left(\frac{rs}{c}\right) + \frac{2\mu c}{rs} K_1\left(\frac{rs}{c}\right)}{(\lambda+2\mu) K_0\left(\frac{r_0 s}{c}\right) + \frac{2\mu c}{r_0 s} K_1\left(\frac{r_0 s}{c}\right)} \bar{\sigma}_r(r_0, s)\, e^{st}\, ds \quad (46)$$

Given a mathematical expression for P(t) at the boundary,

$$\sigma_r(r_0, t) = -P(t) \quad (47)$$

then taking the Laplace transform

$$\bar{\sigma}_r(r_0, s) = \int_0^\infty -P(t)\, e^{-st}\, dt \quad (48)$$

and substituting into Equation 46, an exact expression is obtained for σ_r.

Selberg inverted Equation 46 explicitly for the case of step loading and gave some numerical results. However, in the case of more realistic loading profiles, such as obtained in the current study, the inversion is a long and tedious task which was left for future work because of the present limitations on funds and time.

Numerical computer approach (TOODY II) TOODY II is a Fortran code for computing the solution to wave propagation problems in two dimensions. The code was obtained from Sandia Laboratory in Albuquerque, New Mexico, since it appeared to be ideally suited for a numerical comparison of the current study. Since the code was originally written in C.D.C. 3600 Fortran, a great deal of time and effort (approximately 2 years) was spent in converting the code to an IBM 360 system in order to utilize the funded computer at this university. Although the author experimentally determined the material parameters that were required by the program for analysis, Professor T. R. Rogge* performed the actual conversion of the program. With the present limitation on funds, the complete pulse shape was not obtained. However, the author believes that TOODY II is of significant importance to deserve some discussion other than a recommendation for future work.

Basically the code solves the finite difference analogs to the Langrangian equation of motion in two dimensions. In order to use the finite difference technique, a mathematical model has to be sectioned into a suitable mesh array. Since the technique is an approximate method, the

*Dr. T.R. Rogge is an Associate Professor of Engineering Mechanics at Iowa State University.

degree of approximation depends on the mesh sizes, mesh shape, and any artificial viscosity coefficients that are needed for smoothing.

The results obtained by the program are directly dependent on the constitutive equations or the equations of state describing the materials involved. Therefore, in order to obtain physically realistic results, realistic values have to be obtained and used for the material constants. The sensitivity of the results to the variation on any particular material constant has to be investigated as well. Therefore, when the constitutive equations and material constants are known, along with suitably chosen mesh sizes and viscosity coefficients, TOODY II is capable of reasonable accuracy.

As the program is somewhat involved and is over 1400 statements in length with numerous subroutines, no effort will be made here to list the program or explain its functioning. Rather the main concern in this text is to indicate how the problem was formulated and to briefly discuss the results obtained to date.

Since TOODY II will accommodate up to nine different materials in a single problem, the three materials involved in the current study were easily handled. A grid system was established with the radial sides designated by I and the concentric tangential sides designated by J (Figure 48). The x-z coordinate system was located with the origin at

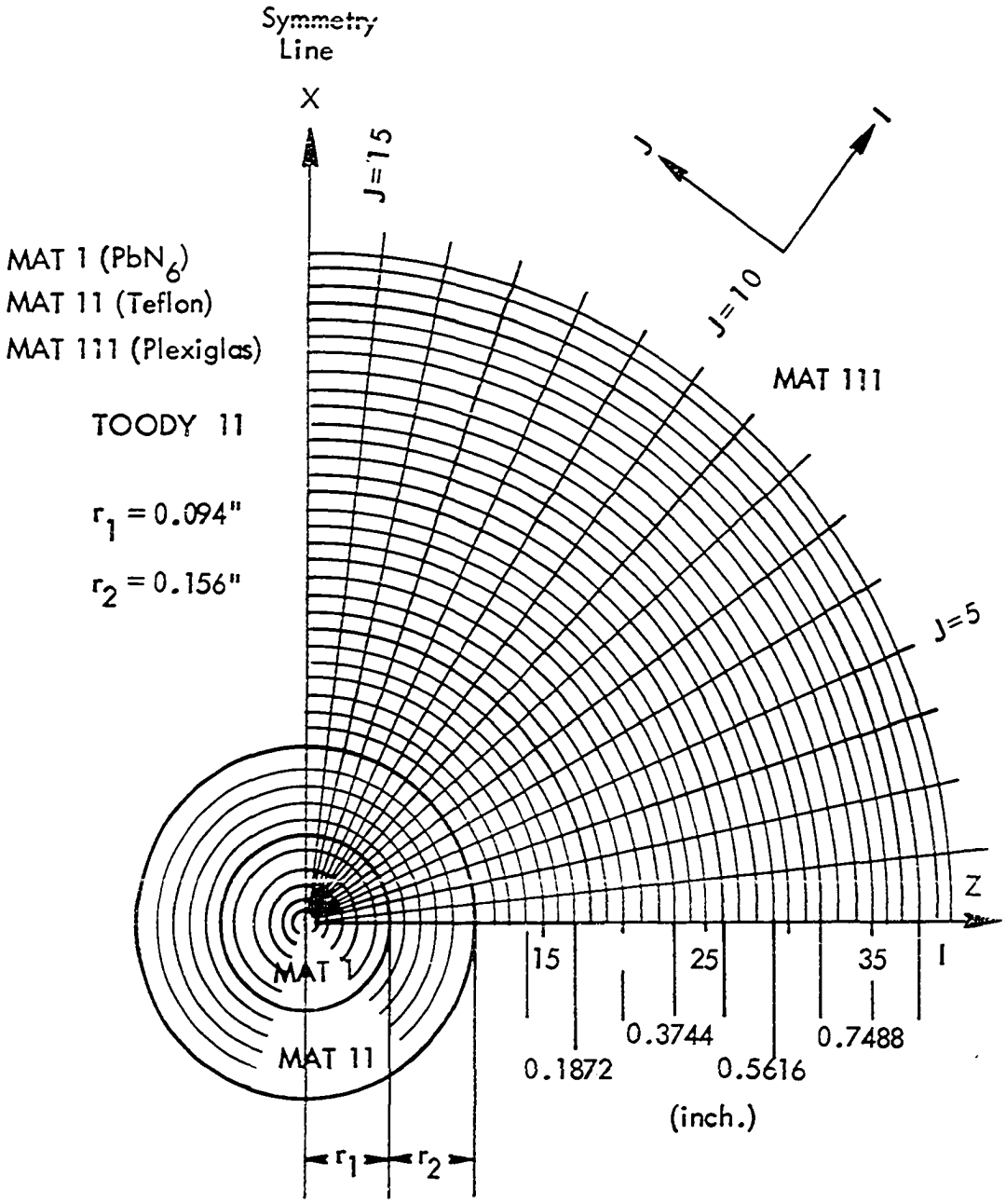

Figure 48. TOODY II output data meshes for current problem

the nucleus of the explosive charge. Since TOODY II requires a minimum of five grids in the radial direction, the explosive (Material I) was divided into 0.01875 inch radial increments. The Teflon (Material II) and the Plexiglas (Material III) were sectioned into 0.0312 inch increments. Sixteen equally spaced increments were established in the tangential direction. This was a minimum number in order that an individual mesh would not elongate and become unstable and distorted during the execution of the program.

The material parameters experimentally established for the different materials are listed in Table 5, Appendix E. The artificial viscosities as well as several other numerical parameters were obtained from tables supplied by Sandia.

The problem was so formulated, that once the lead azide was detonated at the nucleus, the burning would propagate out from the origin igniting each consecutive grid as a whole. A limiting shear stress was put on the Teflon such that when it reached 1000 psi, it would become perfectly plastic and not support additional load.

The numerical results obtained to date are presented and discussed in Appendix E.

DATA ACQUISITION

With the establishment of a suitable birefringent material, liner material, properly machined cavity, and suitable explosive, a new series of tests were conducted to establish the pulse transmitted to a birefringent model by the explosive loading.

After the plate model was prepared according to the forementioned procedure, increasing charges of PbN_6 were detonated in the charge cavities of increasing diameter until the model fractured with a charge of approximately 130 mg. of PbN_6. Thereafter, 120 mg. was established as the standard charge for all of the Teflon liner tests to avoid fracture which produces nonsymmetry in the fringe patterns. The charge of 120 mg. of PbN_6 could be lightly packed in a 0.188 inch diameter by 0.235 inch long cavity.

Once the liners were fitted in the models with the smoke shields, fiber reinforced tape was wrapped around the open end of the liner shield to direct the smoke to the upper half of the model. Since it was necessary to observe the isochromatics as they entered the model, an exploding wire detonator energized by the number one spark gap was used to ignite the explosive charge. Since ignition commenced as the first gap fired, several frames passed before the initial fringe was observed in the model. Figure 49 (shot 081) shows representative frames from a

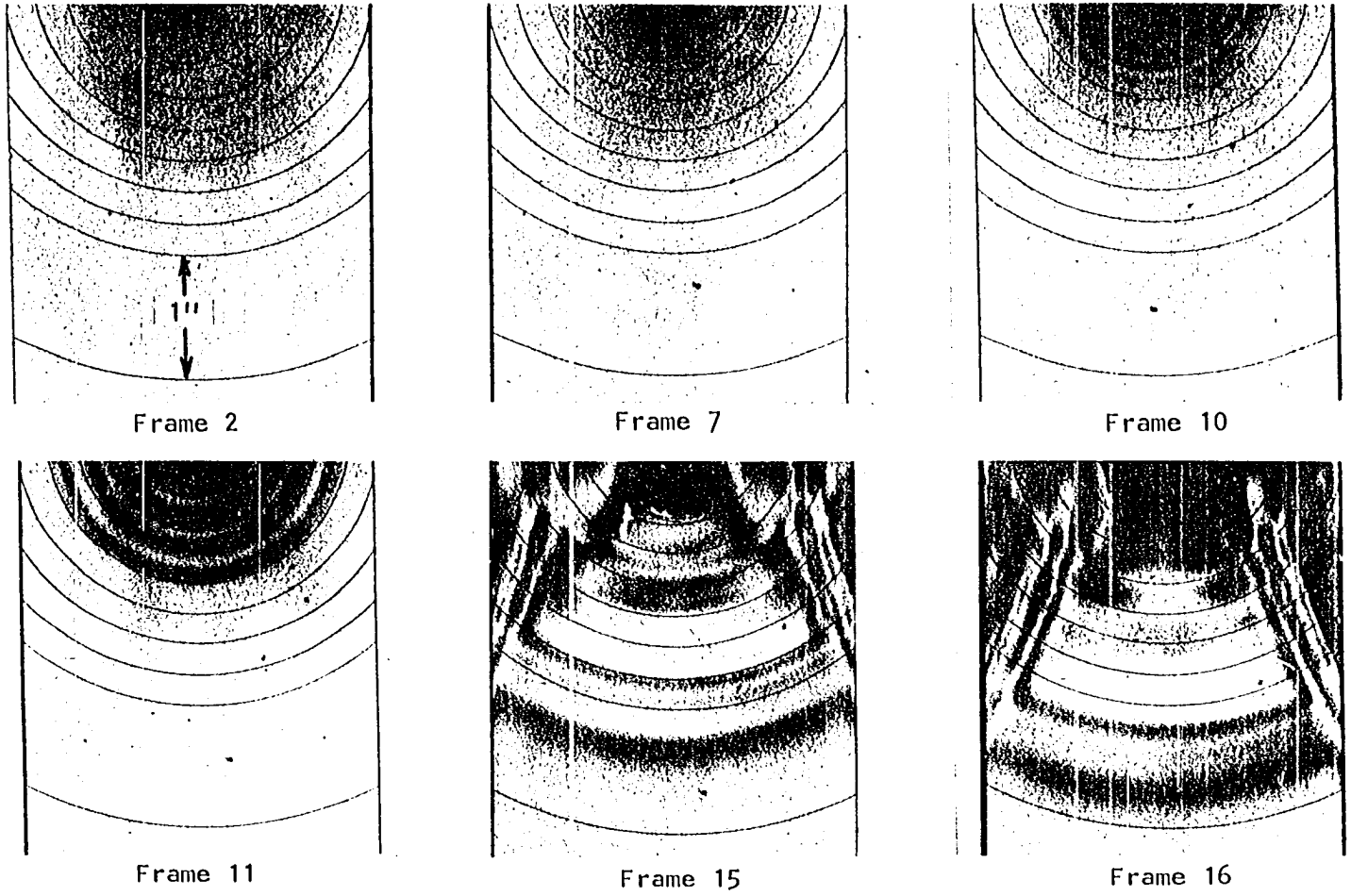

Figure 49. Six frame representation of the light field explosive pulse sequence (shot 081)

sixteen frame sequence in which it was found that the pulse had not been transmitted to the Plexiglas model by the sixth frame. Therefore, the first fringe was clearly recorded as it entered the model during the seventh frame. The thickness of the fringe indicated that it was traveling in excess of 100,000 inches/second.

Once the inductor taps were adjusted to produce the desired timing sequence, a variety of shots were taken. Since a large amount of information was needed to interpret the fringe patterns once they were obtained, both light (Figure 50) and dark (Figure 51) polarized fields were utilized on different tests under as close to identical conditions as experimentally possible. For light field sequences, one-half order fringes were obtained. This is the field commonly used in dynamic photoelastic studies since it transmits the greatest amount of light to the film plane. The information contained in the fringe patterns was sufficient to permit a relatively good evaluation of the shape of the stress wave. Since the true plate wave speed is measured with reference to the wave front, where the first fringe in a light field photograph represents a half fringe order, the slope of the fringe curve had to be extrapolated to the zero fringe in order to obtain the location of the wave front. With the dark field photographs, not only was a good representation of the shape of the stress pulse obtained, but an accurate location of the

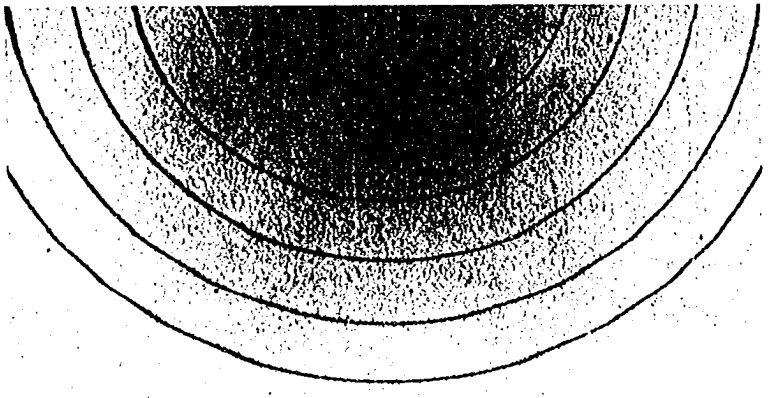

Frame 6

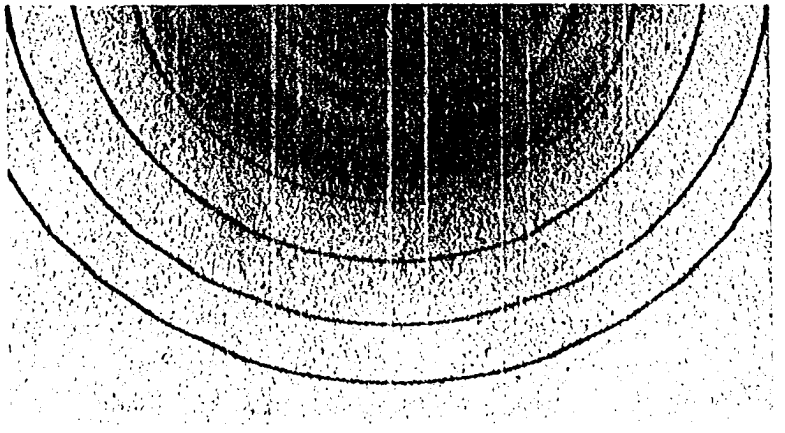

Frame 10

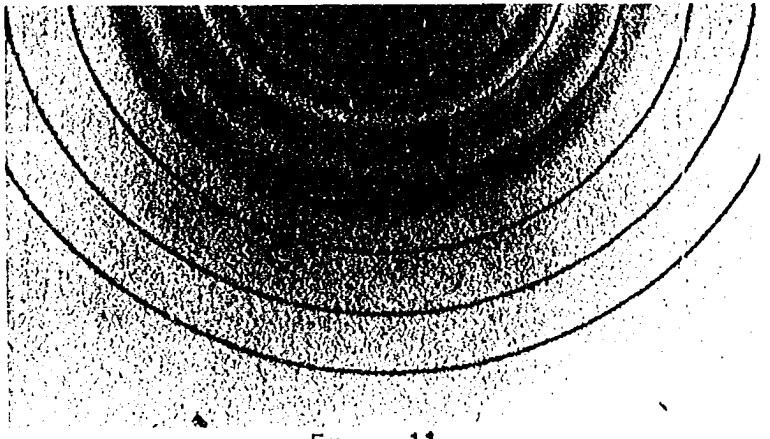

Frame 11

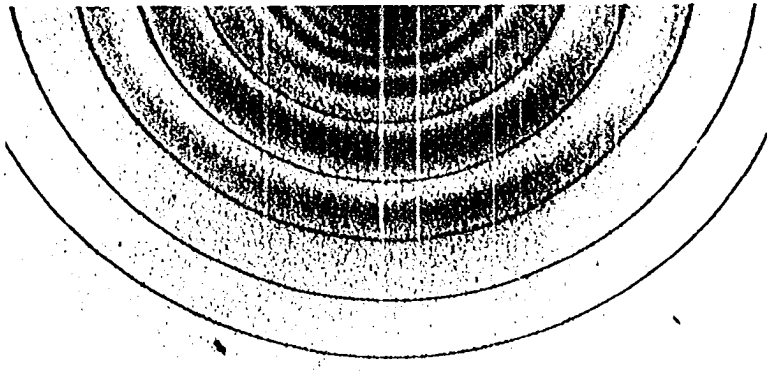

Frame 12

Figure 50. Light field explosive pulse sequence with 0.25 inch reference grid (shot 075)

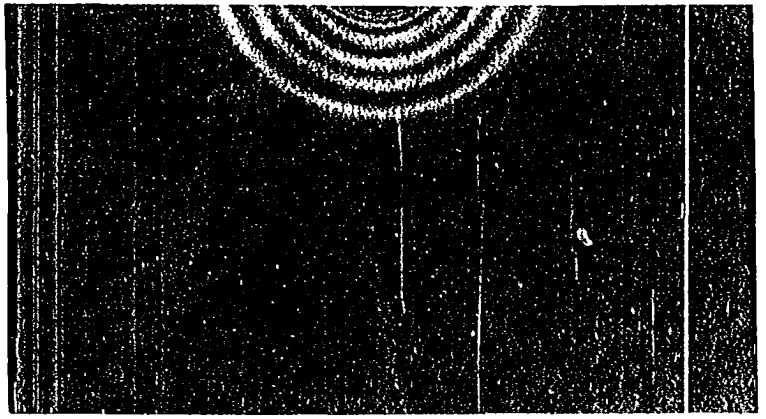

Frame 6

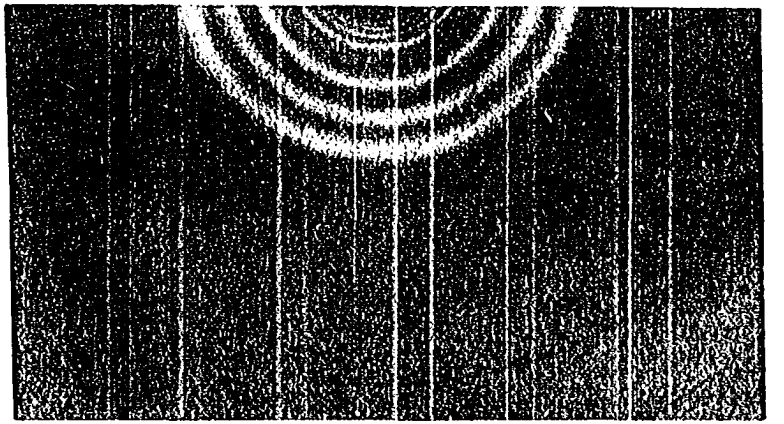

Frame 7

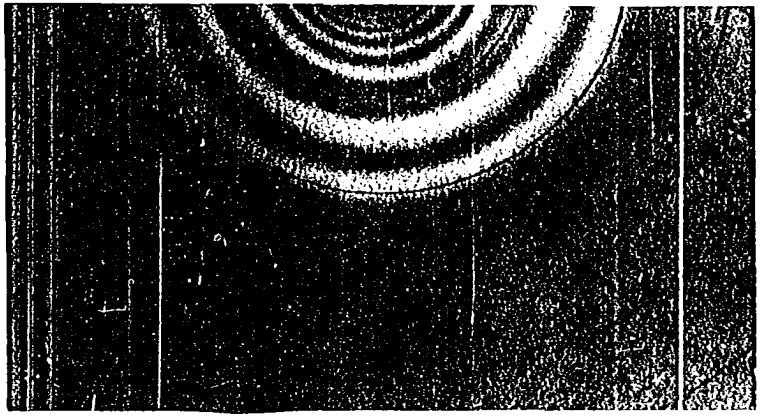

Frame 8

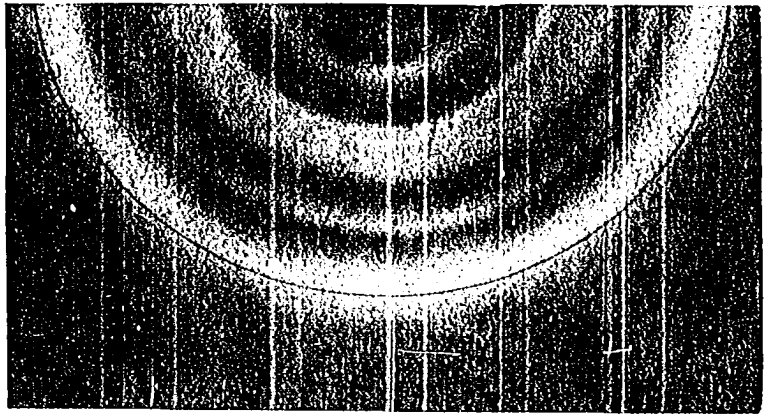

Frame 10

Figure 51. Dark field explosive pulse sequence with 0.5 inch reference grid

wave front was rendered since the zero fringe order was easily identified.

One of the major benfits of using an optically insensitive material such as Plexiglas was that the close field fringe density (Figure 52, Frame 11) was not beyond the resolution limits of the spark camera. On the other hand, an equivalent charge in CR-39 produced a fringe density (Figure 53, Frame 2) which could not be resolved when the wave had propagated the same distance in a geometrically identical plate.

In many previous dynamic photoelasticity investigations, far field information was obtained using sensitive materials such as CR-39. When the wave had propagated several inches into the model, the fringes were of sufficient number that they began to bundle into packets making fringe magnitude identification relatively simple (Figure 53, Frame 6). However, with the Plexiglas, the number of fringes diminished so rapidly as the wave propagated from the source that they were unable to separate into bundles before they were extinguished and identification became very difficult. In order to assist in identifying the magnitude of these close field bands, two methods were employed.

A strip of CR-39 was designed such that, after loading, the pressure dilitational (P_1) wave eventually struck a boundary (Figure 54). Once this occurred, a reflected shear wave (P_1S_1), which was quite sensitive to fringe

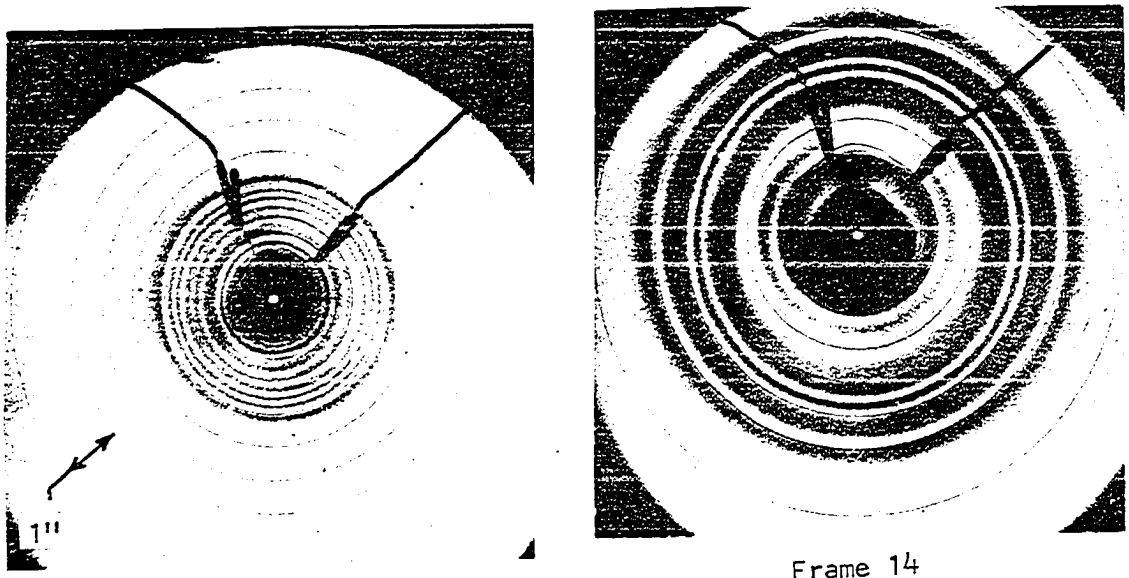

Frame 11 Frame 14

Figure 52. Explosive pulse symmetry and fringe density in Plexiglas

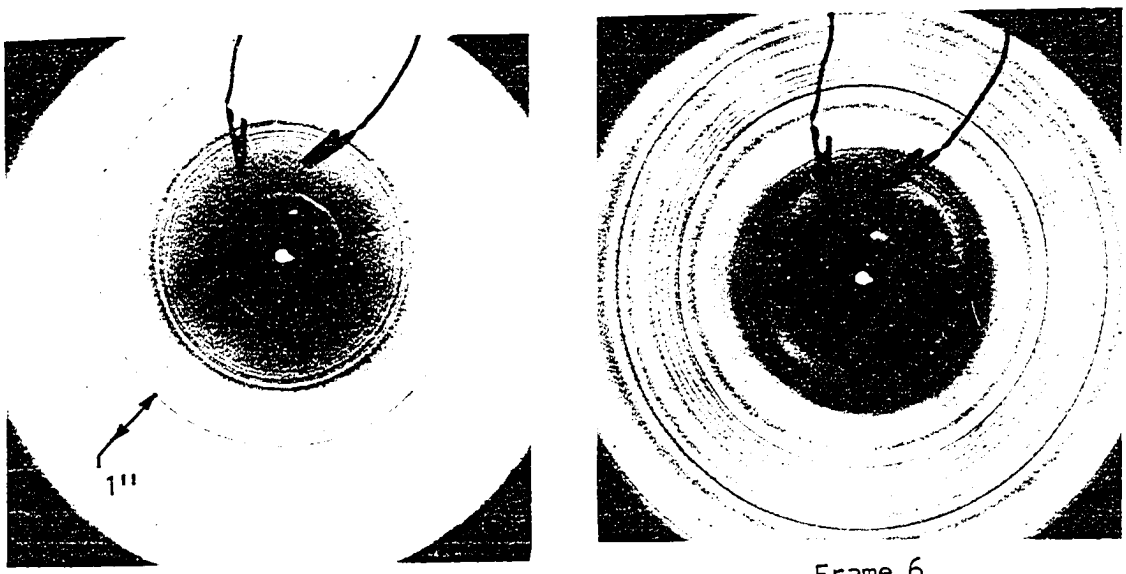

Frame 2 Frame 6

Figure 53. Explosive pulse symmetry and fringe density in CR-39

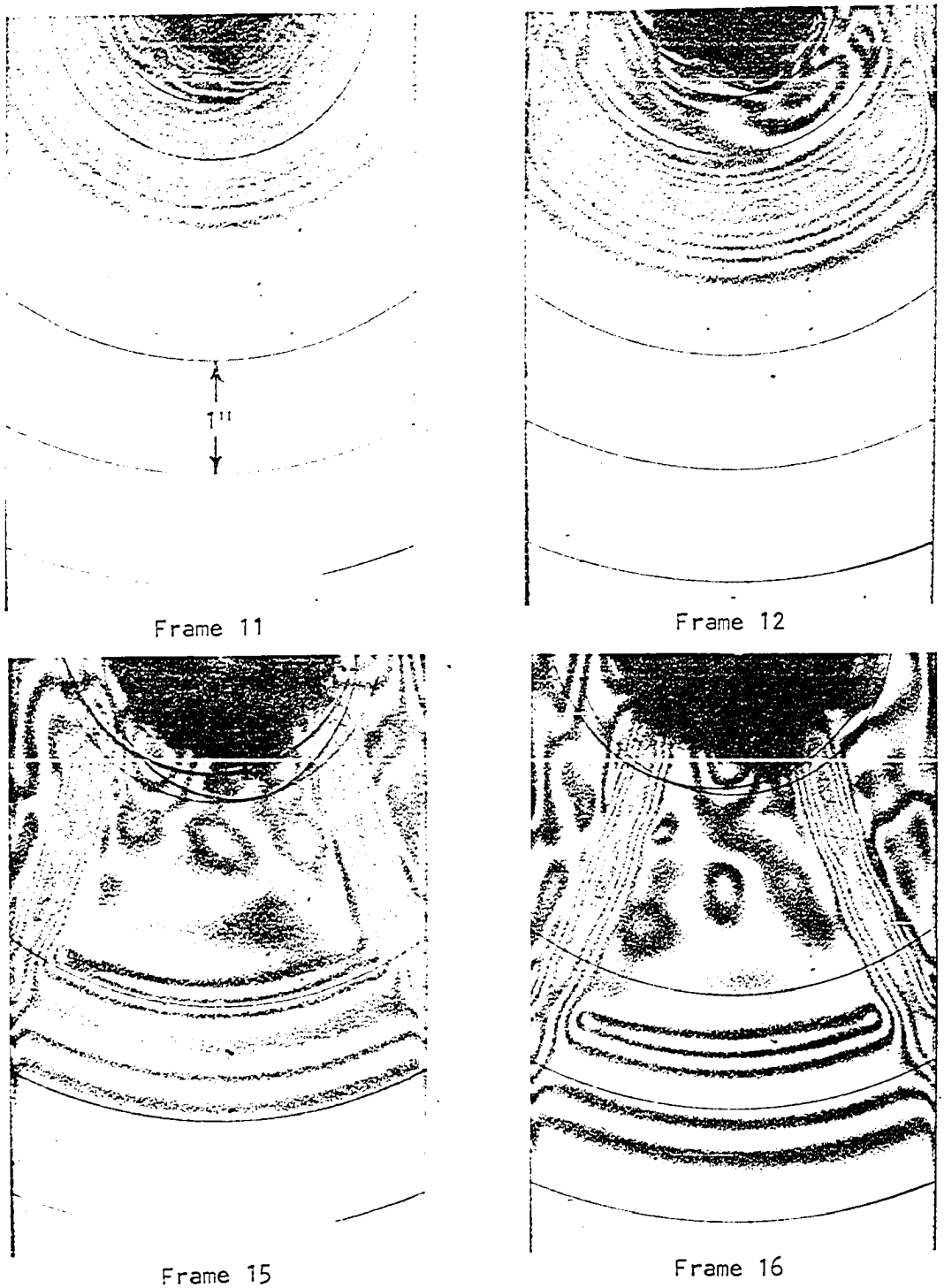

Figure 54. Four frame representation of an explosive pulse sequence in a 3 inch strip of CR-39

production because of the nature of the stress distribution was produced on the boundary. The relation between the P_1 and P_1S_1 waves is illustrated in Figure 55 which is an enlargement of Frame 16, Figure 54. A knowledge of the interaction of these two waves, as verified experimentally by using an optically sensitive material such as CR-39, allowed for the reliable interpretation of the fringe magnitudes on the outer limits of the close field study when Plexiglas was used as the model material.

By close observation of Figure 54 (Frames 15 and 16) and the enlargement of Figure 55 two overlapping dark bands can be distinguished in the region just outside of the propagating smoke. Each one of the two bands was the result of the photographic Schlieren effect which was created by the density gradient of the air shock. Two air shock waves appear in the photographs since part of the shock propagates down the back of the model while the remaining part moves down the front.

The magnitude of the highest order fringe to emerge from the boundary had to be identified before a pulse shape could be established. The location of the peak of the P_1 wave and its trailing zero order fringe were readily distinguishable from colored photographs of the sequence as illustrated in the sample Frame 9, ($t = 20.7$ micro-seconds) in Figure 56. By starting at the front of the wave disturbance in Figure 56, the corresponding initial

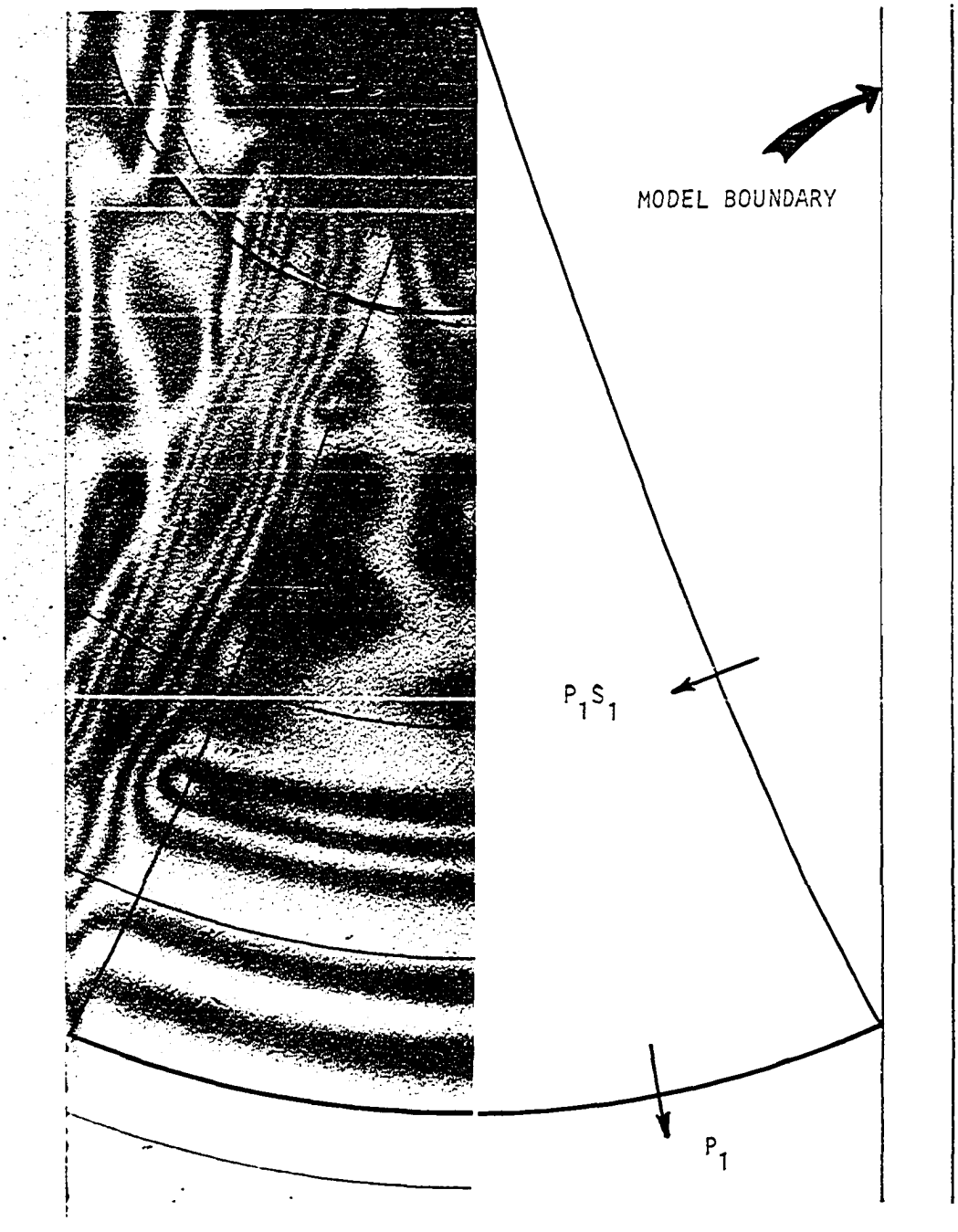

Figure 55. Enlargement of CR-39 strip with extensional (P_1) and reflected distortional waves (P_1S_1) indicated

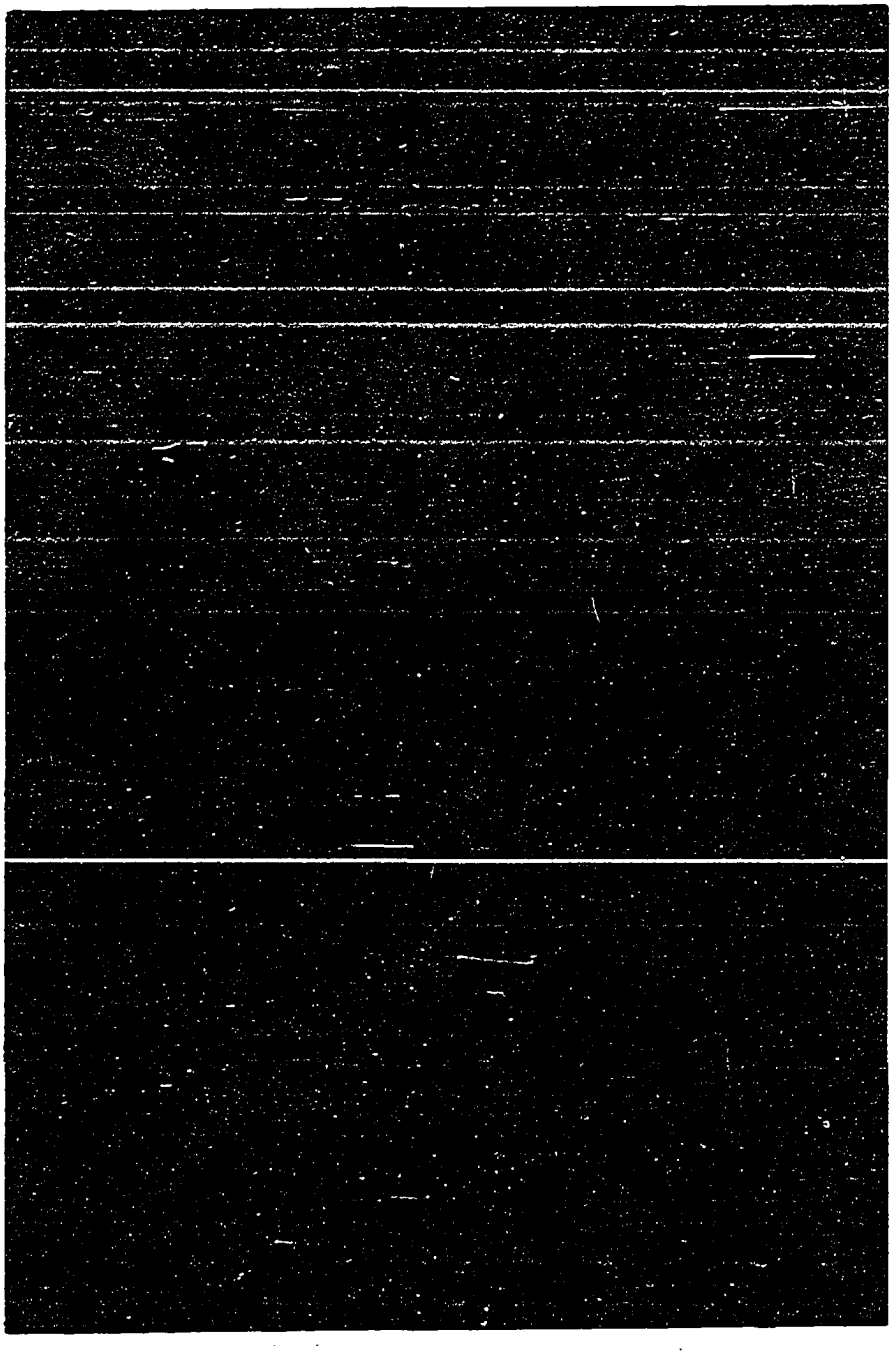

Figure 56. Color photograph of a dark field cylindrical wave in Plexiglas model with 0.25 inch reference grid

colors appear to be light blue-grey, yellow, orange, purple and deep blue. Since the next color begins to repeat the spectrum with purple being followed by orange, yellow, blue-grey, and finally black, the peak of the wave is clearly located in the deep-blue region with the zero order fringe just inside the 0.73 inch reference line. The strip of Kodak 34-A filter material was taped to one side of the hole to aid in the identification of fringe order at various points.

DATA REDUCTION AND RESULTS

Once a photographic record is obtained of a dynamic photoelastic event, experimental data is available in the form of full field stress difference information at different points in time. This isochromatic information has to be evaluated and separated into the parameters desired on a point to point basis. In order to interpret the fringe information correctly, a reference point must be established. Even in the most complicated static structure, reference points are easy to obtain since free corners and other points of zero shear are readily recognizable. However, in a dynamic fringe sequence of the current study, before any boundary interaction between the stresses had occurred, there was a lack of recognizeable reference points. Therefore, the colored pictures served to identify points of zero stress since they were the only points which appeared black. Once the zero fringe order was located, the fringe information was obtained with respect to its geometric locations on the model.

In order to locate the position of the wave front with respect to time, time sequence information had to be reliably interpreted from the oscilloscope trace of the spark sequence. At the lower speeds (500,000 frames per second or less) the trace was well defined as shown in Figure 17. However, at the high speeds (900,000 frames per

second or greater), the oscilloscope information was not as well defined because of the response limitations of the lite mike and the Model 547 oscilloscope. Since it was desirable to vary the framing rate between sparks in certain framing sequences, the average rate of a constant sequence was not acceptable as the correct time between any given frames. The reason for this was that when the framing rate was varied, certain gaps in time occurred periodically, i.e., if frames one through eight were operating at 1.5 microseconds between frames and nine through sixteen at 3 microseconds between frames, sometimes gaps of 4 or 5 microseconds would appear between given frames in the last half of the framing sequence. The gap was attributed to the variance in the interaction of induced voltages in the inductors which was caused by the large magnitudes of the magnetic fields that were collapsing in the inductor cabinet at different times. Since the lite mike recorded the time increments regardless of their sequence, the gap in time was of little consequence especially since a given inductor combination was reproducible from one sixteen frame sequence shot to the next.

Once the fringe orders were identified, they were plotted as a function of position, as shown in Figures 57 through 59.

Figure 57 is a representation of light field information plotted as a function of position. The information was

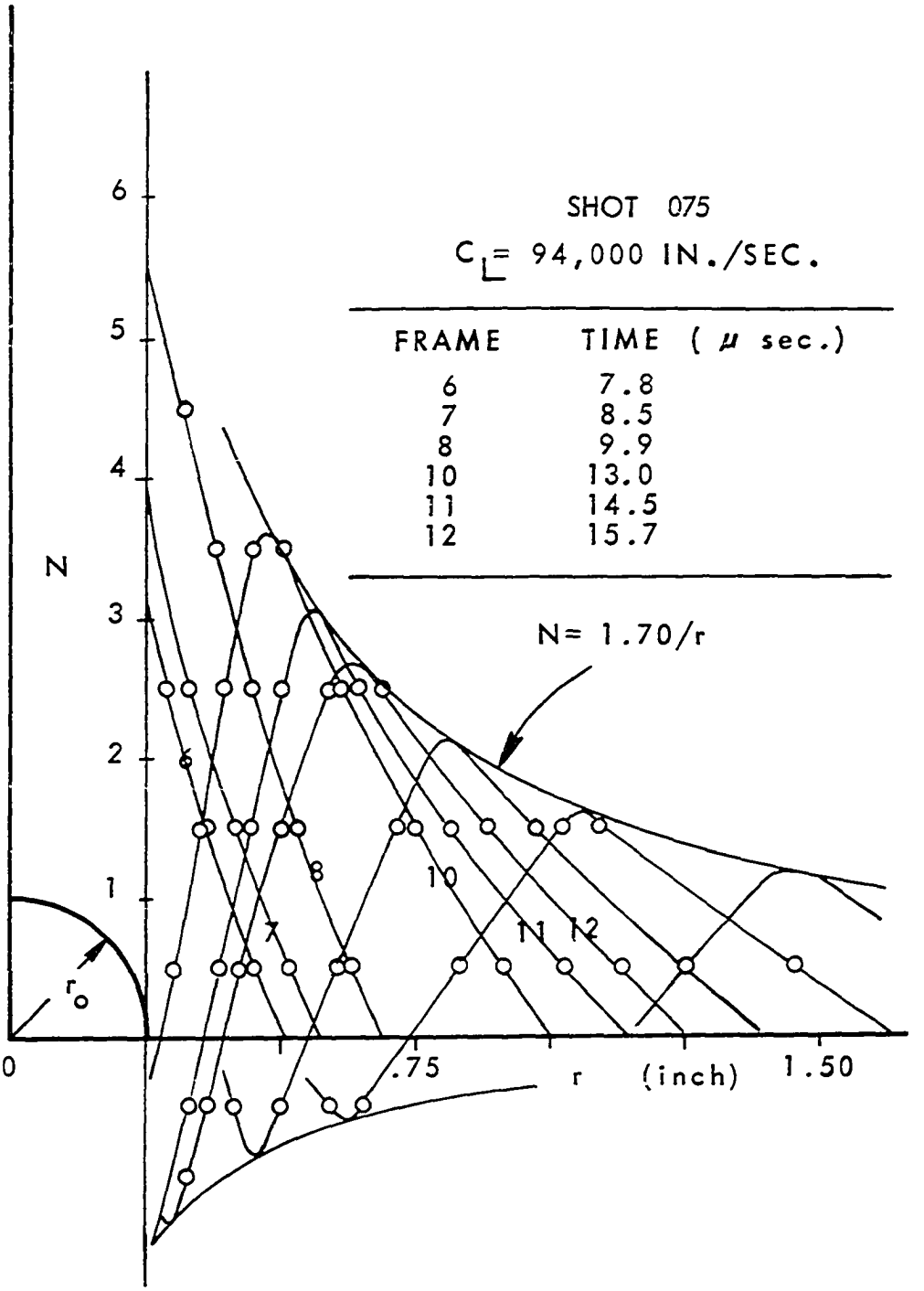

Figure 57. Light field fringe order as a function of distance at several times after the detonation of the lead azide charge (shot 075)

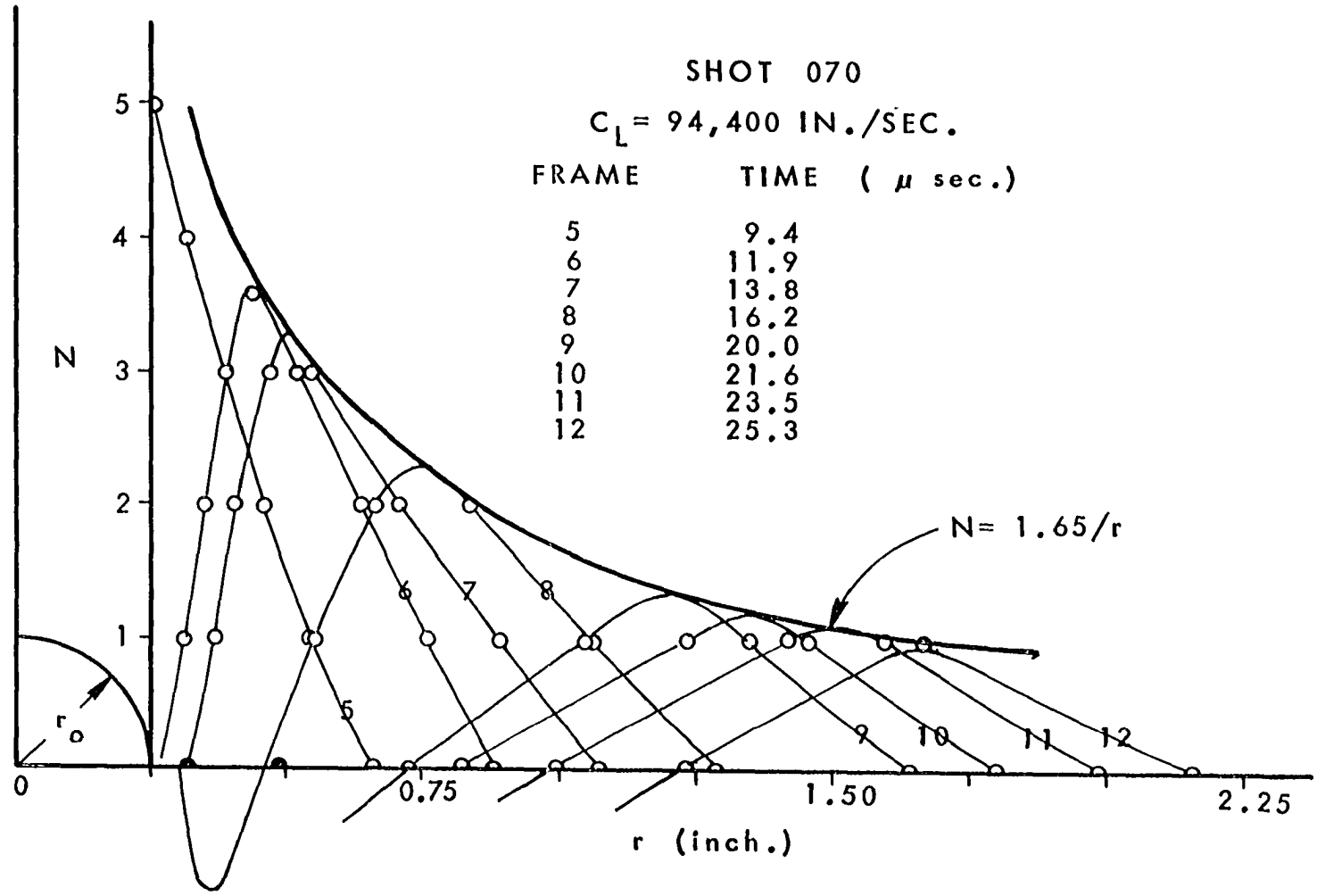

Figure 58. Dark field fringe order as a function of distance at several times after the detonation of the lead azide charge (shot 070)

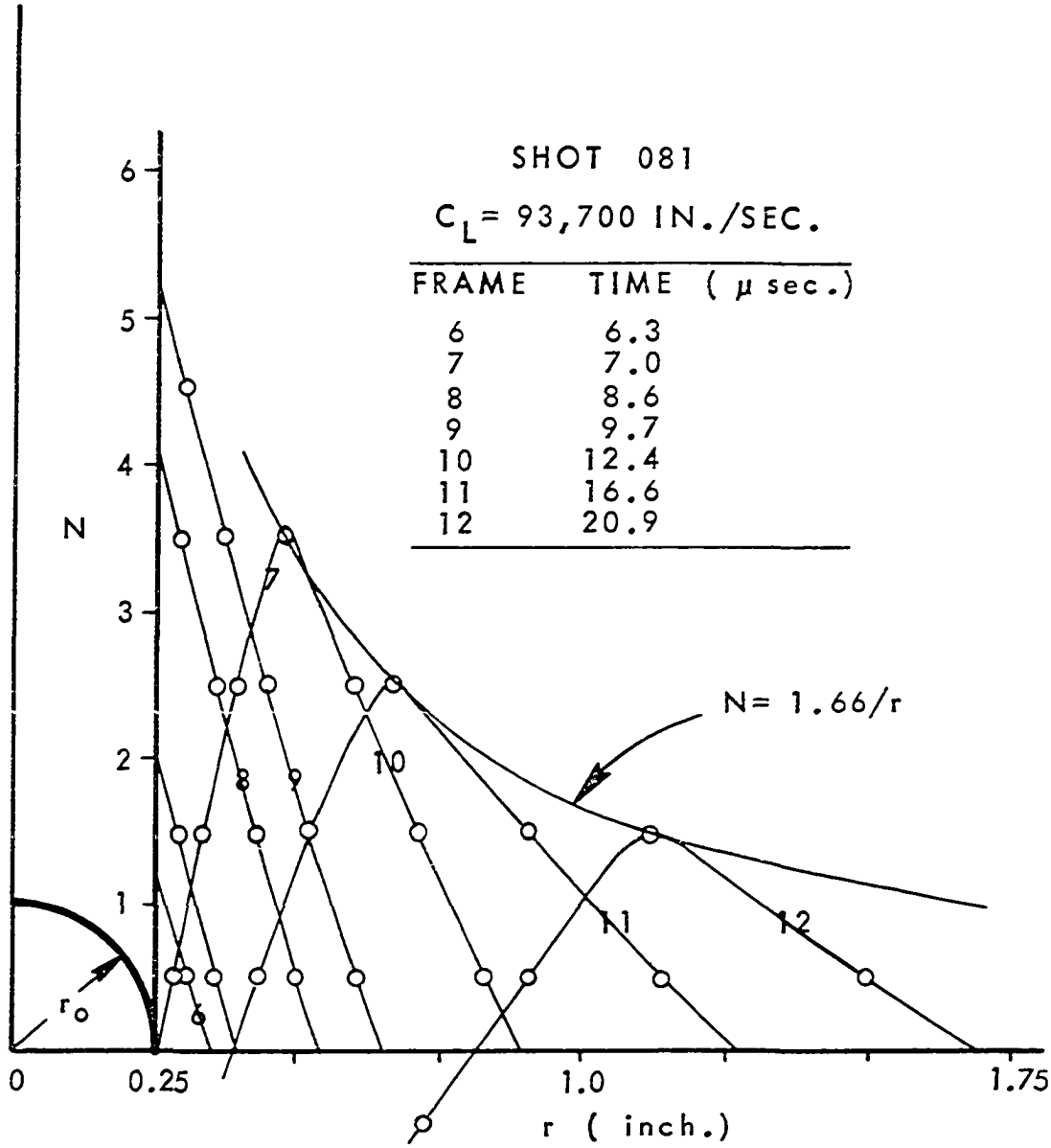

Figure 59. Light field fringe order as a function of distance at several times after the detonation of the lead azide charge (shot 081)

taken from the photographic data in which Figure 50 (shot 075) is a four sequence example. From an extrapolation of the one half fringe order to the wave front, which is of zero fringe order for the pulse location at a particular time, the plate velocity was calculated. This was used in conjunction with the rod wave speed obtained from the load cell to calculate the dynamic modulus. Since the wave front is determined by extrapolation, some error was expected in the process. To help assess the error as well as to acquire additional fringe information, the dark field sequence shown in Figure 51 (shot 070) was plotted as a function of position (Figure 58). Since dark field photographs define integer fringe orders, i.e., 0,1,2,...,N, then the zero order, which is on or very close to the wave front, was well defined. Therefore, this value was taken to represent the best average wave speed, C_L, of the plate.

For the purposes described on page 120, paragraph 3, a light field boundary sequence for Plexiglas was photographed (Figure 49). This sequence also provided infinite plate information, as plotted in Figure 59, during the time in which the wave propagated from the hole boundary until the P_1 pressure wave had interacted with the parallel boundaries of the strip. This produced a reflected P_1S_1 wave that eventually influenced the trailing tail of the P_1 wave.

Although over 100 explosive tests were conducted in the liner series, the three above mentioned shots, along with the dark field color sequence, were the predominate sources of full field information. This was not to say that segments of data from many of the other shots were not used, as well, in evaluating the information in these four shots. To the contrary, a large quantity of information was taken from many of the other tests. Point to point checks were made thoughout the analysis from the other data. Justification for using such a small number of shots to predict typical behavior in dynamic photoelasticity will be discussed in the Reproducibility section of the next chapter.

In all events, the time at which the first portion of a fringe enters the Plexiglas was determined by calculating the time required for the wave front to reach the first recorded zero order fringe location, based on the average velocity of the wave in the plate.

The point at which the P_1 wave front first entered the Plexiglas was then used as a reference time, t_1, for all data in order to evaluate that portion of the sequence attributed to detonation, burning, and transmission through the liner. Since this time varied from shot to shot, as shown in Table 2, the reference time, t_o, for light field shot number 075 was arbitrarily chosen as the time to which the times of all other shots would be shifted.

Table 2. Reference times

Shot Number	Field	t_1
075	light	5.3 μ sec.
070	dark	4.9 μ sec.
081	light	8.0 μ sec.

For example, results of shot 081 were adjusted by subtracting 2.7 microseconds from each time in its framing sequence. The shifts in time were mainly attributed to the variation in the exploding wire detonation from test to test. In addition to this, sub-microsecond control is beyond the scope of the present photographic system because of inherent delays in the system's circuitry.

Once the time sequences for all shots had been shifted to a common base, a plot of fringe order versus time at the boundary was prepared, Figure 60. Although lack of sub-microsecond control in the photographic system prevented the capturing of any data points on the decreasing part of the P_1 wave at the boundary, the fact that the wave was completely into the Plexiglas and the fringe order had returned to zero in less than 2.5 microseconds after the highest order fringe was recorded during the initial rise of the pulse, produced an outer limit of approximately 12.5 microseconds for the pulse duration. Although the shape of the pulse is not exact on the decaying side, a very close approximation was made by utilizing the shape of

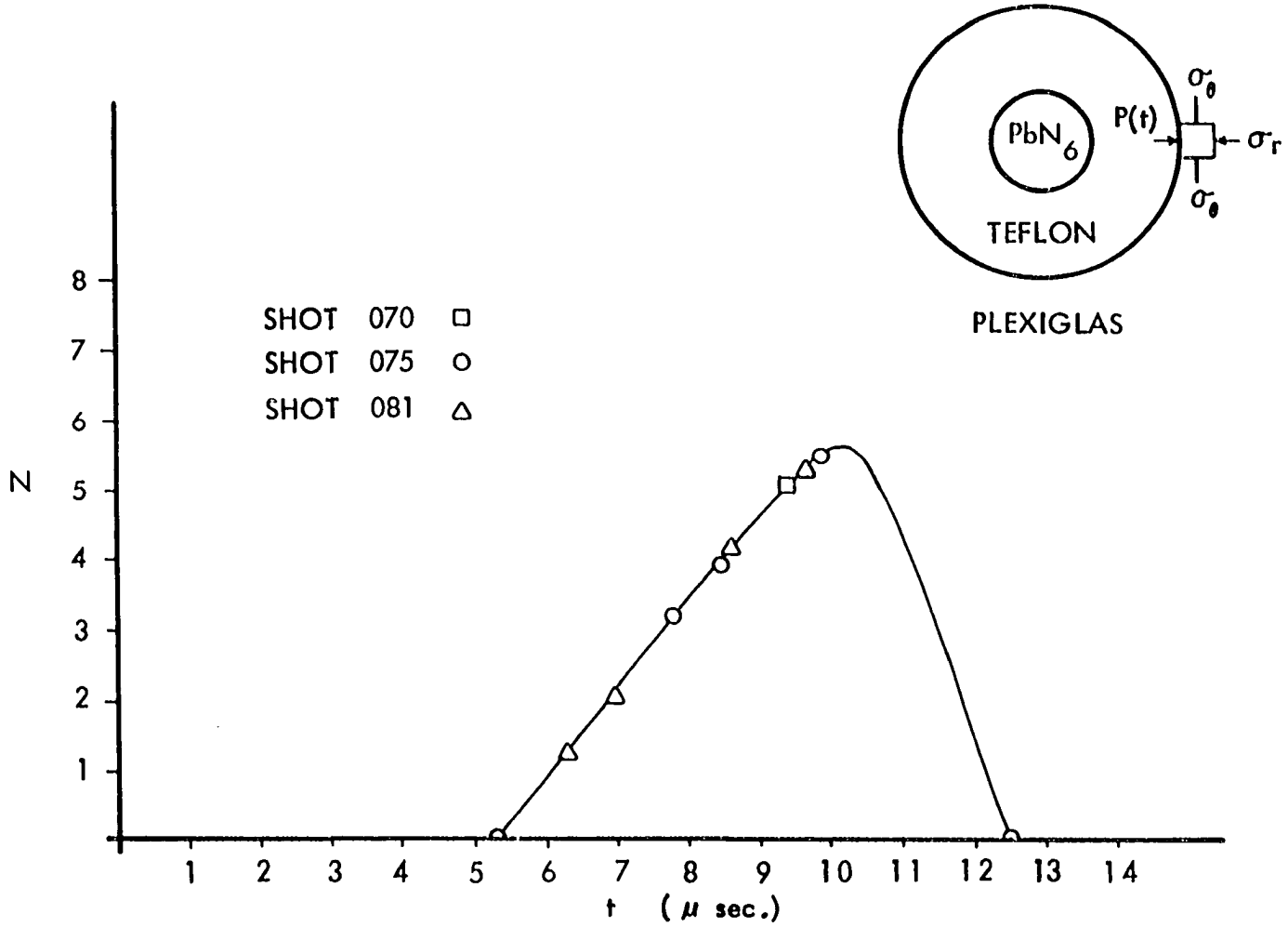

Figure 60. Fringe magnitude vs time at the Teflon-Plexiglas hole boundary

the tail of the first pulse completely into the Plexiglas. Again since this was a shape that had been relaxed slightly after it traveled through the material, it is repersentative of the worst case or the largest possible spread in the tail of the pulse. Since this description of the fringe order as a function of time is only an indication of how the difference in the secondary principal stresses, or the in-plane maximum shearing stresses, vary with time, the principal stresses were separated by the following numerical technique (77).

From Equation 2, the dynamic stress optic law can be written in the form

$$\sigma_\theta - \sigma_r = \frac{N (f_\sigma)_d}{h} \tag{49}$$

for cylindrical coordinates where σ_θ is algebraically larger than σ_r. In the event of a loading situation where only a pure dilitational wave propagates, in this case an incident P_1 wave, the principal stresses can be separated without introducing additional experimental data since these waves propagate without rotation. Although in-plane stresses occur both in the direction of wave propagation and perpendicular thereto, in-plane displacements are only present in the direction of wave propagation because of symmetry of geometry and loading. Therefore the displacements (U_r, U_θ) are written as

$$U_r = f(r) \tag{50}$$

and

$$U_\theta = 0 \tag{51}$$

For a pure P_1 wave propagating from a circular boundary without fracture, polar symmetry is exhibited such that the strain displacement equations are:

$$\epsilon_r = \frac{dU_r}{dr} \tag{17}$$

and

$$\epsilon_\theta = \frac{U_r}{r} \tag{18}$$

For the state of plane stress, the stress strain relations from generalized Hooke's law reduce to

$$\sigma_r = \frac{E}{1-\nu^2}(\epsilon_r + \nu\epsilon_\theta) \tag{52}$$

and

$$\sigma_\theta = \frac{E}{1-\nu^2}(\epsilon_\theta + \nu\epsilon_r) \tag{53}$$

since $\sigma_y = 0$

Subtracting Equation 52 from 53, an equation in terms of the difference in the principal stress is obtained, i.e.

$$\sigma_\theta - \sigma_r = \frac{E}{1+\nu}(\epsilon_\theta - \epsilon_r) \tag{54}$$

From the difference in Equations 17 and 18

$$\epsilon_\theta - \epsilon_r = \frac{U_r}{r} - \frac{dU_r}{dr} \tag{55}$$

which may be divided by r and written as

$$\frac{\epsilon_\theta - \epsilon_r}{r} = -\frac{d}{dr}\left(\frac{U_r}{r}\right) \tag{56}$$

Substituting Equation 56 into 54 yields

$$\frac{d}{dr}\left(\frac{U_r}{r}\right) = -\frac{(1+\nu)}{E}\frac{1}{r}(\sigma_\theta - \sigma_r) \tag{57}$$

Integrating both sides with respect to r,

$$\frac{U_r}{r} = -\frac{(1+\nu)}{E}\int_{r_1}^{r_2}\frac{(\sigma_\theta - \sigma_r)}{r}\,dr \tag{58}$$

Substituting Equation 49 into 58 and utilizing Equation 4,

$$\frac{U_r}{r} = \epsilon_\theta = -\frac{(1+\nu)(f_\sigma)_d}{E}\int_{r_1}^{r_2}\frac{N}{r}\,dr \tag{59}$$

Using Equation 59, a step by step numerical integration was performed to obtain tangential strains and radial displacements as a function of position as illustrated in Figures 61 and 62 for the first 12.4 microseconds of shot 081. From the point to point knowledge of ϵ_θ, the radial strain was calculated as shown in Figure 63 from the combination of Equations 49 and 54 in the form

$$\epsilon_r = \epsilon_\theta - \frac{(1+\nu)}{E}\frac{N(f_\sigma)_d}{h} \tag{60}$$

With ϵ_r and ϵ_θ known, the radial and tangential principal stress σ_r and σ_θ were calculated and plotted (Figures 64 and 65) from Equations 52 and 53.

Once ϵ_r, ϵ_θ, U_r, σ_r, and σ_θ were plotted as a function of position away from the explosive nucleus at

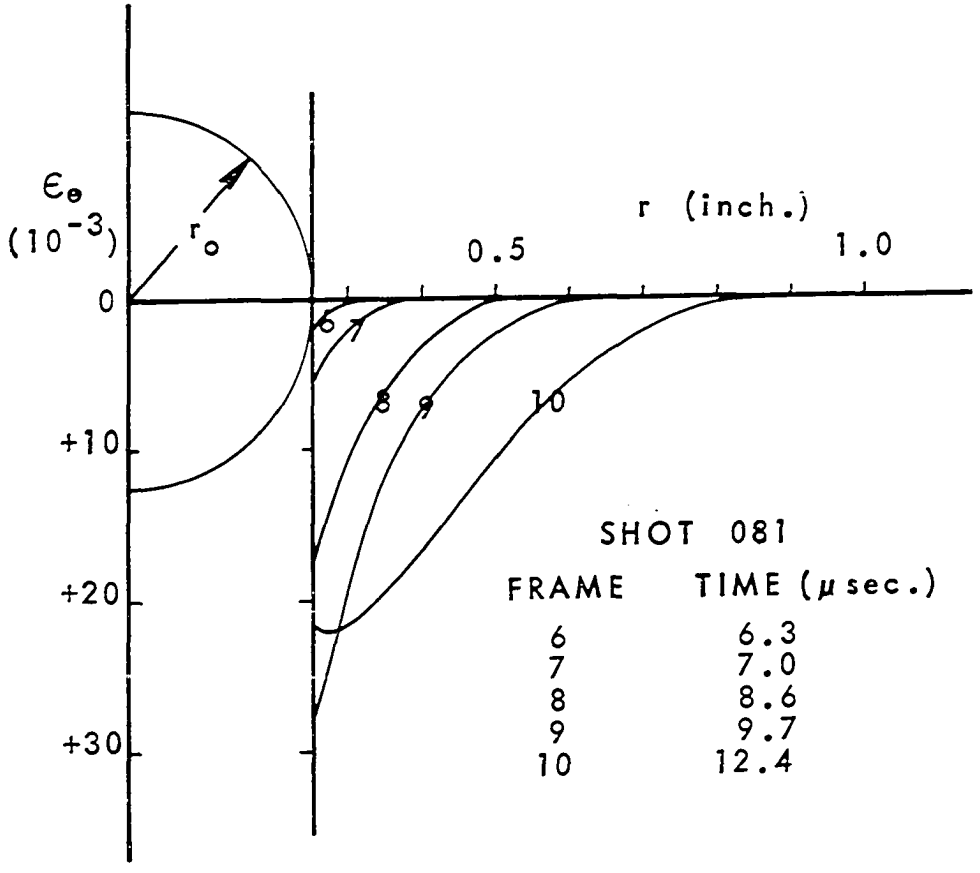

Figure 61. The formation of the tangential strain as a function of distance (shot 081)

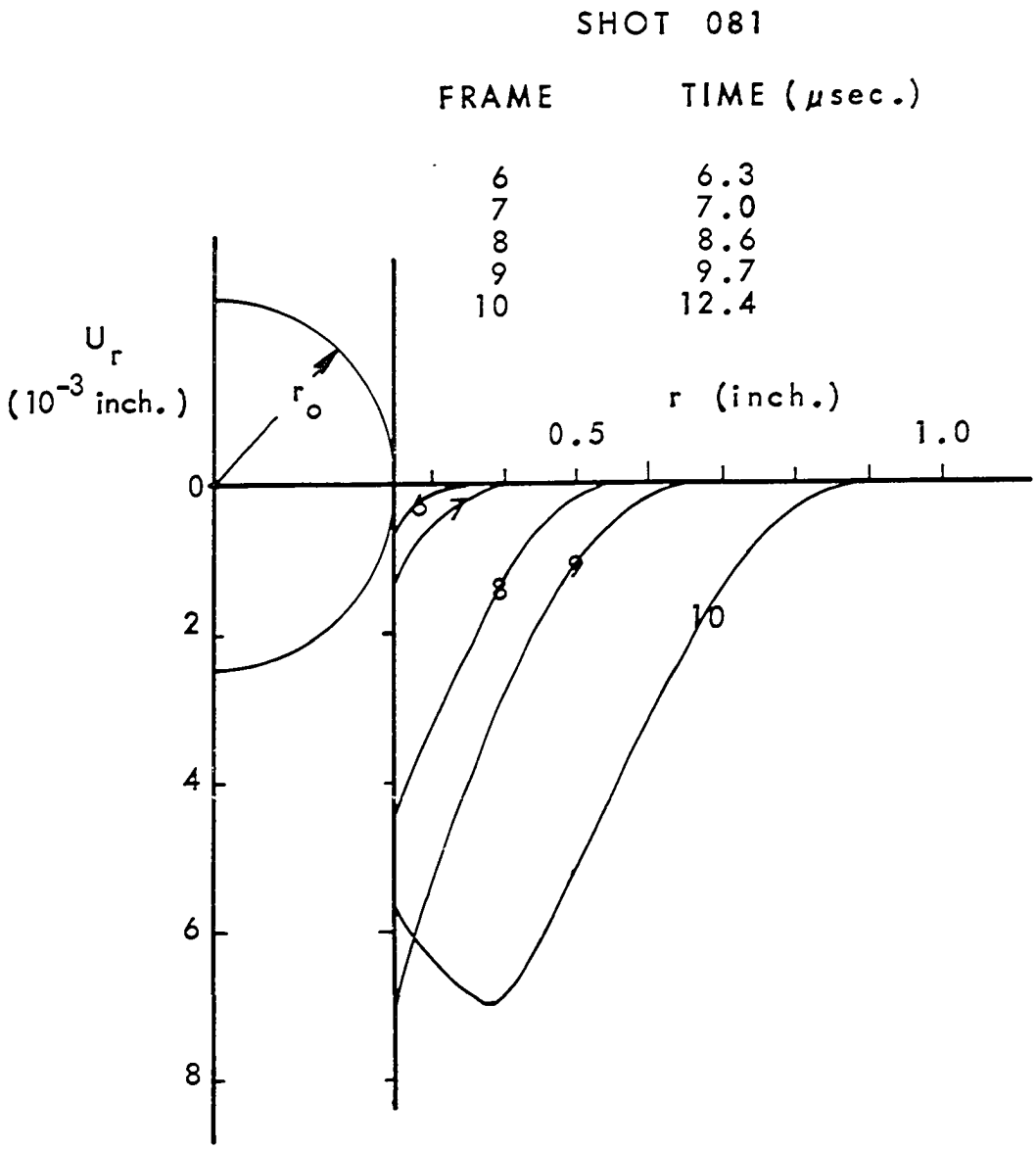

Figure 62. The formation of the radial displacement as a function of distance (shot 081)

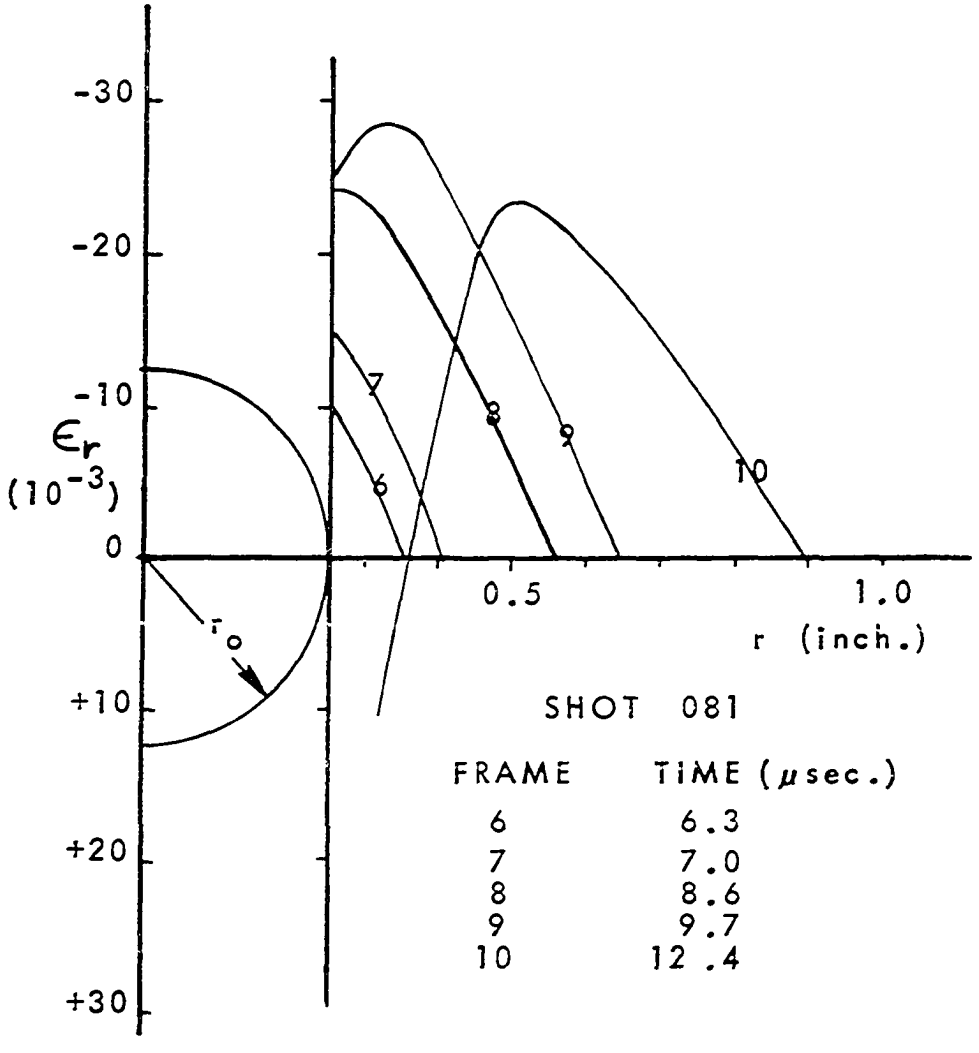

Figure 63. The formation and decay of the radial strain as a function of distance (shot 081)

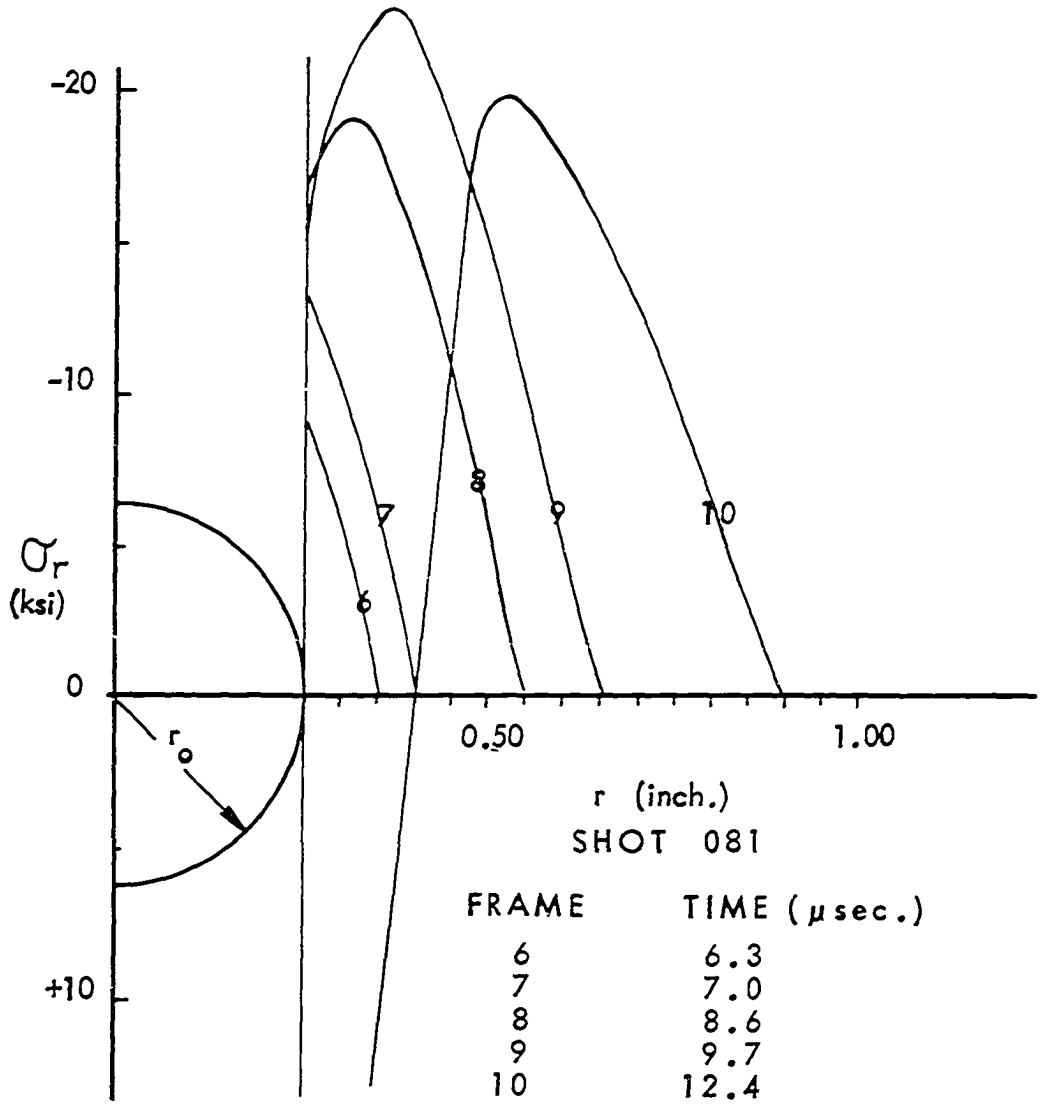

Figure 64. The radial stress formation and decay as a function of distance (shot 081)

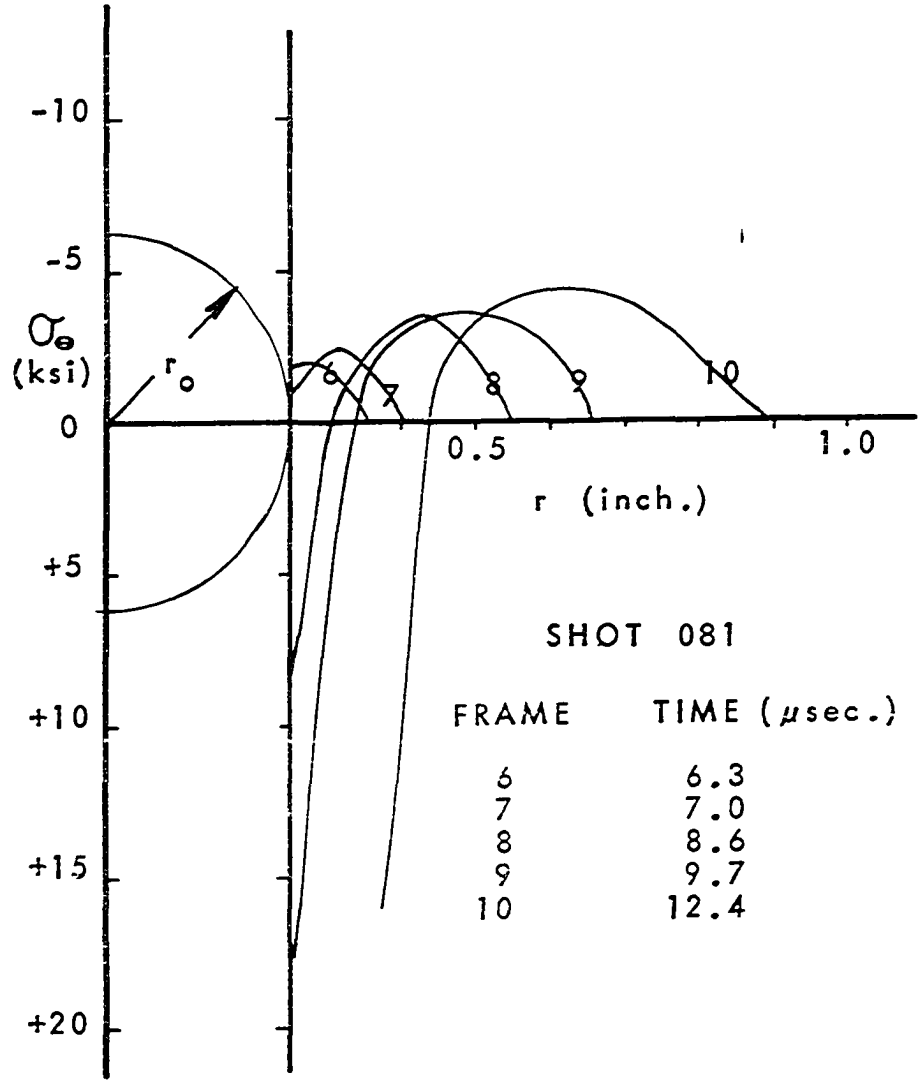

Figure 65. The formation of the tangential stress as a function of distance (shot 081)

different points in time, the individual parameters were all plotted as a function of time at the hole boundary as shown in Figures 66, 67, and 68. The radial stress at the boundary, or the input boundary pulse, P(t), was the main objective of the entire liner investigation. This gives an indication of the shape of an explosive loading function applied to a birefringent material without fracture via a thin protective and dissapative liner.

If the explosive could be applied directly to the plastic without deterioration from heat and fracture, the pulse would obviously be somewhat more abrupt and occur over a shorter length of time. Therefore, the lined hole presented a limiting case in which it is apparent the pulse can be of no longer duration.

A plot of the formation and decay of the maximum σ_r and σ_θ stresses in the material as a function of distance away from the nucleus of the charge was plotted in Figure 69. It is interesting to note that the radial stress just inside the boundary was higher than the pressure applied at the boundary. This will be discussed in the next chapter.

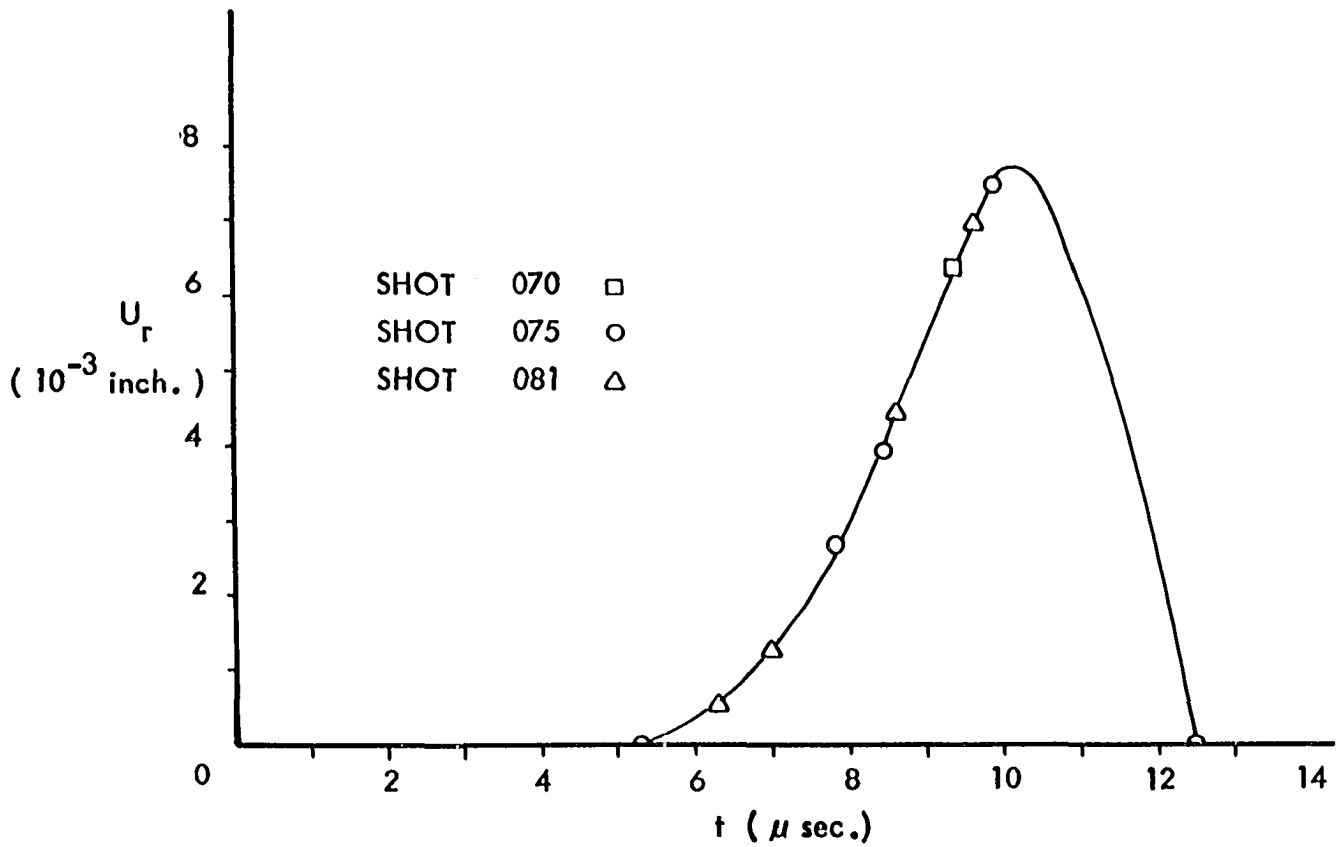

Figure 66. Radial displacement as a function of time at the Teflon-Plexiglas hole boundary

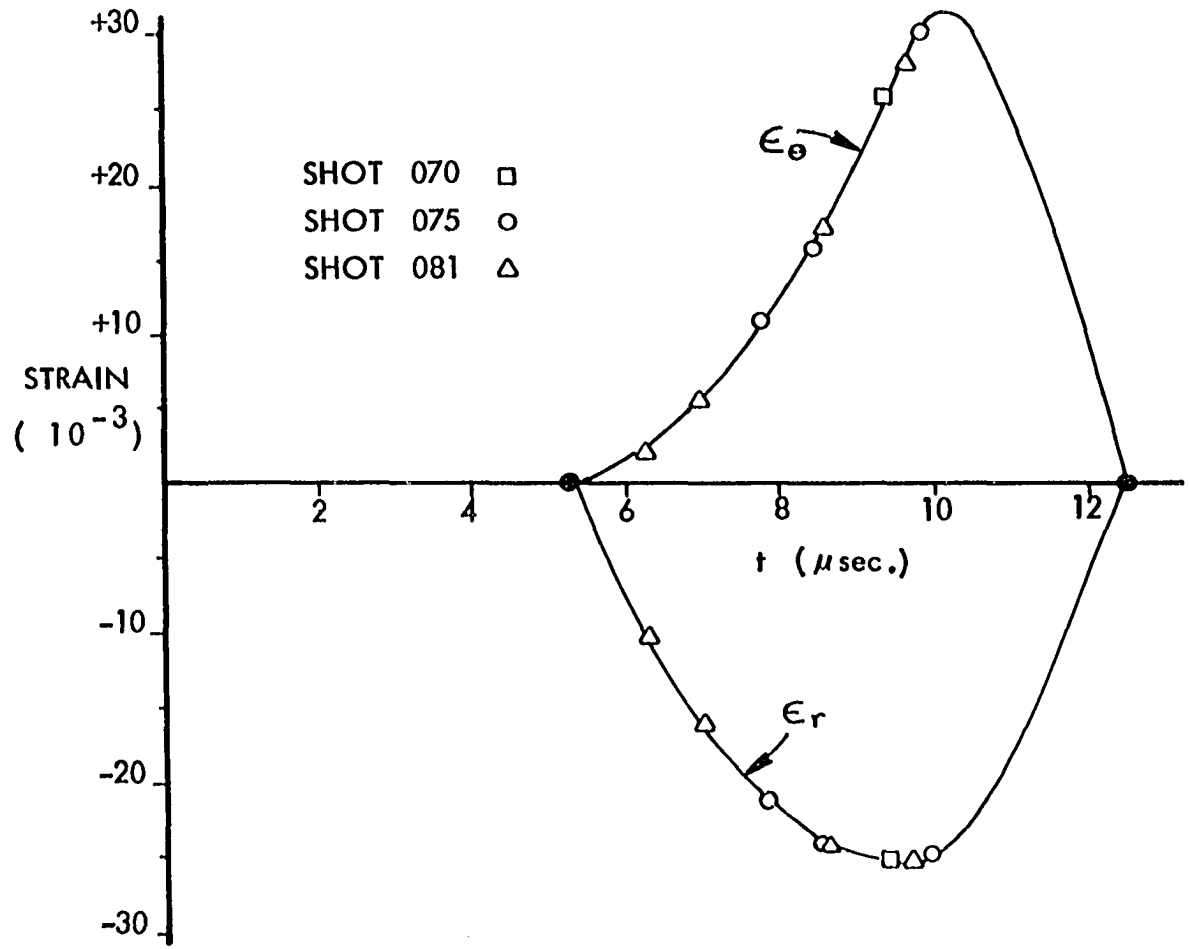

Figure 67. Radial and tangential normal strains as a function of time at the Teflon-Plexiglas hole boundary

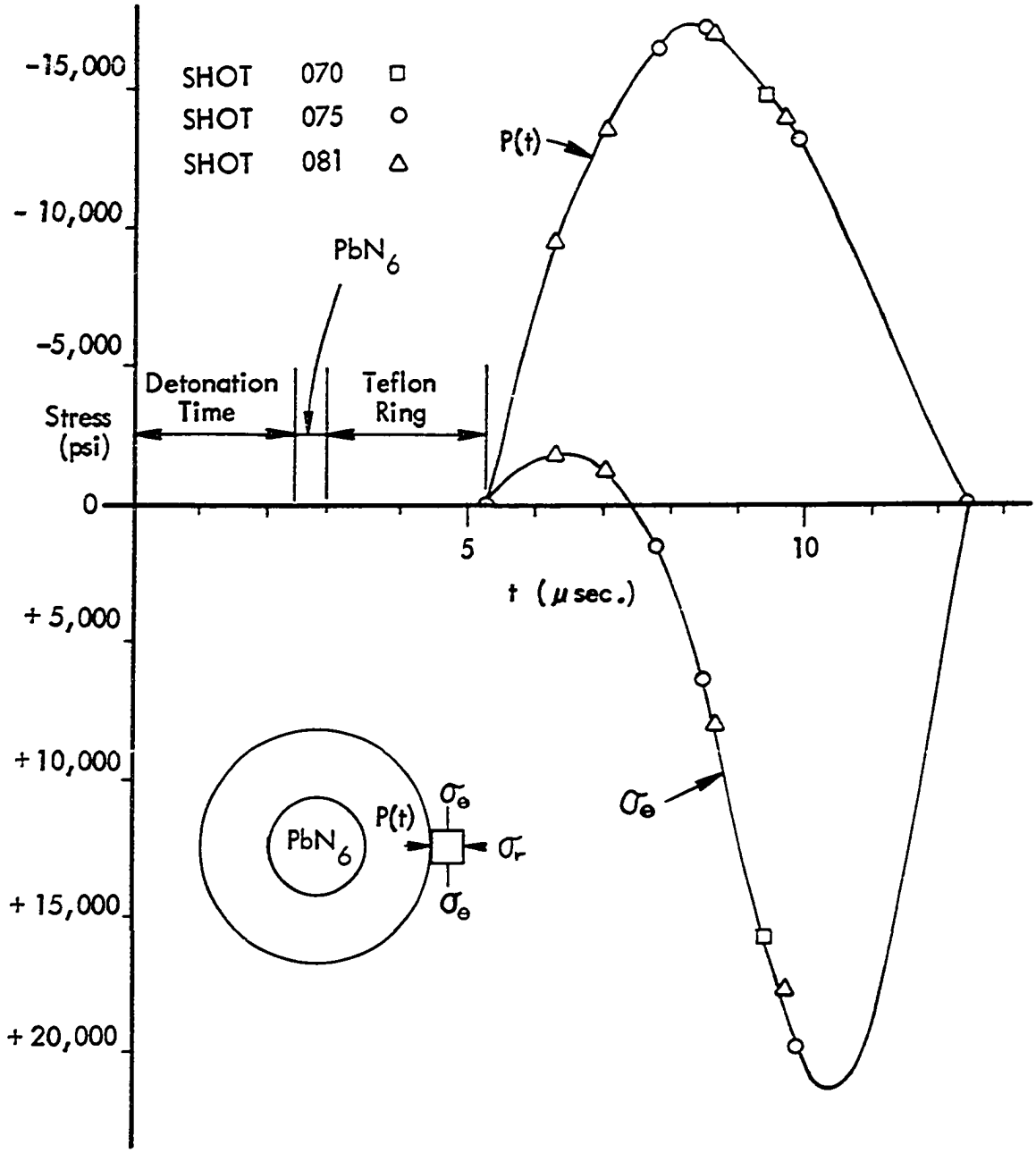

Figure 68. The input pressure pulse and tangential stress as a function of time at the Teflon-Plexiglas hole boundary

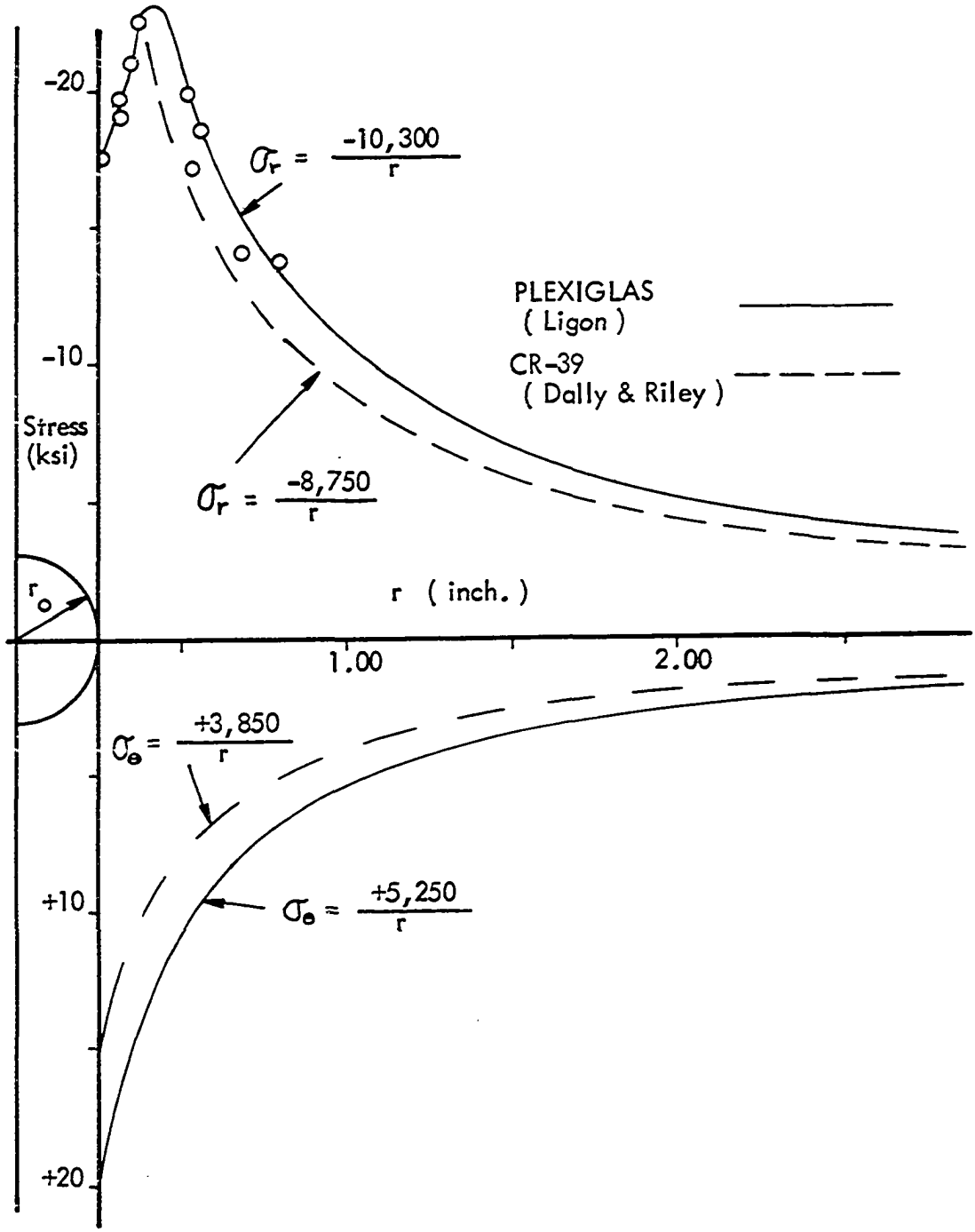

Figure 69. Radial and tangential stress formation and decay as a function of distance (shot 081)

DISCUSSION

In the initial stages of the calibration of the multiple spark camera, certain problems were encountered and resolved. It is this author's belief that they are of sufficient value to discuss in the next few paragraphs.

Multiple Spark Camera

Once the camera was built and tested, a number of instability and synchronization problems existed. Synchronization problems were encountered with the exploding wire detonation system when using the 2 KV source with a servo-operated contact switch which consisted of two 0.5 inch diameter brass spheres being brought together for circuit continuity. The electrical contact area of the two spheres was found to be too small to transmit the instantaneous surge of current necessary to explode the detonator within a few microseconds. Detonation delays of up to 200 microseconds were encountered before a manually operated, extra high voltage knife switch replaced the spherical contacts.

The instability problems were found to be caused by the susceptibility of the Model 547 Oscilloscope triggering system to any large electrical noise in the near vicinity. This was finally eliminated with careful shielding of all high voltage equipment.

The arcing wire worked 100 per cent in all shots.

Some difficulty was encountered initially with the heating wire. It was found that once the heating wire began to glow, the light sensor would prematurely trigger the oscilloscope when the wire reached a certain color. Once it heated beyond the frequency of this color, the oscilloscope could be rearmed. The glowing wire would not trigger it again until the wire voltage was decreased thus bringing the glowing wire back through the triggering color. This was eliminated by putting a physical stop on the heating wire voltage dial below that point in which the color was first produced that triggered the oscilloscope.

Later instability problems were traced to capacitor plate leakages. This was remedied, obviously, by replacing the capacitors.

Since the camera involves extremely large voltages and magnetic fields collapsing in close proximity to millivolt sensors, many of these problems were expected to some degree. Once the peculiarities of the system were observed and understood, the camera provided unfailing reliability and versatility throughout the testing sequence.

Once the data was recorded, analyzed, reduced, and plotted, a careful evaluation and discussion was made in order to enhance the validity of the results.

Explosive Pulse Sequence

The experimental results produced what is believed to be a good representation of the pulse shape as illustrated in Figure 68. This pulse is somewhat different from those previously estimated by earlier investigators. In Figure 70, an approximation of the pulse shape of a surface explosion from a semicircular cavity was presented by Dally and Thau (83). The shape of the pulse was based on the observation of the shape of the pressure wave, P_1, several inches into the model where dispersion and dissipation had well influenced the results. Dally and Thau made some

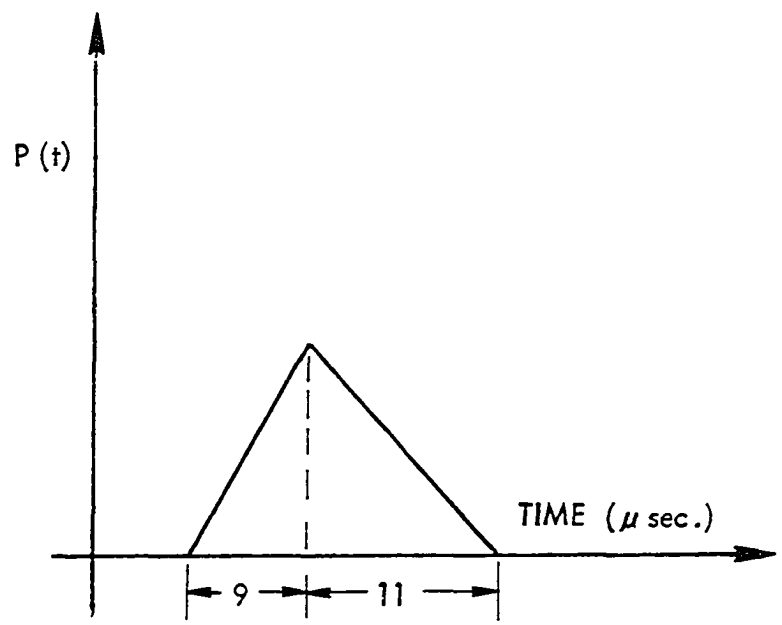

Figure 70. A surface explosion pulse shape approximated by Dally and Thau (83, page 297)

corrections for these results while readily admitting that the explosive would obviously not produce a ramp type of pulse. This shape was used as a matter of convenience for the theoretical solution. However, the duration of the rise and decay of the pulse was believed to be realistic.

In the current study, lead azide, with a burn rate of 192,000 in./sec. would be expected to have a burn time of approximately 0.5 microsecond for the 0.094 inch radius of the explosive cavity. The wave front would then take approximately 2.4 microseconds to transverse the Teflon ring (see Figure 68). This apparently lengthens the rise time to that of approximately 3 microseconds as indicated in Figure 68.

In the surface shot represented by Figure 70, the radius of the hole was 0.188 inch. This would produce an expected burn time of approximately 1 microsecond with no dissipation caused by any lining material. Therefore, it is difficult to visualize that the pulse would be any longer in duration than that calculated in this investigation.

Once σ_r was plotted as a function of r at different points in time (Figure 64), the observation was made that the maximum σ_r stress that was obtained during the propagation sequence in the material was up to 30 per cent higher than that applied to the boundary. This was attributed to the inertia effect of the material which was subjected to an extremely high loading rate ($\dot{\epsilon}_r$ = 94,000 in./in./sec.) for

a short length of time. The accelerated material continued to strain in compression for approximately 1.2 microseconds after the explosive had ceased to burn. Therefore, the peak σ_r stress occurred approximately 0.18 inches into the Plexiglas. From that point on, σ_r decayed as a function 10,300/r psi (Figure 69). This is in good agreement with some far field studies conducted by Dally and Riley (77) on CR-39. In their test, they were unable to obtain data any closer than 2 inches from the explosive nucleus. However, from that point on, the peak σ_r stress decayed as 8750/r psi. Although Dally and Riley's explosive charge caused the material to rupture, their decaying stress relation appeared to be in good agreement with the liner results since the ultimate strength of Plexiglas is 30 to 50 per cent greater than that of CR-39. Therefore, we would expect to have a larger stress input into the Plexiglas than that into the CR-39 before rupture.

Reproducibility

The reproducibility of an explosive charge in a birefringent material has been proven time and time again by investigators such as Dally, Riley, Durelli, and Daniels. Professor Dally's example of a doubly loaded half space (56) is a classic example of reproducibility. A test sequence which involved two separate explosives ignited several inches apart in the same model at the same instant

on one day was then repeated in the same manner on another model on a different day. The results were two negatives that became coincident when placed one upon the other at the same point in space. Because of the difficulty in producing a constant detonation interval from day to day, there was a 2 microsecond shift in time from when the waves in each photograph reached a certain position in space. This shift occurred in the detonation interval and not after the wave had entered the material from the explosive. In tests where the material fractures, the maximum fringe order is also highly repetitive. This will be discussed in the following section.

W. Goldsmith, et al. (129-130) utilized this repeatability in a wave sequence obtained by photographing the impact of a model at different time delays with a single frame camera.

In the liner series, the maximum fringe order was found to vary slightly (Figures 57 through 59) since fracture did not occur in any of the tests analyzed. Since the variance was only 3 per cent in the worst case, this was considered insignificant.

Fracture Criteria

By observing the type of fracture produced in the initial liner tests where the critical amount of PbN_6 was determined, some previously observed phenomena were able to

be explained. The fracture in the plexiglas appeared as a perfect crack running radially outward from the cavity and in a plane perpendicular to that of the thin plate. This indicated a failure criterion based on the maximum normal stress (Rankines) or maximum normal strain (Saint Venant) theories of failure. This is a type of failure typical of a brittle material. Therefore, Plexiglas, which is a ductile material under static conditions, behaves as a brittle material under extremely high loading rates experienced by its subjection to an explosive pulse.

Since the fracture crack was in a radial direction, failure was obviously produced by the tangential stress or strain reaching a maximum. In observing how σ_θ varied with time at the circular boundary (Figure 68) some insight into a phenomenon observed by previous investigators and this author was explained.

In previous tests that were conducted without liners, the maximum fringe order produced in a birefringent material remained constant when more than approximately 30 mg. of PbN_6 was used, i.e., no additional amplitude was achieved when larger quanitities of PbN_6 were detonated. The only evidence of the additional PbN_6 being used was a larger amount of destruction to the model. If the pattern established in Figure 68 is extended with increasing amounts of PbN_6, this phenomenon is explained (Figure 71).

Consider the case of the liner filled with a given

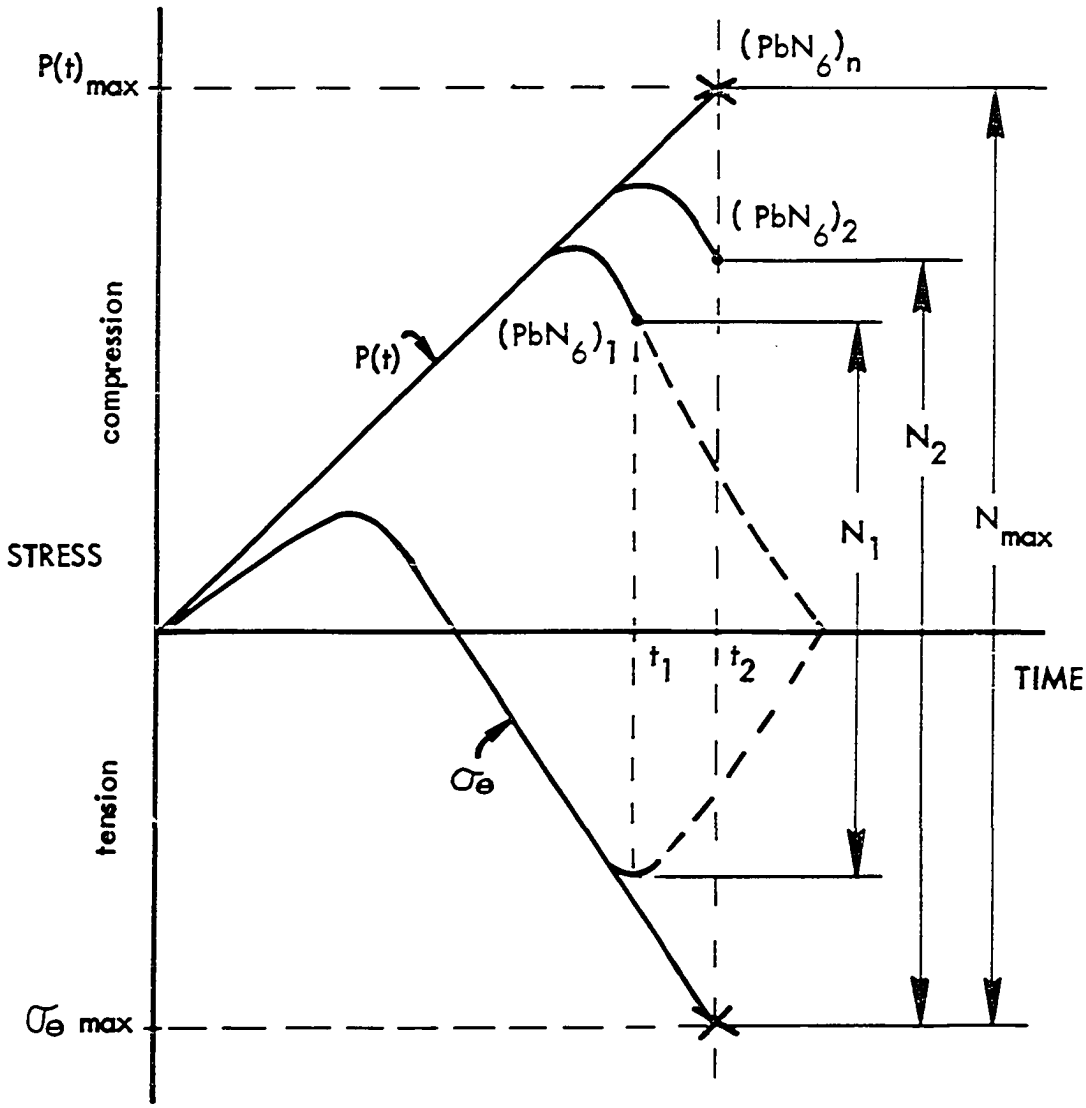

Figure 71. The effect of increasing the quantity of lead azide on the maximum birefringence developed

amount of lead azide designated as $(PbN_6)_1$. With this charge, σ_θ does not reach fracture before the $(PbN_6)_1$ is spent as the fringe order, N_1, peaks at t_1. However, if the charge is increased to $(PbN_6)_2$, the loading pressure P(t) is on the decay when σ_θ reaches fracture and the fringe order N_2 is a maximum at the time t_2. If the charge is again increased to the point that σ_θ reaches fracture before the pressure peaks, then a limiting fringe order is obtained. Any increase in lead azide (PbN_6) would simply be dissipated in destroying and burning material and not in producing additional stress. This then would explain the highly repetitive nature of the fringe magnitude for previous work where the liner was not used.

When the fracture stress of the birefringent material is reached in a Teflon lined hole, the principal stresses become nonsymmetric with the introduction of distortional waves caused by the rapidly relieved tangential stresses associated with fracture. However, the propagating isochromatics are influenced only when the difference in the principal stresses becomes nonsymmetrical as shown near the hole boundary in Frame 11, Figure 54. Since this does not occur instantaneously, the initial and decaying portion of the isochromatic pattern remains unaffected by the fracture as illustrated by Frames 12, 15, and 16 in Figure 54.

It should be recalled that the primary objective of this investigation was to obtain some insight into the actual manifestation of an explosive pulse. This information would be used to obtain some valid representation of the explosive loading function in order to have a realistic pulse shape to be utilized with theoretical consideration in wave mechanics problems. Therefore, the following sections are included as a general discussion to support the validity of the experimental data obtained in the current study.

Validity of Material Fringe Coefficient

Once the fringe order as a function of position was obtained, this information was used in conjunction with the dynamic material constants to determine the magnitude of the individual stresses σ_r and σ_θ. The fact that the material fringe coefficient for plexiglas was obtained by extrapolating data on a semi-logarithmic plot over several cycles of time may introduce significant error in the stress magnitudes. However, it should be recalled that the main objective was the determination of the pulse shape. Therefore, if desired, the stresses obtained from the dynamic optical coefficient could be normalized and give the same pulse shape information. However, after observing that the elastic modulus and material fringe coefficient of Plexiglas varied with time in the same manner that these parameters change in the tests conducted by Clark on CR-39, the

coefficient was felt to be realistic. In addition, the stress magnitudes seem to be in line with those values expected from information obtained from published works of previous investigators as indicated in the following paragraph.

In comparing the results obtained in the liner series near the cavity boundary with those obtained by Dally and Riley (77) several inches into the model, the pulse magnitudes were found to decay in a similar manner, i.e., inversely proportional to r. However, the initial build up of the σ_r stresses after a short distance of propagation into the model boundary could not possibly have been anticipated from the results of Dally and Riley since inherent synchronization delay, density of fringes, and lack of adequate smoke shielding prevented stress evaluation closer than two inches from the explosive source.

Validity of Stress-Strain Relations at High Loading Rates

In a series of tests conducted by Dally and Riley on various birefringent materials which were subjected to different constant loading rates (53), the modulus of elasticity as well as the fracture stresses were shown to increase with increased loading rates. However, at any given strain rate, the slope of the stress-strain curve was linear. This information was supplemented by tests conducted by Clark (132) on CR-39 and Dally and Riley on Plexiglas (54) which verified

that the dynamic modulus is much greater than that of the static modulus under explosive loading conditions. Kuske (143) found that the multiphase theory of plastics approximately explained the higher values for the elastic modulus under dynamic conditions.

In the stress separation procedure used in the previous chapter, the dynamic modulus calculated from plate and rod velocities, was used as a constant in determining stresses. This was also based on the theory that the density remains constant as the wave moves through the material. However, at very high stress levels, such as those achieved at the Teflon and Plexiglas interface, it is conceivable that the stress-strain curve may become concave upward and thus steeper at the higher stress levels. This type of consideration is discussed by Skidmore (144). This would indicate that the stress could have been slightly higher than that calculated in the previous chapter.

Validity of the Uniform Plane Stress Assumption

In two dimensional dynamic photoelasticity, the fringe order represents the average of the difference in principal stresses through the thickness of the model at a particular point. Therefore, judgement must be made by the investigator as to how thick a model can be before this assumption is no longer valid. The cylindrical shaped PbN_6 charge was assumed

to have burned radially outward from its nucleus. This would produce a uniform pressure over the entire cavity at the same instant in time. The rapid burning rate of PbN_6 combined with the smoothing action of the Teflon liner was found to have had sufficient flexibility to produce a uniform pressure on the cavity as indicated by the perfect symmetry of the fringes (Figures 52 and 53). Therefore the thickness of 0.235 inches would not be of sufficient magnitude to invalidate the uniform stress assumption.

A second consideration was that of the validity of the generalized plane stress assumption. For generalized plane stress, effects of internal dissipation as well as dispersive effects from the actual three dimensional geometry, are neglected in mathematical models. Dispersion is manifested in the dynamic loading of materials since the harmonic components of the waves will propagate at velocities which depend on their frequencies. This occurs in plates from the interaction of the waves with the front and back surfaces of the plate. While both dispersion and dissipation increases the decaying phenomenon of the stress magnitudes, dispersion causes the base of the pulse to broaden as it propagates. According to Mindlin (145), the generalized plane stress approximation becomes accurate when the wave length (λ) $>>$ π x plate thickness (h). Since the compressive extension wave length in the current study was equal to the thickness of the model in the immediate

vicinity of the circular cavity, the wave initially induced was dispersive. Therefore, the predominate discrepancy that can be expected in utilizing the experimentally determined pulse in a generalized plane stress mathematical model, should be attributed primarily to dispersion and internal dissipation.

Once the wave propagated several inches into the material, the base of the wave broadened by dispersion to the extent that it was significantly larger than 0.75 inches; thus, the dispersive effects became negligible. This was verified by Dally and Thau in fairly good theoretical and experimental comparison in far field studies (12), (83).

RECOMMENDATIONS FOR FUTURE WORK

Although dynamic photoelastic wave propagation is not a new field, extensive work still remains for the interested investigator. Of the many facets of experimental wave mechanics that can be pursued in future work, only those of direct relationship to this study will be considered.

Multiple Spark Camera

Throughout the construction and the many months of utilizing the spark camera in hundreds of test shots, several possibilities for improvement were recorded to be presented for the benefit of future investigators.

Polarized field

As mentioned before, one drawback to the present multiple spark camera is that the light passes through the model at an oblique angle. By introducing another field lens of the same specifications into the system, this situation could be improved. The model would be placed between the two lenses and the light could be directed through the model at a smaller angle. Bradley and Kobayashi utilized this design in a multiple spark camera they constructed for crack propagation studies (146).

Post suggested an interesting modification to the system which would also alleviate the problem of the polarized field not being perpendicular to the model. If the

spark array were mounted on the inside wall of a cylindrical drum, the light from the gaps could be directed toward the model by use of a multiple sided prism or system of mirrors mounted in the core of the drum. After passing through the model, the light rays could be directed to a similarly mounted lens array by means of another multiple sided prism. Since the illumination of the model by each spark gap would originate from essentially the same point, the multiple sided prism, the model could easily be oriented so that it is orthogonal to the polarized field.

Intensity control

Since each gap of the spark array did not always generate the same intensity of light, variation in the density of the negative from frame to frame was often experienced. Since the lenses of the array do not gather light in the same manner as a conventional lens, reducing the diameter of the diaphragm serves only to reduce the photographic field and not the intensity of the light reaching the film plane. Previous investigators observed that uniform intensity for each frame could be achieved by varying the diameters of the brass spheres from gap location to gap location. By trial and error, the correct combination of brass spheres would yield a series of sparks of consistent intensity. The author found the balancing of intensity among frames could be done in an easier and less expensive fashion

by using dark room techniques. However, this has some drawbacks; namely, lack of simplicity for a person who is not proficient in dark room techniques.

The problem could be eliminated, easily, by installing a polaroid filter in a rotating mount directly on each lens in the array. By rotating the polaroid, varying degrees of light extinction could be achieved. Therefore, each individual lens could have its light input adjusted until a uniform intensity was achieved on the film plane.

Frame rate control

Some time was spent in the initial stages of the construction of the camera considering the feasibility of installing inductors with variable cores for a continuous selection of framing rates. Although a suitable core material was not found, the idea appears to be feasible. Since this would give the photographic system sub-microsecond control, which has been found to be desirable, reevaluation of the concept is in order.

Synchronization

Because of the sensitivity of the internal triggering mechanism of the Tektronix 547 Oscilloscope to high voltages in the vicinity of the camera, another oscilloscope model might have been more suitable for this particular photographic system. Because of the many "dry firings" of the camera

that are necessary to calibrate a particular combination of spark delays, storage capabilities of an oscilloscope would be a desirable feature from the point of view of convenience and economy.

Although all of these features in one oscilloscope would probably exclude the built in delay capabilities of the Model 547, a separate delaying generator could be added to the system to accomplish this task.

Time sequence gapping

Inherent gapping in time in the intervals between frames was observed when certain combinations of inductors were utilized in a particular sequence. As mentioned before, this was attributed to an interaction of induced voltages in the inductors which was caused by the large magnitudes of the magnetic fields which were collapsing in the inductor cabinet at different times. One possible solution to this would be to isolate each inductor in a separate shielded container thus minimizing induced voltage interaction between adjacent inductors.

All of the above mentioned improvements for future consideration should increase the flexibility of the camera without reducing the effectiveness of the present system. Since they are specialty items, a particular investigator would have to justify their adoption after a careful investigation.

Explosive Pulse Sequence

The ultimate goal of this phase of the study was to experimentally obtain some insight into the shape of an explosive pressure pulse at the loaded circular boundary in order to assist in the mathematical modeling of complicated problems in wave mechanics. While considerable progress was made toward the solution of this difficult problem, a significant amount of work remains to be done before the phenomenon occurring in the region near the loaded boundary is completely understood. This and future mathematical comparisons will be discussed in the following paragraphs.

Model materials

Although Plexiglas provided an optically suitable material for close field consideration, the photographic system was capable of resolving fringe densities greater than those experienced in Plexiglas. Therefore, for future work in close field studies there is still a need for a temporarily birefringent material that has an optical sensitivity greater than Plexiglas but less than CR-39 and exhibits all of the desirable properties established earlier for model materials.

Since it would be extremely expensive to have a birefringent material developed especially for a particular photoelastic use, photoelasticians have to rely on commercially

available plastics and resins, developed for consumer products, for their model materials. Therefore, locating a material with the desired optical and mechanical properties can be an endless process of testing numerous polymers as they are introduced to the market. One such material, Zelux, which is commercially available from Westlake Plastics Company, was investigated to some extent in the latter stages of the current study. Zelux is a transparent optical grade polycarbonate that is extremely resistant to fracture. In fact, a 200 mg. charge of lead azide detonated in a 0.25 inch diameter cavity in a sheet of Zelux produced only a small amount of plastic deformation in the material with no apparent fracture. This material would appear to be ideally suited for the current investigation since the explosive could be detonated in an unlined charge cavity without fracture. However, because of this characteristic, extremely high stresses were created in the vicinity of the circular cavity since the material accepted the excessive amount of energy that is normally dissipated in fracturing and accelerating small pieces of the model. This, coupled with the high optical sensitivity of the material, produced a fringe density that was not resolvable until the wave had propagated over 18 inches from the charge cavity. This excluded the use of the material as a model for close field studies with the spark camera; however, in far field observations, the Zelux

exhibited birefringence for a much greater distance from the explosion than CR-39 with an equivalent charge of lead azide. This was expected in light of the high optical sensitivity of the Zelux as well as the large initial stresses that were produced in the model because of the lack of dissipation by fracture.

Although not suited for models in future close field studies, Zelux should be considered as a possible liner material because of its apparent resistance to fracture.

Dispersion effects

For the generalized plane stress problem, more work should be done in evaluating effects normally attributed to dispersion. This could be accomplished by detonating an explosive in plates of different thicknesses and comparing the results.

The case in which the plate thickness is large, with respect to other dimensions can be investigated by utilizing the embedded polariscope technique for three dimensional photoelasticity. The embedded polariscope is constructed of two oriented polaroids bonded to each side of a thin sheet of birefringent material. The resulting laminated sheet is then sandwiched and bonded between two large slabs of the same birefringent material. When appropriately loaded, the birefringence in the material that is separating the polaroids is photographically recorded. This is repre-

sentative of the case of generalized plane strain in the plane that is experiencing birefringence. Since the propagating waves can be analyzed before interacting with the front and back surfaces of the slab, dispersion is eliminated.

Intermediate field

As previously stated, a representation of the dynamic stress situation in the close field region near the charge hole boundary was established from the results of the current study. From work conducted by Riley, Dally, and Thau, the dynamic stress situation in the far field region has been extensively investigated. However, the intermediate field, which is the transition region between near and far fields, there is a need for further experimental investigation. In order to pursue this, more data is needed on the decaying side of the initial P_1 wave, Figure 60. Since submicrosecond control is presently beyond the capabilities of the spark camera, a large number of shots would have to be made until a sufficient amount of the desired data points were obtained from various random framing rate sequences. Additional information could be obtained in the intermediate field with the introduction of new birefringent materials or the modification of the circuitry of the system to allow for submicrosecond control. Both of these possibilities have been discussed in previous sections.

Close field

With the establishment of the pulse shape, possible future work will involve comparisons with numerical solutions such as TOODY II as well as close field mathematical modeling such as that outlined by Selberg. Of immediate interest in the near future is the inversion of Equation 46, page 110, once a suitable mathematical expression is obtained for the pulse shape and substituted into the equation for P(t).

Material properties

Work should be continued with further investigations on how the various optical and mechanical properties of temporarily birefringent materials behave at extremely high loading rates.

Although the properties of CR-39 are well established, Plexiglas and new materials such as Zelux must be investigated at greater lengths before these materials become widely used in wave propagation studies.

SUMMARY AND CONCLUSIONS

A versatile dynamic photoelasticity laboratory was established. The major component of the laboratory, an ultra high speed multiple spark camera was constructed and found to be very reliable for use in evaluating complex wave mechanics problems in solids. Several of the preceding chapters and the Appendices were written in such a manner that this manuscript may be readily used as a complete reference and service manual for the multiple spark photographic system. Several new synchronization systems and smoke shielding allowed for the recording of close field information never before achieved. Although the photographic system functioned flawlessly, once perfected, several suggestions for future improvements in its flexibility were discussed.

An extensive investigation into the use of colored photography with the spark camera was highly successful and provided information on fringe magnitudes not previously available from black and white photographs.

A simple, reliable, and rapid means of nondestructively measuring plane wave speeds in any material that can be shaped into a bar or rod was developed using a quartz load cell as a sensor.

The dynamic stress situation in a region close to an explosive pulse propagating from a circular cavity in a thin

plate was optically investigated revealing the manner in which the pulse was formed. The investigation indicated that the pulse was not fully formed until it had propagated into the boundary for approximately 0.2 inches reaching magnitudes up to 30 per cent more than its original boundary loading value. The loading function P(t) on the boundary was found to reach a magnitude of 17,500 psi with a rise time of approximately 3 microseconds and a decay time from 3.5 to 4.2 microseconds. The tangential component of stress, σ_θ, on the boundary was found to go initially into compression (for about 2.2 microseconds) and then rapidly extend in tension. The behavior of the σ_θ stress explained the frequently observed phenomenon that there is an upper limit to the number of isochromatics that a given birefringent material will exhibit before fracturing in tension under an explosive load.

A numerical computer solution (TOODY II) was employed to obtain a theoretical pulse shape for comparison with that resolved from the experimental approach. However, because of a lack of funds, this work had to be terminated before the entire pulse shape was obtained.

A theoretical plane strain approach that is applicable to the current problem was obtained from literature. Since the numerical results for the solution relied on the inversion of a Laplace transform, once a loading function P(t) was established, this too was left for future work.

BIBLIOGRAPHY

1. Brewster, D. On the communication of the structure of doubly refracting crystals to glass, muriate of soda, flour spar, and other substances by mechanical compression and dilation. Philosophical Transactions of the Royal Society 1816: 156-178. 1816.

2. Neumann, F. E. Über die gesetze der doppelbrechung des lichtes in comprimierten und ungleichformig erwarmten unkrystallinischen korpern. Abhandlungen der Koniglichen Akademie der Wissenschaften zu Berlin, Part II: 1-254. 1841.

3. Maxwell, J. C. On the equilibrium of elastic solids. Transactions of the Royal Society of Edinburgh 20, Part I: 87-120. 1853.

4. Coker, E. G. and Filon, L. N. G. A treatise on photoelasticity. Cambridge, University Press. 1931.

5. Frocht, Max Mark. Photoelasticity, Volume I. New York, N. Y., John Wiley and Sons, Inc. 1941.

6. Frocht, Max Mark. Photoelasticity, Volume II. New York, N. Y., John Wiley and Sons, Inc. 1948.

7. Dally, James W. and Riley, William F. Experimental stress analysis. New York, N. Y., McGraw-Hill Book Co., Inc. 1965.

8. Durelli, A. J. and Riley, W. F. Introduction to photomechanics. Englewood Cliffs, N. J., Prentice-Hall, Inc. 1965.

9. Jessop, H. T. and Harris, F. C. Photoelasticity. New York, N. Y., Dover Publications, Inc. 1950.

10. Heywood, R. B. Designing by photoelasticity. London, Chapman and Hall, Ltd. 1952.

11. Frocht, M. M. Studies in dynamic photoelasticity with special emphasis on the stress-optic law. In Davids, Norman, ed. International symposium of stress wave propagation in materials. pp. 91-117. New York, N. Y., Interscience Publishers, Inc. 1960.

12. Thau, S. A. and Dally, J. W. Subsurface characteristics of the Rayleigh wave. International Journal of Engineering Science 7: 37-52. 1969.

13. Konig, W. Doppelbrechung in transversal schwingenden glasplatten. Ann. Phys., Leipzig 4: 1-40. 1901.

14. Tuzi, Z. Photographic and kinematographic study of photoelasticity. Journal for the Society of Mechanical Engineers 31, No. 136: 334-339. 1928.

15. Frocht, M. M. Kinematography in photoelasticity. Transactions of the American Society of Mechanical Engineers 54, Part 1: 83-96. 1932.

16. Tuzi, Z. and Nisida, M. Photoelastic study of stresses due to impact. Philosophical Magazine Ser. 7, 21: 448-473. 1936.

17. Senior, D. A. and Wells, A. A. A photoelastic study of stress waves. Philosophical Magazine Ser. 7, 37: 463-469. 1946.

18. Foeppl, L. Slow motion pictures of impact tests by means of photoelasticity. Journal of Applied Mechanics 71: 173-177. 1949.

19. Christie, D. G. Reflection of elastic waves from a free boundary. Philosophical Magazine Ser. 7, 46: 527-541. 1955.

20. Christie, D. G. A multiple spark camera for dynamic stress analysis. Journal of Photographic Science 1, No. 5: 153-159. 1955.

21. Cranz, C. and Schardin, H. Kinematographic auf rukendem film und mit extrem hoher bildfrequenz. Zeitschrift fur Physik 56: 147-183. 1929.

22. Schardin, H. Application of spark-cinematography for the study of failure processes. In Naslin, P. and Vivie, J., eds. Photographie et Cinematographie Ultrarapides. pp. 301-314. Paris, Dunod. 1956.

23. Perkins, H. C. Movies of stress waves in photoelastic rubber. Journal of Applied Mechanics 20, No. 1: 140-141. 1953.

24. Courtney-Pratt, J. S. High speed photography and micorgraphy. Applied Optics 3, No. 11: 1201-1208. 1964.

25. Schwieger, H. Photoelastic study of the impact of thin glass rods. In Naslin, P. and Vivie, J., eds. Photographic et Cinematographie Ultrarapides. pp. 345-351. Paris, Dunod. 1956.

26. Frocht, M. M. and Flynn, P. D. Studies in dynamic photoelasticity. Journal of Applied Mechanics 23: 116-122. 1956.

27. Betser, A. A. and Frocht, M. M. A photoelastic study of maximum tensile stresses in simply supported short beams under central transverse impact. Journal of Applied Mechanics 24: 509-514. 1957.

28. Flynn, P. D. and Frocht, M. M. On the photoelastic separation of principal stresses by oblique incidence. Journal of Applied Mechanics 28: 144-145. 1961.

29. Flynn, P. D. and Froch, M. M. On Saint Venant's principle under dynamic conditions. Proceedings of the Society for Experimental Stress Analysis 18, No. 1: 16-20. 1961.

30. Wells, A. A. and Post, D. The dynamic stress distribution surrounding a running crack - a photoelastic analysis. Proceedings of the Society for Experimental Stress Analysis 14, No. 1: 69-96. 1957.

31. Christie, D. G. An investigation of cracks and stress waves in glass and plastics by high-speed photography. Journal of the Society of Glass Technology 36: 74-89. 1952.

32. Riley, W. F. and Durelli, A. J. Stress distribution on the boundary of a circular hole in a large plate during passage of a stress pulse of short duration. Journal of Mechanical Engineering Science 3, No. 1: 62-68. 1961.

33. Durelli, A. J. and Riley, W. F. Experiments for the determination of transient stress and strain distributions in two-dimensional problems. Journal of Applied Mechanics 24: 69-76. 1957.

34. Durelli, A. J., Dally, J. W. and Riley, W. F. Developments in the application of the grid method to dynamic problems. Journal of Applied Mechanics 26, No. 4: 629-634. 1959.

35. Dally, J. W., Riley, W. F. and Durelli, A. J. A photoelastic approach to transient stress problems employing low-modulus materials. Journal of Applied Mechanics 26, No. 4: 613-620. 1959.

36. Durelli, A. J. and Dally, J. W. Stress concentration factors under dynamic loading conditions. Journal of Mechanical Engineering Science 1, No. 1: 1-5. 1959.

37. Dally, J. W., Durelli, A. J. and Riley, W. F. Photoelastic study of stress wave propagation in large plates. Proceedings of the Society for Experimental Stress Analysis 17: 33-50. 1960.

38. Riley, W. F. and Durelli, A. J. Application of Moire methods to the determination of transient stress distributions. Journal of Applied Mechanics 29, No. 1: 23-29. 1962.

39. Daniel, I. M. and Riley, W. F. Stress distribution on the boundary of a circular hole in a large plate due to an air shock wave traveling along an edge of the plate. Journal of Applied Mechanics 31, No. 3: 402-408. 1964.

40. Flynn, P. D., Feder, J. C., Gilbert, J. T. and Roll, A. A. Some new techniques for dynamic photoelasticity. Experimental Mechanics 2: 159-160. 1962.

41. Flynn, P. D., Gilbert, J. T. and Roll, A. A. Some recent developments in dynamic photoelasticity. Society of Photographic Instrumentation Engineers Journal 2: 128-131. 1964.

42. Flynn, P. D., Feder, J. C., Gilbert, J. T. and Roll, A. A. Stress waves due to explosive and mechanical loading of low modulus photoelastic materials. Frankford Arsenal (Philadelphia, Pa.) Report No. A 62-4. 1962.

43. Flynn, P. D., Gilbert, J. T. and Roll, A. A. Photoelastic studies of dynamic stresses in low modulus materials. Frankford Arsenal (Philadelphia, Pa.) Report No. A 62-18. 1962.

44. Flynn, P. D., Feder, J. C., Gilbert, J. T. and Roll, A. A. Impact stresses in low modulus photoelastic materials. In Proceedings of the International Symposium on Photoelasticity. pp. 265-275. New York, N. Y., Pergamon Press. 1963.

45. Flynn, Paul D. Recent advances in dynamic photoelasticity. Frankford Arsenal (Philadelphia, Pa.) Report No. A 64-30. 1964.

46. Flynn, P. D. A dual-beam polariscope for oblique incidence. Experimental Mechanics 4, No. 6: 182-184. 1964.

47. Flynn, P. D. Dynamic photoelasticity using a dual-beam polariscope and ultra-high-speed photography. Proceedings of the Seventh International Congress on High-Speed Photography, Zurich. pp. 351-357. Darmstadt, Germany, Helwich Verlag. 1967.

48. Flynn, Paul D. Dynamic photoelasticity. Instrument Society of America 5, No. 1: 65-72. 1966.

49. Flynn, Paul D. Dynamic photoelastic stress patterns from a simplified model of a head. In Caveness, William and Walker, Earl, eds. Head Injury Conference Proceedings. pp. 344-349. Philadelphia, Pa., J. B. Lippincott Co. 1966.

50. Flynn, Paul D. Photoelastic studies of dynamic stresses in high modulus materials. Journal of the Society of Motion Picture and Television Engineers 75, No. 8: 729-734. 1966.

51. Flynn, Paul David. Studies in dynamic photoelasticity. Unpublished Ph.D. thesis. Chicago, Illinois, Library, Illinois Institute of Technology, 1954.

52. Feder, J. C., Gibbons, R. A., Gilbert, J. T. and Offenbacher, E. L. The study of the propagation of stress waves by photoelasticity. Proceedings of the Society for Experimental Stress Analysis 14, No. 1: 109-118. 1956.

53. Dally, J. W. and Riley, W. F. Photoelastic study of wave propagation. (IIT Research Institute Technology Center, Chicago) Air Force Weapons Laboratory Contract No. AF 29(601)-6696 Project 5710. 1965.

54. Dally, J. W. and Riley, W. F. Photoelastic study of wave propagation. (IIT Research Institute Technology Center, Chicago) Air Force Weapons Laboratory Technical Report No. AFWL-TR-66-54. 1966.

55. Riley, W. F. and Dally, J. W. A photoelastic analysis of stress wave propagation in a layered model. Geophysics 31, No. 5: 881-899. 1966.

56. Dally, J. W. A dynamic photoelastic study of a doubly loaded half-plane. Proceedings of the Midwestern Mechanics Conference 10: 649-664. 1967.

57. Dally, J. W. and Riley, W. F. Initial studies in three-dimensional dynamic photoelasticity. Journal of Applied Mechanics 34: 405-410. 1967.

58. Dally, J. W. and Lewis, David, III. A photoelastic analysis of propagation of Rayleigh waves past a step change in elevation. Bulletin of the Seismological Society of America 58, No. 2: 539-563. 1968.

59. Dally, J. W. and Brillhart, L. V. Application of the multiple-spark-gap camera to dynamic photoelasticity. Journal of the Society of Motion Picture and Television Engineers 77: 116-120. 1968.

60. Riley, W. F. and Dally, J. W. Recording dynamic fringe patterns with a Cranz-Schardin camera. Journal of the Society for Experimental Stress Analysis 9, No. 8: 27N-33N. 1969.

61. Marino, R. L. and Dally, J. W. Rayleigh wave propagation along curved boundaries. Proceedings of the 11th Midwestern Mechanics Conference 5: 819-831. 1969.

62. Daniel, I. M. Photoelastic study of wave propagation in layered media. (IITRI Research Institute Technology Center, Chicago) Air Force Weapons Laboratory IITRI Research Project No. D6038. 1968.

63. Daniel, I. M. Experimental methods for dynamic stress analysis in visco-elastic materials. Journal of Applied Mechanics 32, No. 3: 598-606. 1965.

64. Daniel, I. M. Dynamic properties of a photoviscoelastic material. In Proceedings of the international congress for experimental mechanics. pp. 183-192. Westport, Conn., Society for Experimental Stress Analysis. 1966.

65. Daniel, I. M. Interaction of a plane stress wave and a cylindrical cavity in a viscoelastic medium. Presented at the U. S. National Congress on Applied Mechanics, Minneapolis. New York, N. Y., American Society of Mechanical Engineers. 1966.

66. Daniel, Issac M. Static and dynamic stress analysis in viscoelastic materials. Unpublished Ph.D. thesis. Chicago, Illinois, Library, Illinois Institute of Technology. 1964.

67. Mindlin, R. D. A mathematical theory of photoviscoelasticity. Journal of Applied Physics 20: 206-216. 1949.

68. Daniel I. M. Experimental study of stress wave interaction in photoviscoelastic plates. Kirtland Air Force Base, New Mexico, Air Force Weapons Command Report No. AFWL-TR-65-43. January, 1966.

69. Ferguson, C. W. Analysis of stress-wave propagation by photoviscoelastic techniques. Journal of the Society of Motion Picture and Television Engineers 73, No. 9: 782-787. 1964.

70. Brown, G. W. and Selway, D. R. Frequency response of a photoviscoelastic material. Society for Experimental Stress Analysis 21, No. 1: 57-63. 1964.

71. Taylor, C. E. Applications of lasers to photoelasticity. Urbana, Illinois, University of Illinois, T and AM Report No. 276. 1965.

72. Taylor, C. E., Bowman, C. E., North, W. P. and Swinson, W. F. Applications of lasers to photoelasticity. Society for Experimental Stress Analysis 23, No. 1: 289-296. 1966.

73. North, W. P. T. and Taylor, C. E. Dynamic-stress concentration using photoelasticity and a laser light source. Proceedings of the Society for Experimental Stress Analysis 23, No. 2: 337-341. 1966.

74. Rowlands, R. E., Taylor, C. E. and Daniel, I. M. Multiple pulsed ruby laser system for dynamic photomechanics; applications to transmitted and scattered light photoelasticity. Experimental Mechanics 9, No. 9. 385-389. 1969.

75. Rowlands, R. E. A sequentially modulated ruby laser system for transmitted and scattered light dynamic photoelasticity. Urbana, Illinois, University of Illinois, T and AM Report No. 304. 1967.

76. Rowlands, R. E., Taylor, C. E. and Daniel, I. M. Ultra-high speed framing photography employing a multiple pulsed ruby laser and a smear type camera; application to dynamic photoelasticity. Presented at the 8th International Congress on High Speed Photography, Stockholm. New York, N. Y., John Wiley and Sons, Inc. 1968.

77. Dally, J. W. and Riley, W. F. Stress wave propagation in a half plane due to a transient point load. In Developments in theoretical and applied mechanics, Vol. 3. pp. 357-377. New York, N. Y., Pergamon Press. 1967.

78. Dally, James W. Data analysis in dynamic photoelasticity. Experimental Mechanics 7, No. 8: 332-338. 1967.

79. Goldsmith, W. Dynamic photoelasticity. In Worley, W. J., ed. Experimental techniques in shock and vibration. pp. 25-54. New York, N. Y., American Society of Mechanical Engineers. 1962.

80. Hays, George E. A color Schlieren system for high-speed photography. Journal of the Society of Motion Picture and Television Engineers 66, No. 5: 355-360. 1957.

81. Frocht, M. M., Flynn, P. D. and Landsberg, D. Dynamic photoelasticity by means of streak photography. Proceedings of the Society for Experimental Stress Analysis 14, No. 2: 81-90. 1957.

82. Dally, J. W., Henzi, A. and Lewis, D. On the fidelity of high-speed photographic systems for dynamic photoelasticity. Experimental Mechanics 9, No. 9: 394-400. 1969.

83. Dally, J. W. and Thau, S. A. Observations of stress wave propagation in a half-plane with boundary loading. Int. J. Solids Structures 3: 293-308. 1967.

84. Ellis, A. T. and Fourney, M. E. Application of a ruby laser to high-speed photography. Proceedings of the Institute of Electrical and Electronic Engineers Correspondence 51: 942. 1963.

85. Walker, E. W. Kerr cell cine-camera. In Collins, R. B., ed. Proceedings of the 3rd International Congress on High Speed Photography. pp. 133-137. New York, N. Y., Academic Press. 1957.

86. Schenck, W. J. Kerr cells for ultra high-speed photography. Instrument Society of America Transactions 5, No. 1: 14-27. 1966.

87. Froome, K. D. An electronically operated kerr cell shutter. Photographic Journal 92B: 158-161. 1952.

88. Bagley, C. H. Trapping time with photography. Industrial Research 4: 15-23. 1962.

89. Williams, M. L., Jessey, M. E. and Parmerter, R. R. Some exploratory photoelastic studies in stress wave propagation. Proceedings of the Society for Experimental Stress Analysis 17, No. 2: 121-134. 1960.

90. Sutton, G. W. A photoelastic study of strain waves caused by cavitation. Journal of Applied Mechanics 24, No. 3: 340-348. 1956.

91. Miller, C. D. Half-million stationary images per second with refocused revolving beams. Journal of the Society of Motion Picture and Television Engineers 53, No. 11: 479-488. 1949.

92. Hayes, R. A. Design parameters of an image-dissection camera. Instrument Society of America Transactions 5, No. 1: 37-43. 1966.

93. Tuttle, F. High speed motion pictures by multiple-aperture focal-plane scanners (image dissection). Journal of the Society of Motion Picture and Television Engineers 53, No. 4: 451-461. 1949.

94. Sultanoff, M. A 100,000,000 frames per second camera. Journal of the Society of Motion Picture and Television Engineers 55, No. 8: 158-166. 1950.

95. Courtney-Pratt, J. S. Fast multiple frame photography. Journal of Photographic Science 1, No. 1: 21-40. 1953.

96. Reed, W. O. and Niklas, W. F. Shutter image converter tube for multiple frame photography. Journal of the Society of Motion Picture and Television Engineers 68, No. 1: 1-5. 1959.

97. Korpel, A., Adler, R., Desmares, P. and Smith, T. M. An ultrasonic light deflection system. Institute of Electrical and Electronics Engineers Journal of Quantum Electronics QE-1, No. 1. 1965.

98. Fowler, F. J., Buhrer, C. F., and Bloom, L. R. Electro-optic light beam deflectors. Institute of Electrical and Electronics Engineers Proceedings 52, No. 2: 193. 1964.

99. Chesterman, W. D. The photographic study of rapid events. Oxford, Clarendon Press. 1951.

100. Jones, G. A. High Speed Photography. New York, N. Y., John Wiley and Sons, Inc. 1952.

101. Bibliography on high-speed photography. Journal of the Society of Motion Picture and Television Engineers 56, No. 1: 93-111. 1951.

102. Courtney-Pratt, J. S. A review of the methods of high speed photography. Reports on Progress in Physics 20: 379-432. 1957.

103. Lunn, Goerge H. A general survey of high speed photographic techniques. Journal of the Society of Motion Picture and Television Engineers 71, No. 12: 915-920. 1962.

104. Coleman, K. R. Ultra high-speed photography. International Science and Technology: 40-44. January, 1964.

105. Brown, E. B. Modern optics. New York, N. Y., Reinhold Publishing Corporation. 1965.

106. Hyzer, W. G. Introduction to high-speed photographic instrumentation. Instrument Society of America Transactions 5, No. 1: 1-4. 1964.

107. Eisendrath, D. B. Some highlights of the early history of high speed photography. Presented at the 99th Technical Conference of the Society of Motion Picture and Television Engineers. New York, N. Y., Society of Motion Picture and Television Engineers. May, 1966.

108. Collines, R. B., ed. Proceedings of the Third International Congress on High-Speed Photography, 1956. London, Butterworth's Scientific Publications. 1957.

109. Holland, T. E., Healey, T. J. and Bagley, C. H. Ultra-high speed photographic instruments. Instrument Society of America Transactions 5, No. 1: 5-13. 1966.

110. Edgerton, H. E. and Killian, J. R. Flash seeing the unseen by ultra high-speed photography. Boston, Hale, Cushman and Flint. 1939.

111. Fayolle, P. and Naslin, P. Simple electronic devices for high-speed photography and cinematography. Journal of the Society of Motion Picture and Television Engineers 60, No. 4: 603-612. 1953.

112. Miklowitz, Julius. Recent developments in elastic wave propagation. Applied Mechanics Reviews 13, No. 12: 865-877. 1960.

113. Miklowitz, Julius. Elastic wave propagation In Abramson, H. Norman, ed. Applied Mechanics Surveys. pp. 809-839. Washington, Spartan Books. 1966.

114. Kolsky, H. Experimental wave-propagation in solids. New York, N. Y., Pergamon Press. 1960.

115. Kolsky, H. Stress waves in solids. New York, N. Y., Dover Publications, Inc. 1963.

116. Ewing, W. Maurice and Jardetzky, Wenceslas S. and Press, Frank. Elastic waves in layered media. New York, N. Y., McGraw-Hill Book Co., Inc. 1957.

117. Cagniard, L., Flinn, Edward A. and Dix, C. Hewitt. Reflection and refraction of progressive seismic waves. New York, N. Y., McGraw-Hill Book Co., Inc. 1962.

118. Davies, R. M. Stress waves in solids. British Journal of Applied Physics 7: 203-209. 1956.

119. Davies, R. M. Stress waves in solids. In Batchelor, G. K. and Davies, R. M., eds. Surveys in mechanics; 70th anniversary volume. pp. 64-138. London, Cambridge University Press. 1956.

120. Dally, J. W., Riley, W. F., and Brillhart, L. V. Literature survey of stress waves in solids subjected to dynamic point source loading. (IIT Research Institute Technology Center, Chicago, Illinois) IITRI Project No. M 6097 Interim Report. April, 1965.

121. Sezawa, K. Dilatational and distortional waves generated from a cylindrical or a spherical origin. Bulletin of the Earthquake Research Institute 2, Tokyo University: 13. March, 1927.

122. Kromm, A. Zur ausbreitung von stosswellen in kreislochscheiben. Zeitschrift fur angewandte Mathematik und Mechanik 28: 297-303. 1948.

123. Goodier, J. N. and Jahsman, W. E. Propagation of a sudden rotary disturbance in an elastic plate in plane stress. Journal of Applied Mechanics 23, No. 2: 284-286. 1956.

124. Miklowitz, J. Plane-stress unloading waves emanating from a suddenly punched hole in a stretched elastic plate. Journal of Applied Mechanics 27: 165-171. 1960.

125. Forrestal, J. J. An approximate solution for the circumferential stresses in a stretched plate caused by a suddenly punched hole. Journal of Applied Mechanics 32: 949-950. 1965.

126. Eringen, A. C. Propagation of elastic waves generated by dynamical loads on a circular cavity. Transactions of the American Society of Mechanical Engineers 28E: 218-222. 1961.

127. Selberg, Henrik L. Transient compression waves from spherical and cylindrical cavities. Communicated by Nauckhoff, S. and Borelius, G. Arkiv Für Fysik Band 5, nr. 7: 97-107. June 6, 1951.

128. Bishop, R. E. D. On the dynamical problems of plane stress and plane strain. Quarterly Journal of Mechanics and Applied Mathematics 6: 250. 1953.

129. Goldsmith, W. and Norris, G. W. Stresses in curved beams due to transverse impact. Proceedings of the U. S. National Congress of Applied Mechanics 3. pp. 153-162. New York, N. Y., American Society of Mechanical Engineers. 1958.

130. Goldsmith, W. and Dabaghian, L. Photoelastic and strain-gage investigation of penetration of thin plates. Proceedings of the Society for Experimental Stress Analysis 18, No. 2: 121-128. 1961.

131. Clark, A. B. J. and Sanford, R. J. A comparison of static and dynamic properties of photoelastic materials. Proceedings of the Society for Experimental Stress Analysis 20, No. 1: 148-151. 1963.

132. Clark, A. B. J. Static and dynamic calibration of a photoelastic model material, CR-39. Proceedings of the Society for Experimental Stress Analysis 14, No. 1: 195-204. 1956.

133. Coolidge, D. J., Jr. An investigation of the mechanical and stress-optical properties of columbia resin, CR-39. Proceedings of the Society for Experimental Stress Analysis 6, No. 1: 74-82. 1948.

134. Sutton, George Walter. A study of the application of photoelasticity to the investigation of stress waves. Unpublished Ph.D. thesis. Pasadena, California, Library, California Institute of Technology. 1955.

135. Cook, Melvin A. The science of high explosives. New York, N. Y., Reinhold Book Corporation. 1958.

136. Cook, Melvin A. The amazing story of explosives. University of Utah Bulletin 42, No. 7. 1952.

137. Hopkinson, B. The effects of momentary stresses in metals. Proceedings of the Royal Society A, 74: 498. 1905.

138. Kolsky, H. The detection and measurement of stress waves. In Worley, Will J., ed. Experimental techniques in shock and vibration. pp. 11-24. New York, N. Y., The American Society of Mechanical Engineers. 1962.

139. Pochhammer, L. Über die fortpflanzungsgeschwindigkeiten schwingungen in einem unbengrenzten isotropen Kreisylinder. J. Jur. Math. 81: 324-336. 1876.

140. Chree, C. The equations of an isotropic elastic solid polar and cylindrical co-ordinates, their solution and application. Transactions of the Cambridge Philosophical Society 14: 250. 1889.

141. Chou, Pei Chi and Koenig, H. A. Unified approach to cylindrical and spherical elastic waves by method of characteristics. Journal of Applied Mechanics 33: 159-167. 1966.

142. Abramowitz, Milton and Segun, Irene A., eds. Handbook of mathematical functions. New York, N. Y., Dover Publications, Inc. 1965.

143. Kuske, Albrecht. Photoelastic research on dynamic stresses. Proceedings of the Society for Experimental Stress Analysis 23, No. 1: 105-112. 1966.

144. Skidmore, I. C. An introduction to shock waves in solids. Applied Materials Research 4: 135-147. 1965.

145. Mindlin, R. D. An introduction to the mathematical theory of vibrations of elastic plates. Fort Monmouth, New Jersey, U. S. Army Corps, Engineering Laboratories Monograph. 1955.

146. Bradley, W. B. and Kobayashi, A. S. A dynamic photoelastic system. (Department of Mechanical Engineering, University of Washington, Seattle, Washington) Office of Naval Research Contract Nonr-477(39) Nr 064 478 Technical Report No. 9. April, 1969.

ACKNOWLEDGEMENTS

It is with the greatest satisfaction that I am able to thank the many fine people who made this study possible.

First and foremost I would like to express my deepest appreciation to my wife, Linda, who in addition to her numerous duties as a mother, teacher and understanding spouse, spent many endless hours typing and retyping, assisting in the dark room, and helping with the many minute, but time consuming, tasks that were necessary in presenting this study in a written form. To my five year old son, Dan, who has grown very disenchanted with the study, I wish to express my apology for the many hours of patience that I demanded of such a small boy.

A very special thanks goes to my major advisor, Professor W. F. Riley, for the knowledge, inspiration, advice and numerous hours of time that he readily gave throughout the investigation. His constant concern for the financial needs and the well being of his students is greatly appreciated and deserves special notice.

Throughout an investigation such as this, a need arises from time to time for assistance from people with expertise in various specialized areas. For such assistance, I would like to especially thank Professor T. R. Rogge for his lengthy work and financial computer aid on the TOODY II numerical comparison, Professor K. G. McConnell for his

helpful advise on instrumentation and Professor L. W. Schmerr for his assistance on the theoretical aspects of wave propagation.

Sincere thanks is given to Professor H. J. Weiss, the Engineering Mechanics Department, and the Engineering Research Institute without whose financial assistance none of the study would have been possible.

APPENDIX A: ELECTRICAL ANALYSIS OF THE HIGH VOLTAGE SYSTEM

Once the cascading arc of high voltage has been initiated by the internal triggered spark gap, the time between the firing of gap A and that of gap B is controlled by the magnitude of the inductance L in the following circuit:

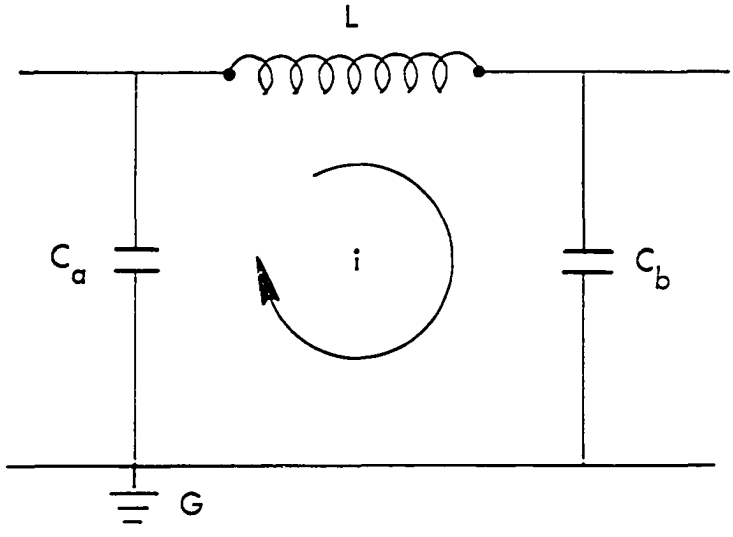

In order to calculate the time lag between the discharge of gap A and that of gap B, a loop equation for the center section was written in terms of the capacitance C, inductance L, and electrical discharge q:

$$L\ddot{q} + \frac{q}{C_a} + \frac{q}{C_b} = 0 \qquad (60)$$

Since $C_a = C_b$, Equation 60 was simplified to

$$L\ddot{q} + \frac{2q}{C} = 0 \tag{61}$$

Differential Equation 61 has a solution which may be written in the form

$$q = A \cos\omega t + B \sin\omega t \tag{62}$$

where

$$\omega = \sqrt{\frac{2}{LC}}$$

Since the current is simply the time derivative of charge, Equation 62 was differentiated to give

$$\dot{q} = i = \omega(-A \sin\omega t + B \cos\omega t) \tag{63}$$

The initial conditions for the circuit were

$$i\Big|_{t=0} = 0 \tag{64}$$

$$E\Big|_{t=0} = E_0 \tag{65}$$

From elementary circuit theory, the circuit voltage may be written in terms of current and inductance as

$$E(t) = \frac{1}{C}\int i\, dt = \frac{1}{C}\, q(t) \tag{66}$$

After applying initial condition 64 to Equation 63, the constant B was found to be

$$B = 0 \tag{67}$$

The constants B and ω were then substituted into Equation 62 to yield

$$q = A \cos \sqrt{\frac{2}{LC}}\, t \tag{68}$$

The constant A was evaluated by utilizing initial condition 65 and Equation 66 in Equation 68, i.e.

$$A = CE_o \tag{69}$$

By substituting Equations 66 and 69 into Equation 68, the fluctuation of the voltage as a function of time may be expressed as

$$E(t) = E_o \cos\sqrt{\frac{2}{LC}}\, t \tag{70}$$

Equation 70 indicated that the voltage varies in the manner shown in Figure 72.

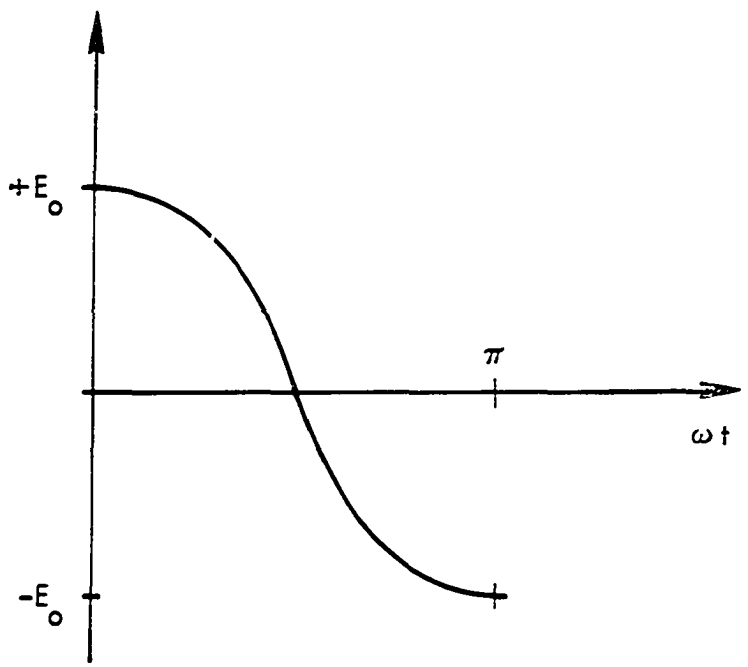

Figure 72. The time variation of the high voltage circuit

The length of time necessary for the voltage to drop from a positive E_o to a negative E_o is the amount of time that lapses between the firing of gap A and gap B. Since the drop is achieved in one half of a cycle, then the argument of the cosine must be equal to π radians, i.e.

$$\sqrt{\frac{2}{LC}}\, t = \pi \tag{71}$$

Therefore, the time between subsequent photographs was calculated from Equation 72.

$$t = \sqrt{\frac{LC}{2}}\, \pi \tag{72}$$

where

C is measured in farads

L is measured in henries

The framing rate was calculated from the inverse of the lapse time, i.e.

$$R = \frac{1}{t} = \frac{1}{\pi}\sqrt{\frac{2}{LC}} \tag{73}$$

Since all of the high voltage capacitors in the system were 0.05 micro-farads, Equation 73 was rewritten as

$$R = \frac{2 \times 10^3}{\sqrt{L}} \tag{74}$$

where

L is measured in henries

R is the framing rate

Equation 74 illustrates that the framing rate of the camera is readily changed by varying the inductance. Since

only experimentation can incorporate all the variables in inductor design, an approximate value was calculated for each inductor to produce the desired framing rate from Equation 75.

$$L = 3.19 \times 10^{-8} n^2 lA \qquad (75)$$

where

L = inductance (henries)

l = core length (inches)

n = turns/inch for a given diameter wire

A = cross-sectional area of the core (inches)

In order to obtain the desired spectrum of framing rates from approximately 50,000 to 1,000,000 frames per second (f.p.s.), a large range of inductances from 4 micro-henries were needed. Since this required a large variation in the number of turns on each inductor, two different sizes of cores were used. The calculated values for the framing rates as well as those determined from actually discharging the camera, are shown in Table 3.

Table 3. Inductor design

R Theoretical Speed (f.p.s.)	R' Experimental Speed (f.p.s.)	L Inductance (μ henries)	n Turns per inch	N Turns	D_c Core Diameter (inches)	l Coil Length (inches)
980,000	815,000	4.17	15	5	1.5	0.33
725,000	753,000	7.60	15	9	1.5	0.60
488,000	535,000	16.82	15	20	1.5	1.33
251,000	272,000	63.25	15	75	1.5	5.00
188,500	320,000	113.00	15	18	4.0	1.25
99,000	129,000	408.00	15	68	4.0	4.53
71,250	87,000	790.00	15	131	4.0	8.75

APPENDIX B: OPTICAL SYSTEM DESIGN OF THE MULTIPLE SPARK CAMERA

The optical analysis of the multiple spark camera is composed of two separate but compatible systems. The optical elements are aligned in such a manner that the image of the model is illuminated as well as focused on the film plane of the camera. In ordinary photography, the alignment of the camera lens has a large amount of latitude since the light is reflected from the object through a single camera lens. However, in dynamic photoelastic photography, where high speed images are recorded on film by transmitted light through both a field lens and a camera lens, the alignment of the optical elements becomes critical with much less tolerance.

Illumination System

The light output produced by each spark gap is directed through the lens assembly as shown in Figure 73. In order for the light from a given gap location to focus on the appropriate lens of the lens array, the parameters in the lens formula must be satisfied:

$$\frac{1}{q_a'} - \frac{1}{p_a'} = \frac{1}{f_a} \tag{76}$$

In accordance with the lens formula, the output of light from a given gap location, say number 1, would be directed through the field lens to the lens position number

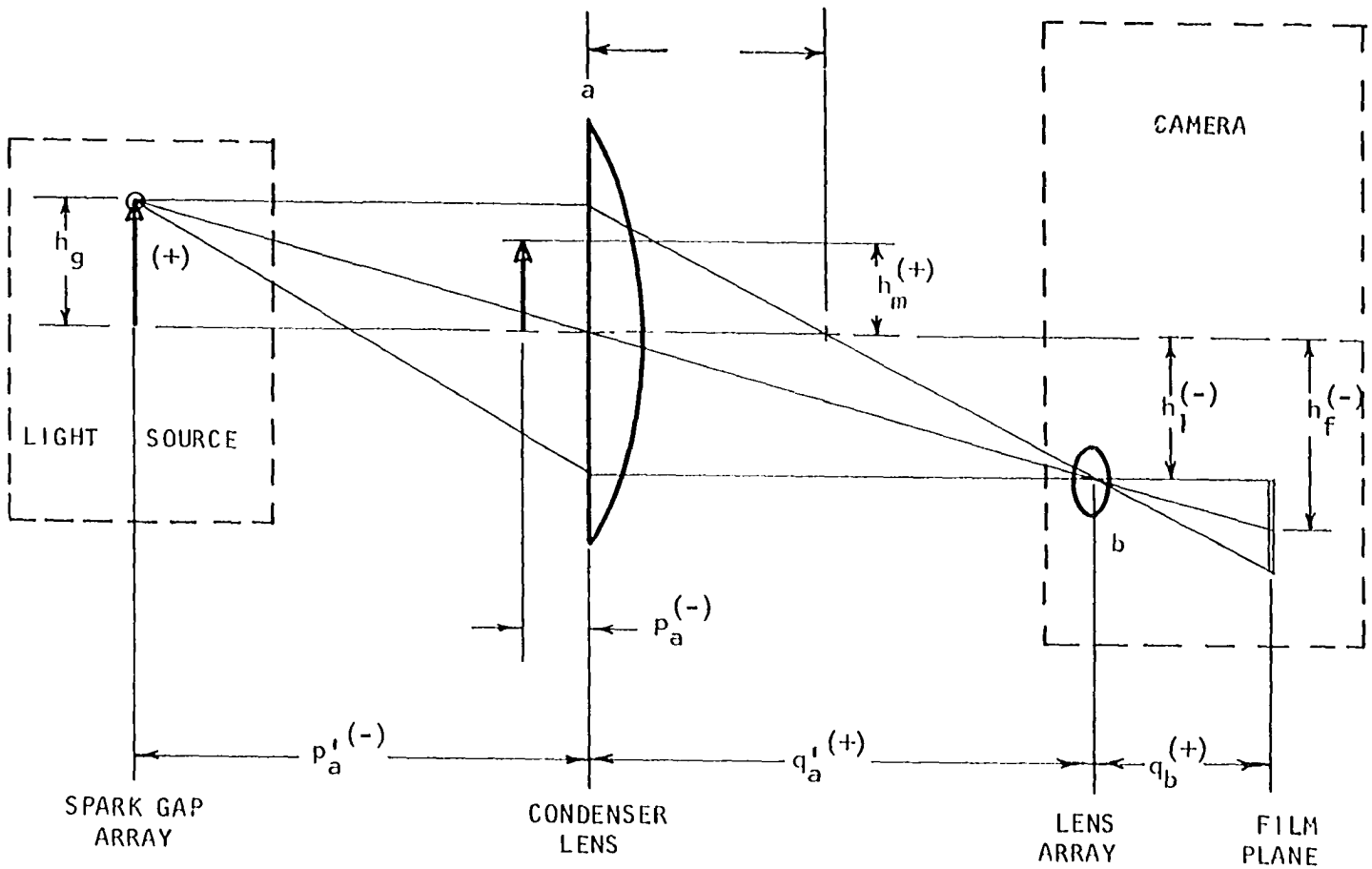

Figure 73. Model illumination system

16 of the lens array (Figure 74). A useful relationship is the ratio of the vertical height of a particular gap location with that of the corresponding lens location. This ratio is known as the magnification

$$M_a = \frac{h_1}{h_g} = \frac{q_a'}{p_a'} \tag{77}$$

Upon substitution of Equation 77 into Equation 76, the lens formula may be rewritten as:

$$q_a' = (1 - M_a)\, f_a \tag{78}$$

or

$$p_a' = q_a'/M_a \tag{79}$$

With Equations 78 and 79 satisfied, the maximum amount of light from a given gap will enter the appropriate lens.

Camera System

In the camera system, a virtual image of the model is produced in the field lens which is recorded on the film plane by a view camera lens. Although this optical system differs from that of the illumination system, the alignment is designed such that the image falls within the illuminated area on the film plane (Figure 75). In order for the image of the model to be focused on the film plane with a magnification M of the combined lens system, then

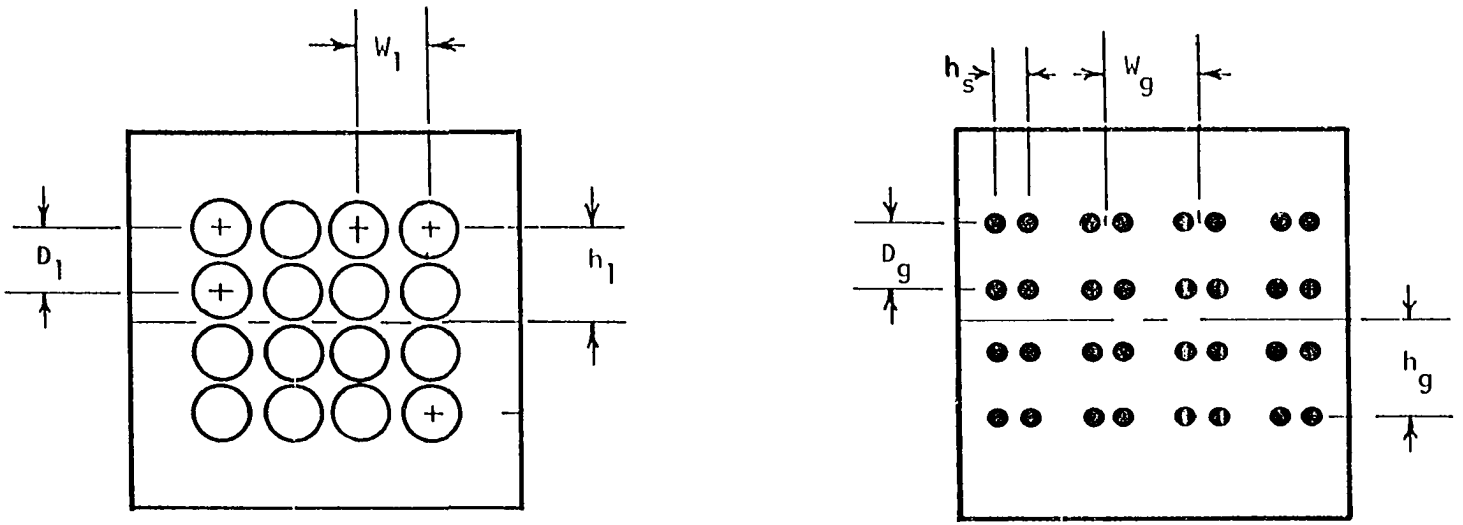

Figure 74. The lens and the spark gap arrays

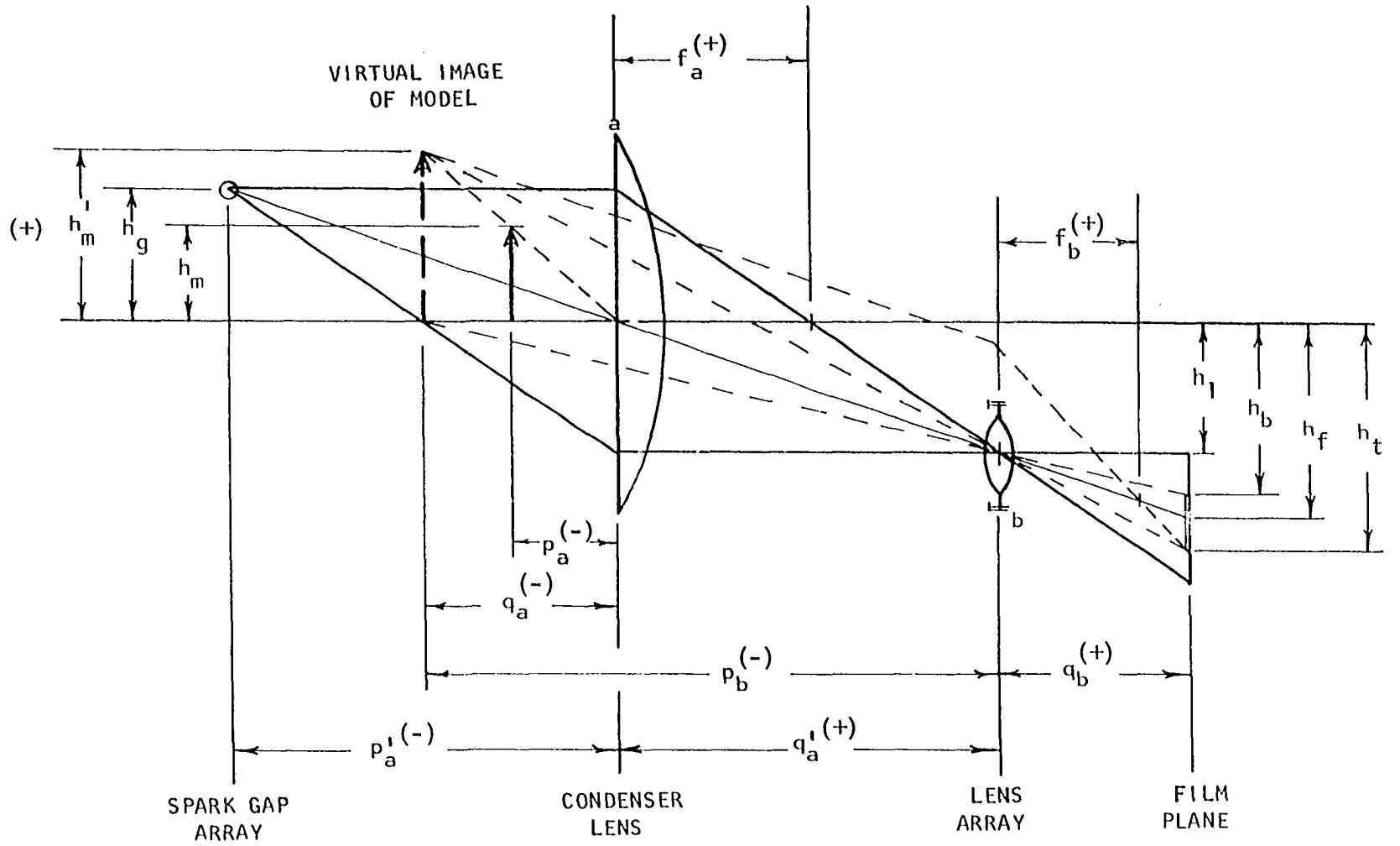

Figure 75. Alignment of optical system

$$M = \frac{h_f}{h_m} = \frac{q_a q_b}{p_a p_b} \tag{80}$$

The lens equation for the field lens for the photographic process is represented by:

$$\frac{1}{q_a} - \frac{1}{p_a} = \frac{1}{f_a} \tag{81}$$

while for each of the view camera lenses, the equation is written as:

$$\frac{1}{q_b} - \frac{1}{p_b} = \frac{1}{f_b} \tag{82}$$

Having utilized the fact that

$$p_b^{(-)} = q_a^{(-)} - q_a^{(+)} \tag{83}$$

Equations 80, 81, 82, and 83 are combined to give

$$M = \frac{f_a f_b}{p_a f_a - (f_a + p_a)(q_a' - f_b)} \tag{84}$$

The amount of draw on the camera bellows is calculated from

$$q_b = M(p_a - q_a'(1 + p_a/f_a)) \tag{85}$$

The distance from the field lens to the model plane is obtained from

$$p_a = \frac{f_a f_b((M - 1)/M) - q_a' f_a}{q_a' - f_a - f_b} \tag{86}$$

Calculations

Because of the necessity of compatibility between the two optical systems, certain limitations are imposed upon the dimensions of the elements themselves. Photoelasticity itself governs certain other requirements of the overall optical alignment.

Requirements for illuminating the model

One basic requirement of two dimensional photoelasticity is that the center line between the light source and the optical recorder be perpendicular to the plane of the model. Since this is not feasible in the multiple spark camera, it is desirable to hold this angle as close to 90° as possible. This requires that h_g and h_1 be held as small as possible and still be consistent with the design constraints. The smallest center to center distance obtainable for the view camera lenses is fixed by the physical diameter of the lens mounts; therefore, the only vertical design latitude is in the distance between the spark gap centers.

The 0.25 inch spark gaps were formed by 0.5 inch diameter brass spheres mounted on brass screw studs on 0.75 inch centers. The spark gaps were held to vertical centers of

$$D_g = 2.75 \text{ inches} \tag{87}$$

Therefore, the vertical height of the upper level of gaps in the spark gap array was fixed at

$$h_g = 4.125 \text{ inches} \tag{88}$$

The diameter of each camera lens housing was found to be

$$d_b' = 2.25 \text{ inches} \tag{89}$$

Therefore, the minimum convenient vertical distance between lens centers was held to

$$D_1 = 3.565 \text{ inches} \tag{90}$$

The vertical height of the upper level of lenses in the lens array was fixed at

$$h_1 = 3.565 \text{ inches} \tag{91}$$

Since it was desirable to have the sixteen frames evenly proportioned on the 11 inch by 14 inch film back, W_1 and D_1 as well as W_g and D_g (Figure 74), were proportioned to an 11 by 14 ratio. Therefore,

$$W_s = 3.50 \text{ inches} \tag{92}$$

and

$$W_1 = 3.02 \text{ inches} \tag{93}$$

The plano-convex field lens has the following specifications

$$\text{focal length} = f_a = 24 \text{ inches} \tag{94}$$

$$\text{lens diameter} = d_a = 16 \text{ inches} \tag{95}$$

Each of the sixteen camera lenses in the lens array has the following specifications

$$\text{focal length} = f_b = 7.5 \text{ inches} \tag{96}$$

$$\text{lens diameter} = \frac{f_b}{F} = \frac{7.5}{4.5} = 1.6 \text{ inches} \tag{97}$$

From Equation 77 the magnification was found to be

$$M_a = -.865 \tag{98}$$

The distance from the field lens to the lens array was obtained from Equation 78, i.e.

$$q_a' = (1 + .865)24 = 44.8 \text{ inches} \tag{99}$$

The distance from the field lens to the spark gap array was calculated from Equation 79.

$$p_a' = \frac{44.8}{-.865} = -51.8 \text{ inches} \tag{100}$$

With this alignment of the optical elements, the illumination system is satisfied.

Requirements for recording the image of the model

Since the elements of the system are now fixed because of the illumination requirements, the model can only be shifted a small amount in the field without introducing barrel or pincushion distortion.

If the model is positioned a predetermined distance from the field lens, say

$$p_a = -3 \text{ inches} \tag{101}$$

then the ratio of the model size to that of the image is found from Equation 84, i.e.

$$M = \frac{(24)(7.5)}{-3(24) - (24 - 3)(44.8 - 7.5)} = -.21 \tag{102}$$

Therefore, for a circular model diameter of 10 inches, the image diameter would be 2.1 inches. This would be projected on the film plane by a 2.76 inch diameter illuminated field.

The amount of draw necessary on the bellows in order to

to focus the image on the film plane is calculated from Equation 85, i.e.

$$q_b = -.21 - 3 - 44.8(1 + - 3/24) = 8.86 \text{ inches} \quad (103)$$

APPENDIX C: LIST OF PHOTOGRAPHIC SYSTEM COMPONENTS

Table 4. List of photographic system components

Item	Description	Manufacturer	Estimate of Cost
1	Power Pack Model MV20-502M, 2KVDC - 5 Milliamps (1)	Plastic Capacitors, Inc. 2620 N. Clybourn Avenue Chicago, Illinois	50.00
2	Type LK 150-503B Capacitors 0.05 MFD with Spade Type Brackets (4)		640.00
3	Power Pack Model HV 150-502M 15 KVCD - 5 Milliamps (1)		125.50
4	Model 612-W-630 Hallowell Cabinet Bench with 1 3/4" Maple Top (6'x30"x33½") (3)	Allen Supply Company 221 Third S.W. Cedar Rapids, Iowa	504.72
5	Brass Spheres - ½" Diameter (100)	McMaster-Carr Supply Co. P.O. Box 4355 Chicago, Illinois	8.85
6	Resistor Type MVC-3, 15 KV 1 Meg., 3 Watts, ± 20% Axial Leads (20)	International Resistance Co. 6020 W. Diversey Chicago, Illinois	18.20
7	Resistor Type MVC-3, 15 KV, 3 Megs., 3 Watts, ± 20% Axial Leads (4)		5.40

Table 4. (Continued)

Item	Description	Manufacturer	Estimate of Cost
8	Resistor Type MVC-3, 15 KV, 1000 Megs., 3 Watts, ± 5%, Axial Leads (3)		6.09
9	Resistor Type MVD-15, 15 KV, 22.5 Megs., 10 Watts, ± 20% Axial Leads (2)		5.36
10	E.F. Johnson Series #35 Feed Thru-Panel Insulators Type 135-44 (40)	Newark Electronics Corp. 500 North Pulaski Road Chicago, Illinois	13.20
11	Light Sensor IN2175, Max. Voltage: 50 Volts, Rise Time: 2μsec for 10% to 90% Conductivity (1)		6.40
12	19"x50"x0.030" sheet of plastic Laminated Circular Polarizer Type HN-CP-35 or HN-CP-37 (1)	Polarizer Division Polaroid Corporation Cambridge, Massachusetts	35.00
13	Neon Sign Cable-250' Spool 15,000 Volt Cable-Belden No. 318055 (2)	Neon Materials Company 2343 W. Potomac Avenue Chicago, Illinois	24.00
14	Bud Series 60 Cabinet Rack Upright, Louvered Sides, Plain Door Type (1)	Deeco, Incorporated 618 - 1st N.W. Cedar Rapids, Iowa	80.00

Table 4. (Continued)

Item	Description	Manufacturer	Estimate of Cost
15	Ryertex Sheet Grade XXX 36"x72"x¼" (3)	J.T. Ryerson & Son 2558 W. 16th Street Chicago, Illinois	127.30
16	Ryertex Round Tubes Finished to 3 3/4" I.D. by 1/8" Wall. Random Lengths - Approx. 36 in. Grade XXX (8)		68.00
17	Ryertex Round Tubes, Finished to 1¼" I.D. by 1/8" Wall. Random Lengths-Approx. 36 in. Grade XXX (4)		14.00
18	E.G.G. Model TM-11 Trigger Modeule (1)	Edgerton, Germeshausen and Grier Inc. 160 Brookline Avenue Boston, Massachusetts	300.00
19	E.G.G. Model GP-12B Trigger Spark Gap (1)		350.00
20	E.G.G. Model 560 Lite-Mike with Model 561 Head (1)		375.00
21	Rexo Plano-Convex Condensing Lens 16 inch diameter by 24 inch focus (1)	Porter's Camera Store 2208 College Street Cedar Falls, Iowa	254.00

Table 4. (Continued)

Item	Description	Manufacturer	Estimate of Cost
22	Special 11x14 Camera with Rear Section to Accept Standard 11x14 Cut Film Holder and Front Section to Accept 14x14 Lens Board (1)	Burke & James, Inc. 333 West Lake Street Chicago, Illinois	325.00
23	7½" F/4.5 Kodak Anastigmat Lens in Barrel with Iris. Minimum Male Mounting Flange. (16)		1480.00
24	11x14 Film Holder (1)		40.00
25	Wratten Filter No. 34A Gelatin Film - 2 inch square (20)	Eastman Kodak Co. 2205 Ingersoll Avenue Des Moines, Iowa	40.00
26	Wratten Filter No. 47B Gelatin Film - 2 inch Square (2)		40.00
27	Type 547 Oscilloscope (1)	Tektronix, Inc. 400 Higgins Road Park Ridge, Illinois	1875.00
28	Model 202-2 Scope-Mobile Cart (1)		130.00
29	Model C-12 Polaroid Camera (1)		450.00
30	Camera Mounting Bezel Part # 016-0226-00 (1)		15.00

Table 4. (Continued)

Item	Description	Manufacturer	Estimate of Cost
31	Type 1A1 Dual Trace Plug-In Unit (1)		600.00
32	Type L Plug-In Unit (1)		210.00
33	Model 420 Taut-Bank 0-20UA DC Microammeter (1)	Allied Electronics 100 N. Western Avenue Chicago, Illinois	31.10
34	1,000 ft. Spool Type MW-Plastic Wire MIL-W-76B, 1,000 Volt, 80° C Solid Conductor #20 (6)		31.80
35	Box of Fit-221 Shrinkable Tubing		12.00
36	Assorted Insulators, Terminals, Plugs, Banana Jacks, Washers, Nuts, and Bolts, etc.		150.00
37	Machining and Fabrication of Aluminum Mountings	Iowa State University Engineering Research Institute Machine Shop Ames, Iowa	700.00

APPENDIX D: PHOTODIODE DESCRIPTION AND ADJUSTMENT

The E.G.G. Lite-Mike with a model 561 detector head is shown in Figure 76. Before the Lite-Mike initially becomes a unit of the multiple spark system, a Kodak Wratten K-2 filter must be placed over the lens of the detector in order to absorb those rays in the blue region of the electric arc spectrum that are harmful to the photodiode tube. The Lite-Mike is located as close to the spark gap array as possible without disrupting the optical field (Figure 15). The detector head is positioned such that the illumination of the complete array is visible to the photodiode during a firing sequence. Once the Lite-Mike is switched on, in the lighting conditions that the test will be conducted (total darkness), the ambient null control on the base of the assembly (Figure 76) should be increased until the microamperes scale is zeroed. Since the output signal of the photodiode is proportional to the intensity of the light emitted by each gap, a meter level of 50 microamperes with a sensitivity of 10 (Figure 76) was found to produce the desired 1 to 2 volts of output for the system. This is then relayed to the input of the vertical oscilloscope trace.

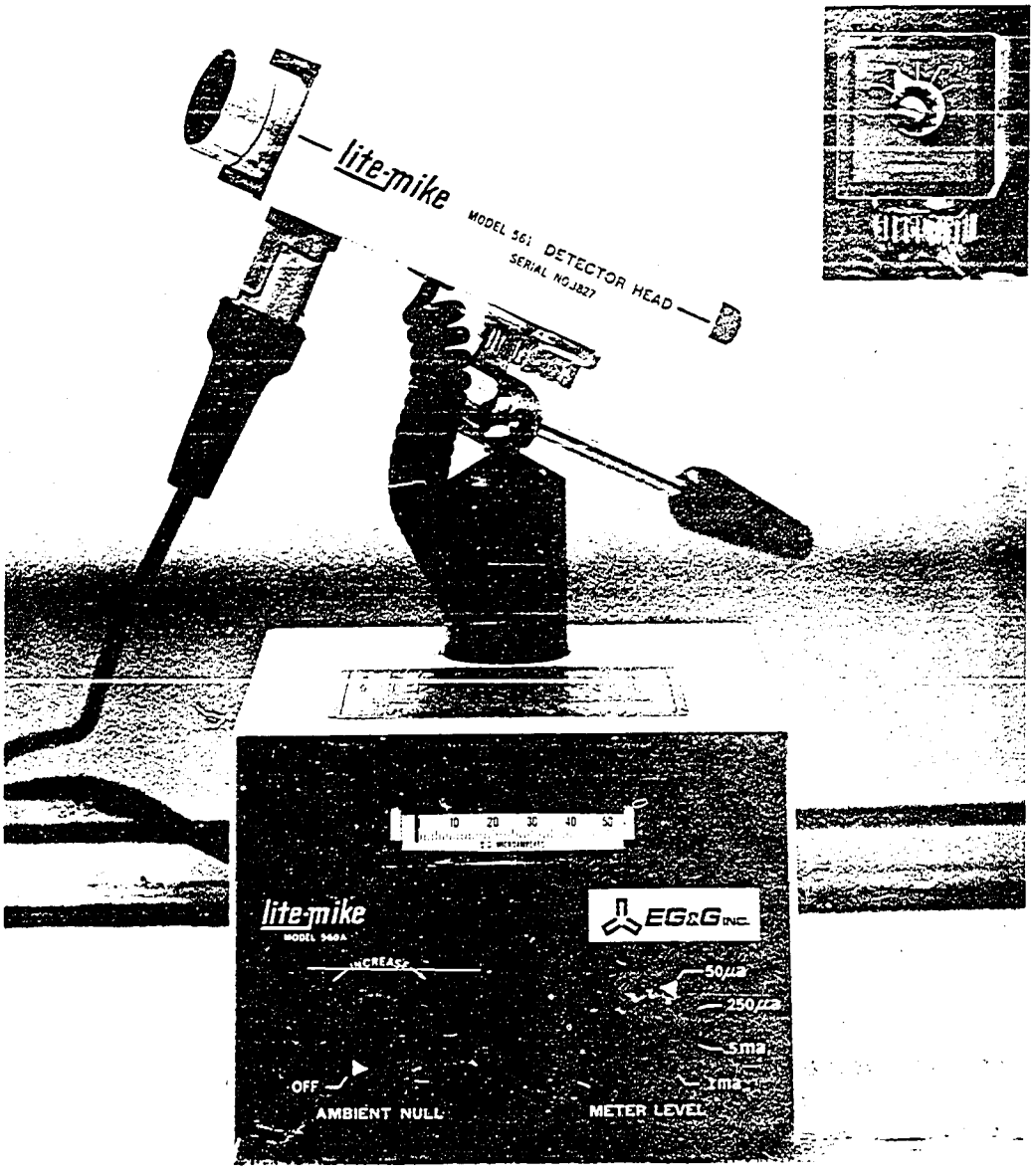

Figure 76. The E.G.G. photodiode light sensor

APPENDIX E: TOODY II: RESULTS AND DISCUSSION

The parameters used for the input of the program were determined from experimental data and information received from Sandia, Table 5. This data is also shown in the

Table 5. Parameters for computer input

Material I (lead azide)

$\rho = 0.048$ lb./in.^{3}

$c_3 = 192{,}000$ in./sec.

Material II (Teflon)

$\rho_o = 0.065$ lb./in.^{3}

$\gamma_d = 0.45$

$s = 1.2$

$c_3 = 64{,}700$ in./sec.

Material III (Plexiglas)

$\rho_o = 0.0426$ lb./in.^{3}

$c_3 = 111{,}500$ in./sec.

$\Gamma_o = 1.36$

$s = 0.85$

$\gamma_d = 0.40$

computer readout (Figure 77). Figures 78, 79, and 80 represent a sample of the computer output for grids I = 4, J = 1 through 16 in Material I, I = 9, J = 1 through 16 in Material II, and I = 15, J = 1 through 16 in Material III respectively where

```
End of Step LKED      C373CUDY, CPU Time= 0000003.8 sec.
           Region Allocated= 0096K Main  0000K LCS
           Region Used     = 0090K Main  0000K LCS


Time in Seconds     0.4370E 05

Program Updated 2/6/68

Circular  Plate with Explosive Input for J. Ligon

    IT       JT    NOMAT    ALPHA IDELOU      NTAP   NTLIM  IPRINT    ISPEC     IACT   IECSW  IRRSSW     IRSF IGNORD
    99       16        3        2      1         4       1       1        0       20       1       1        1      0

          PMAX             TMAX             KT1            OUTMIN           OUTMAX          DELTOUT            PACT
    0.1000D 10       0.3000D-04       0.9000D 00       0.20760-05       0.3010D-04       0.1000D-06       0.2000D 03

            B1               B2               B3               B4              KT2              KT3
    0.1200D 01       0.6000D-01       0.0              0.0              0.5000D-07       0.1000D 01

         TFMIN            TFMAX            TFDEL   IPMIN   IPMAX   IPDEL   JPMIN   JPMAX   JPDEL
    0.0              0.3010D-04       0.1000D-06       1      44       1       1      16       1

          RSMIN            RSMAX            RSDEL
    0.1200D 02       0.2000D 02       0.1200D 02
Material Definition
   MAT      IS      IE      JS     JSI      JE     JEI
     1       2       6       2       0      15       0
     2       7      11       2       0      15       0
     3      12      99       2       0      15       0
    13       1      99       1       0       1       0
    13       1      99      16       0      16       0
    11      99      99       2       0      15       0
    13       1       1       2       0      15       0

Constants for Material     1          Equation of State     2
    0.4800D-01       0.1920D 06       0.1920D 06       0.1750D 01       0.2500D 01       0.2809D 10
             4       0.1875D-01       0.1875D-01

Constants for Material     2          Equation of State     1
                     0.6500D-01       0.6470D 05       0.0              -0.1000D 01      0.9091D-01       0.1138D 01
             0       0.2721D 09       0.1200D 01       0.0              0.0              0.0              0.0
             2       0.1300D 01      -0.1000D 01       0.0              0.0              0.0              0.0
             0       0.2815D 08       0.0              0.0              0.0              0.0              0.0
             2       0.0              0.0              0.0              0.0              0.0              0.0

Constants for Material     3          Equation of State     1
                     0.4260D-01       0.1115D 06       0.0              -0.1000D 01      0.1667D 00       0.1286D 01
             0       0.5296D 09       0.8500D 00       0.0              0.0              0.0              0.0
             2       0.1360D 01      -0.1000D 01       0.0              0.0              0.0              0.0
             0       0.1135D 09       0.0              0.0              0.0              0.0              0.0
             2       0.0              0.0              0.0              0.0              0.0              0.0
```

Figure 77. Readout of input data

Cycle 251 Circular Plate with Explosive Input for J. Ligon Time=0.21535D-05 DT=0.86403751D-08

I	J	Mat	X/UX	Z/UZ	P/Q	DTXX/DQXX	DTXZ/DQXZ	DTZZ/DQZZ	RHO/C	E/Z
4	1	13	0.0	0.10321D 00	0.0	0.0	0.0	0.0	0.0	0.0
			0.0	0.34571D 04	0.0	0.0	0.0	0.0	0.0	0.0
4	2	1	0.10816D-01	0.10264D 00	0.23720D 08	0.0	0.0	0.0	0.20815D-01	0.65117D 09
Detonated			0.35833D 03	0.34396D 04	0.0	0.0	0.0	0.0	0.19200D 06	0.21205D-03
4	3	1	0.21510D-01	0.10094D 00	0.23720D 08	0.0	0.0	0.0	0.20815D-01	0.65116D 09
Detonated			0.71626D 03	0.33817D 04	0.0	0.0	0.0	0.0	0.19200D 06	0.21206D-03
4	4	1	0.31969D-01	0.98127D-01	0.23720D 08	0.0	0.0	0.0	0.20815D-01	0.65116D 09
Detonated			0.10626D 04	0.32857D 04	0.0	0.0	0.0	0.0	0.19200D 06	0.21206D-03
4	5	1	0.42076D-01	0.94234D-01	0.23719D 08	0.0	0.0	0.0	0.20815D-01	0.65115D 09
Detonated			0.13986D 04	0.31534D 04	0.0	0.0	0.0	0.0	0.19200D 06	0.21206D-03
4	6	1	0.51721D-01	0.89302D-01	0.23719D 08	0.0	0.0	0.0	0.20815D-01	0.65114D 09
Detonated			0.17218D 04	0.29853D 04	0.0	0.0	0.0	0.0	0.19200D 06	0.21206D-03
4	7	1	0.60796D-01	0.83388D-01	0.23720D 08	0.0	0.0	0.0	0.20815D-01	0.65116D 09
Detonated			0.20253D 04	0.27871D 04	0.0	0.0	0.0	0.0	0.19200D 06	0.21205D-03
4	8	1	0.69201D-01	0.76556D-01	0.23720D 08	0.0	0.0	0.0	0.20815D-01	0.65116D 09
Detonated			0.23065D 04	0.25580D 04	0.0	0.0	0.0	0.0	0.19200D 06	0.21205D-03
4	9	1	0.76844D-01	0.68881D-01	0.23721D 08	0.0	0.0	0.0	0.20816D-01	0.65118D 09
Detonated			0.25623D 04	0.23012D 04	0.0	0.0	0.0	0.0	0.19200D 06	0.21204D-03
4	10	1	0.83640D-01	0.60448D-01	0.23722D 08	0.0	0.0	0.0	0.20816D-01	0.65120D 09
Detonated			0.27892D 04	0.20194D 04	0.0	0.0	0.0	0.0	0.19200D 06	0.21204D-03
4	11	1	0.89515D-01	0.51349D-01	0.23722D 08	0.0	0.0	0.0	0.20816D-01	0.65121D 09
Detonated			0.29856D 04	0.17153D 04	0.0	0.0	0.0	0.0	0.19200D 06	0.21204D-03
4	12	1	0.94403D-01	0.41687D-01	0.23723D 08	0.0	0.0	0.0	0.20816D-01	0.65122D 09
Detonated			0.31482D 04	0.13926D 04	0.0	0.0	0.0	0.0	0.19200D 06	0.21203D-03
4	13	1	0.98251D-01	0.31560D-01	0.23724D 08	0.0	0.0	0.0	0.20817D-01	0.65123D 09
Detonated			0.32767D 04	0.10536D 04	0.0	0.0	0.0	0.0	0.19200D 06	0.21203D-03
4	14	1	0.10102D 00	0.21088D-01	0.23723D 08	0.0	0.0	0.0	0.20816D-01	0.65122D 09
Detonated			0.33690D 04	0.70427D 03	0.0	0.0	0.0	0.0	0.19200D 06	0.21208D-03
4	15	1	0.10267D 00	0.10384D-01	0.23724D 08	0.0	0.0	0.0	0.20817D-01	0.65123D 09
Detonated			0.34238D 04	0.34629D 03	0.0	0.0	0.0	0.0	0.19200D 06	0.21203D-03
4	16	13	0.0	0.0	0.0	0.0	0.0	0.0	0.0	0.0
			0.0	0.0	0.0	0.0	0.0	0.0	0.0	0.0

Figure 78. Sample TOODY II output for Material I

Cycle 251 Circular Plate with explosive input for J. Ligon Time=0.21535D-05 DT=0.86403751D-08

I	J	Mat	X/UX	Z/UZ	P/Q	DTXX/DQXX	DTXZ/DQXZ	DTZZ/DQZZ	RHO/C	E/A
9	1	13	0.0 0.0	0.20760D 00 0/76216D 04	0.0 0.0	0.0 0.0	0.0 0.0	0.0 0.0	0.0 0.0	0.0 0.0
9 Elastic	2	2	0.21762D-01 0.80656D 03	0.20647D 00 0.75826D 04	0.17459D 08 0.15796D 05	0.85593D 07 0.0	-0.13351D 07 0.0	-0.17092D 08 0.0	0.68007D-01 0.73927D 05	0.52386D 08 0.50790D-03
9 Elastic	3	2	0.43286D-01 0.16-19D 04	0.20306D 00 0.74636D 04	0.17604D 08 0.18104D 05	0.79821D 07 0.0	-0.39901D 07 0.0	-0.16526D 08 0.0	0.68038D-01 0.73968D 05	0.52487D 08 0.50771D-03
9 Elastic	4	2	0.64333D-01 0.23773D 04	0.19741D 00 0.72617D 04	0.17657D 08 0.18540D 05	0.68666D 07 0.0	-0.64697D 07 0.0	-0.15407D 08 0.0	0.68050D-01 0.73984D 05	0.52487D 08 0.50768D-03
9 Elastic	5	2	0.84670D-01 0.31259D 04	0.18959D 00 0.69764D 04	0.17681D 08 0.18721D 05	0.52730D 07 0.0	-0.86473D 07 0.0	-0.13808D 08 0.0	0.68055D-01 0.73991D 05	0.52483D 08 0.50768D-03
9 Elastic	6	2	0.10407D 00 0.38400D 04	0.17967D 00 0.66121D 04	0.17691D 08 0.18703D 05	0.32639D 07 0.0	-0.10445D 08 0.0	-0.11796D 08 0.0	0.68057D-01 0.73994D 05	0.52484D 08 0.50770D-03
9 Elastic	7	2	0.12233D 00 0.45114D 04	0.16777D 00 0.61742D 04	0.17697D 08 0.18856D 05	0.92404D 06 0.0	-0.11785D 08 0.0	-0.94538D 07 0.0	0.68058D-01 0.73996D 05	0.52483D-08 0.50771D-03
9 Elastic	7	2	0.13924D 00 0.51334D 04	0.15403D 00 0.54484D 04	0.17703D 08 0.19037D 05	-0.16438D 07 0.0	-0.12608D 08 0.0	-0.68845D 07 0.0	0.68060D-01 0.73998D 05	0.52487D 08 0.50771D-03
9 Elastic	9	2	0.15462D 00 0.56988D 04	0.13849D 00 0.51002D 04	0.17707D 08 0.19137D 05	-0.43272D 07 0.0	-0.12877D 08 0.0	-0.42001D 07 0.0	0.68060D-01 0.73999D 05	0.52489D 08 0.50771D-03
9 Elastic	10	2	0.16829D 00 0.62015D 04	0.12162D 00 0.44757D 04	0.17708D 08 0.19240D 05	-0.70082D 07 0.0	-0.12582D 08 0.0	-0.15182D 07 0.0	0.68061D-01 0.73999D 05	0.52490D 08 0.50771D-03
9 Elastic	11	2	0.18011D 00 0.66361D 04	0.10331D 00 0.38018D 04	0.17709D 08 0.19312D 05	-0.95692D 07 0.0	-0.11734D 08 0.0	0.10433D 07 0.0	0.68061D-01 0.74000D 05	0.52492D 08 0.50772D-03
9 Elastic	12	2	0.13994D 00 0.69976D 04	0.83866D-01 0.30860D 04	0.17710D 08 0.19352D 05	-0.11898D 08 0.0	-0.10372D 08 0.0	0.337240 07 0.0	0.68061D-01 0.74000D 05	0.52493D 08 0.50772D-03
9 Elastic	13	2	0.19769D 00 0.72817D 04	0.63497D-01 0.23363D 04	0.17710D 08 0.19452D 05	-0.13892D 08 0.0	-0.85526D 07 0.0	0.53669D 07 0.0	0.68061D-01 0.74000D 05	0.52493D 08 0.50772D-03
9 Elastic	14	2	0.20324D 00 0.74852D 04	0.42428D-01 0.15615D 04	0.17706D 08 0.19473D 05	-0.15462D 08 0.0	-0.63550D 07 0.0	0.69375D 07 0.0	0.68061D-01 0.73999D 05	0.52481D 08 0.50773D-03
9 Elastic	15	2	0.20658D 00 0.76052D 04	0.20393D-01 0.76914D 03	0.17707D 08 0.19373D 05	-0.16538D 08 0.0	-0.38780D 07 0.0	0.80145D 07 0.0	0.68061D-01 0.73999D 05	0.52468D 08 0.50773D-03
9	16	13	0.0 0.0	0.0 0.0	0.0 0.0	0.0 0.0	0.0 0.0	0.0 0.0	0.0 0.0	0.0 0.0

Figure 79. Sample TOODY II output for Material II

Cycle 251 Circular Plate with Explosive Input for J. Ligon Time=0.21535D-05 DT=0.86403751D-08

I	J	Mat	X/UX	Z/UZ	P/Q	DTXX/DQXX	DTXZ/DQXZ	DTZZ/DQZZ	RHO/C	E/A
15	1	13	0.0 0.0	0.38213D 00 0.20279D 03	0.0 0.0	0.0 0.0	0.0 0.0	0.0 0.0	0.0 0.0	0.0 0.0
15 Elastic	2	3	0.40050D-01 0.21274D 02	0.38002D 00 0.20173D 03	0.16167D 07 0.21748D 06	0.28022D 06 0.0	-0.44302D 05 0.0	-0.56169D 06 0.0	0.42730D-01 0.12670D 06	0.90026D 05 0.11945D-02
15 Elastic	3	3	0.79649D-01 0.42301D 02	0.37373D 00 0.19650D 03	0.16177D 07 0.21765D 06	0.26181D 06 0.0	-0.13109D 06 0.0	-0.54344D 06 0.0	0.42730D-01 0.12670D 06	0.90133D 05 0.11945D-02
15 Elastic	4	3	0.11839D 00 0.62894D 02	0.36333D 00 0.19303D 03	0.16184D 07 0.21774D 06	0.22577D 06 0.0	-0.21226D 06 0.0	-0.50752D 06 0.0	0.42730D-01 0.12670D 06	0.90211D 05 0.11945D-02
15 Elastic	5	3	0.15582D 00 0.82798D 02	0.34892D 00 0.18542D 03	0.16188D 07 0.21782D 06	0.17350D 06 0.0	-0.28415D 06 0.0	-0.45534D 06 0.0	0.42730D-01 0.12670D 06	0.90263D 05 0.11945D-02
15 Elastic	6	3	0.19153D 00 0.10180D 03	0.33067D 00 0.17575D 03	0.16192D 07 0.21786D 06	0.10735D 06 0.0	-0.34352D 06 0.0	-0.38924D 06 0.0	0.42730D-01 0.12670D 06	0.90298D 05 0.11945D-02
15 Elastic	7	3	0.22513D 0.11967D	0.30877D 00 0.16412D 03	0.16193D 07 0.21789D 06	0.30279D 05 0.0	-0.38779D 06 0.0	-0.31220D 06 0.0	0.42730D-01 0.12670D 06	0.90317D 05 0.11945D-02
15 Elastic	8	3	0.25625D 00 0.13622D 03	0.28348D 00 0.15068D 03	0.16195D 07 0.21791D 06	-0.54350D 05 0.0	-0.41500D 06 0.0	-0.22760D 06 0.0	0.42730D-01 0.12670D 06	0.90331D 05 0.11945D-02
15 Elastic	9	3	0.28455D 00 0.15126D 03	0.25506D 00 0.13558D 03	0.16195D 07 0.21792D 06	-0.14277D 06 0.0	-0.42395D 06 0.0	-0.13918D 06 0.0	0.42730D-01 0.12670D 06	0.90336D 05 0.11945D-02
15 Elastic	10	3	0.30971D 00 0.16464D 03	0.22383D 00 0.11898D 03	0.16195D 07 0.21792D 06	-0.23112D 06 0.0	-0.41426D 06 0.0	-0.50840D 05 0.0	0.42730D-01 0.12670D 06	0.90337D 05 0.11945D-02
15 Elastic	11	3	0.33147D 00 0.17620D 03	0.19014D 00 0.10107D 03	0.16195D 07 0.21792D 06	-0.31549D 06 0.0	-0.38637D 06 0.0	0.33535D 05 0.0	0.42730D-01 0.12670D 06	0.90337D 05 0.11945D-02
15 Elastic	12	3	0.34957D 00 0.18582D 03	0.15435D 00 0.82040D 02	0.16195D 07 0.21792D 06	-0.39220D 06 0.0.	-0.34150D 06 0.0	0.11025D 06 0.0	0.42730D-01 0.12670D 06	0.90333D 05 0.11945D 02
15 Elastic	13	3	0.36382D 00 0.19339D 03	0.11686D 00 0.62110D 02	0.16194D 07 0.21791D 06	-0.45786D 06 0.0	-0.28161D 06 0.0	0.17591D 06 0.0	0.42730D-01 0.12670D 06	0.90329D 05 0.11945D-02
15 Elastic	14	3	0.37497D 00 0.19882D 03	0.76087D-01 0.41496D 02	0.16194D 07 0.21790D 06	-0.50948D 06 0.0	0.20936D 06 0.0	0.22765D 06 0.0	0.42730D-01 0.12670D 06	0.90321D 05 0.11945D-02
15 Elastic	15	3	0.38019D 00 0.20205D 03	0.38452D-01 0.20435D 02	0.16193D 07 0.21788D 06	-0.54507D 06 0.0	-0.12789D 06 0.0	0.26316D 06 0.0	0.42730D-01 0.12670D 06	0.90306D 05 0.11945D-02
15	16	13	0.0 0.0	0.0 0.0	0.0 0.0	0.0 0.0	0.0 0.0	0.0 0.0	0.0 0.0	0.0 0.0

Figure 80. Sample TOODY II output for Material III

I	radial mesh (column)
J	circumferential mesh (row)
X/UX	X coordinate
	UX = X velocity component (particle)
Z/UZ	Z coordinate
	UZ = Z velocity component (particle)
P/Q	P = pressure = -1/3 ($\sigma_x + \sigma_y + \sigma_z$)
	Q = artificial viscosity
DTXX/DQXX	DTXX = σ_x + p
	DQXX = artificial viscosity
DTXZ/DQXZ	DTXZ = τ_{xz}
	DQXZ = artificial viscosity
DTZZ/DQZZ	DTZZ = σ_y + p
	DQZZ = artificial viscosity
RHO/C	RHO = density
	C = sound speed
E/A	E = energy
	A = mesh area

The normalized pressure pulse P(t) was plotted along the radial grid line J = 2 at cycle 251, which occurred at 2.15 microseconds after detonation, Figure 81. This was the longest run obtained before the project funds were depleted. Since the pressure in grid 10 was lower than that in grid 11, the indication was that the peak of the pulse was on or very near grid 11. The pulse shape seemed

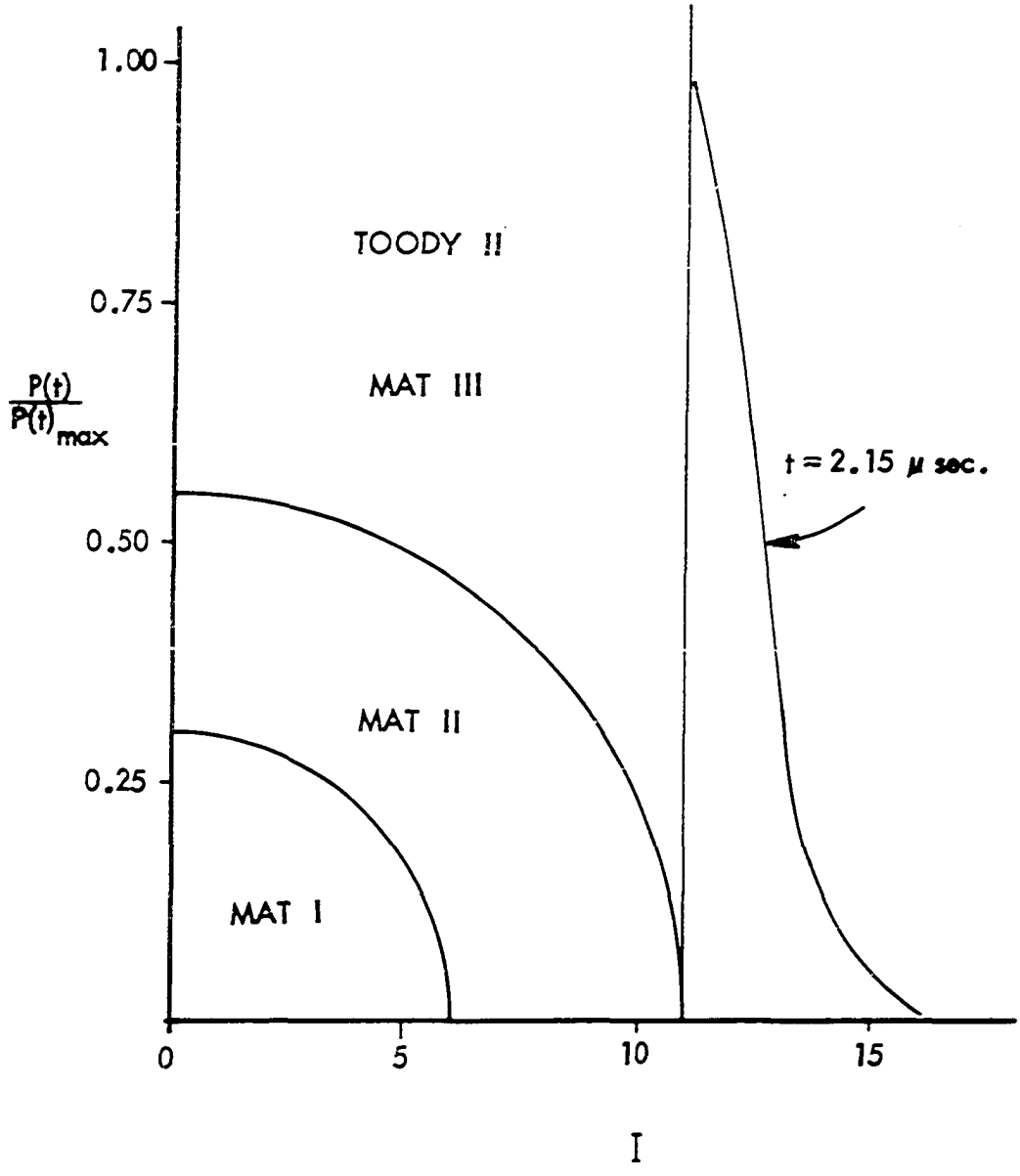

Figure 81. Normalized pressure pulse at the Teflon-Plexiglas interface

to form in a manner similar to that established experimentally with the exception of the stress magnitude. Therefore, the stress values at the Teflon-Plexiglas interface were normalized with respect to the assumed maximum at the boundary since the stress magnitudes were unreasonable.

The TOODY II reference manual indicates that several computer runs should be made in which the magnitude of the numerous constants are varied in order to check their sensitivity to change. It is believed by this author that correcting these values would decrease the boundary stress magnitude to a realistic value. However, funds were not available to pursue this endeavor. To illustrate one source of error, consider the value calculated for the detonation velocity of PbN_6, which was determined experimentally. Cook (135, page 45) gives an expression which clearly illustrates the drastic effect of explosive density changes on burn rate, i.e.

$$D^* = D^*_{\rho_1^\circ} + M^* (\rho_1 - \rho_1^\circ)$$

where

D^* = explosive detonation velocity

$D^*_{\rho_1^\circ}$ = detonation velocity at the density ρ_1°

($D^*_{\rho_1^\circ}(PbN_6) = 5{,}100$ m./sec.)

M^* = slope of the velocity-density curve

($M^*(PbN_6) = 560$)

ρ_1° = original reference density

($\rho_1^{\circ}(PbN_6)$ = 4 g./cc.)

ρ_1 = final detonation density

Using Cook's relation, the detonation velocity was calculated to be twice that which was used for PbN_6 in TOODY II.

In conclusion, TOODY II would appear to give very realistic results over the entire field if sufficient funds were available for investigating and making proper parameter adjustments.